A Theoretical and Computational Study of Limit Cycle Oscillations in High Performance Aircraft

by

Madhusudan A. Padmanabhan

Department of Mechanical Engineering and Materials Science
Duke University

Date: _____

Approved:

_____
Earl H. Dowell, Supervisor

_____
Thomas P. Witelski

_____
Kenneth C. Hall

_____
Donald B. Bliss

_____
Laurens E. Howle

_____
Jeffrey P. Thomas

Dissertation submitted in partial fulfillment of the requirements for the degree of Doctor of Philosophy in the Department of Mechanical Engineering and Materials Science in the Graduate School of Duke University

2015

Abstract

A Theoretical and Computational Study of Limit Cycle Oscillations in High Performance Aircraft

by

Madhusudan A. Padmanabhan

Department of Mechanical Engineering and Materials Science
Duke University

Date: _____

Approved:

_____
Earl H. Dowell, Supervisor

_____
Thomas P. Witelski

_____
Kenneth C. Hall

_____
Donald B. Bliss

_____
Laurens E. Howle

_____
Jeffrey P. Thomas

An abstract of a dissertation submitted in partial fulfillment of the requirements for the degree of Doctor of Philosophy in the Department of Mechanical Engineering and Materials Science in the Graduate School of Duke University
2015

Abstract

High performance fighter aircraft such as the F-16 experience aeroelastic Limit Cycle Oscillations (LCO) when they carry certain combinations of under-wing stores. This 'store-induced LCO' causes serious problems including airframe fatigue, pilot discomfort and loss of operational effectiveness. The usual response has been to restrict the stores carriage envelope based on flight test experience, and accept the accompanying reduction in mission performance.

Although several nonlinear mechanisms - structural as well as aerodynamic, have been proposed to explain the LCO phenomenon, their roles are not well understood. Consequently, existing models are unable to predict *accurately and reliably* the most critical LCO properties, namely onset speed and response level. On the other hand, the more accurate Computational Fluid Dynamics (CFD) based time marching methodology yields results at much greater expense and time. Clearly, there is a critical need to establish methods that are more rapid while providing accurate predictions more in line with flight test results than at present. Such a capability will also aid in future aircraft design and usage.

This work was undertaken to develop a better understanding of nonlinear aeroelastic phenomena, and their relation to classical flutter and divergence, with a particular focus on store-induced LCO in high performance fighter aircraft. The following systems were studied: (1) a 'simple' wing with a flexible and nonlinear root attachment, (2) a 'generic' wing with a flexible and nonlinear wing-store attachment and

(3) the F-16 aircraft, again with nonlinear wing-store attachments. While structural nonlinearity was present in all cases, steady flow aerodynamic nonlinearity was also included in the F-16 case by the use of a Computational Fluid Dynamics model based on the Reynolds Averaged Navier Stokes (RANS) equations. However, dynamic linearization of the CFD model was done for the present computations. The computationally efficient Harmonic Balance (HB) nonlinear solution technique was a key component of this work, with time marching simulations and closed form solutions being used selectively to confirm the findings of the HB solutions. The simple wing and the generic wing were both modeled as linear beam-rods whose displacements were represented using the primitive modes method. The wing aerodynamic model was linear (quasi-steady for the simple wing and based on the Vortex Lattice Method for the generic wing), and the store aerodynamics were omitted.

The presence of a cubic restoring force (of hardening or softening type, in stiffness or in damping) at the root of the simple wing led to several interesting results and insights. Next, various nonlinear mechanisms including cubic restoring force, freeplay and friction were introduced at the wing-store attachment of the generic wing and these led to a still greater variety in behavior. General relationships were established between the type of nonlinearity and the nature of the resulting response, and they proved very useful for tailoring the F-16 study and interpreting its results.

The Air Force Seek Eagle Office/Air Force Research Laboratory provided a modal structural model of an LCO-prone store configuration of the F-16 aircraft with stores included. In order to investigate a range of stores attachment configurations, the analysis required modification of the stiffness and damping of the wing-store attachment. Since the Finite Element model of the wing and store structure was not available, the modification was achieved by subtracting the store and adding it back with the necessary changes to the store or attachment using a dynamic decoupling/coupling technique. The modified models were subjected to flutter/LCO

analysis using the Duke Harmonic Balance CFD RANS solver, and the resulting flutter boundaries were used in combination with the HB method to derive LCO responses due to the wing-store attachment nonlinearity.

Comparisons were made between the simulation results and the F-16 flight test LCO data. While multiple sources of nonlinearity are probably responsible for the wide range of observed LCO behavior, it was concluded that cubic softening stiffness and positive cubic damping were the more likely structural mechanisms causing LCO, in addition to nonlinear aerodynamics.

This dissertation is dedicated to my wife Triveni and our son Dhyanesh.

Contents

List of Tables

List of Figures

List of Abbreviations and Symbols

Symbols

a	nondimensional distance from midchord to elastic axis
b	semichord
c_1	linear damping coefficient
c_3	cubic damping coefficient
EI	beam bending stiffness
f	frequency
GJ	rod torsion stiffness
h	wing sectional plunge/heave
I_α	wing sectional moment of inertia
I_{α_s}	store moment of inertia about attachment point
I^s_α	store cross moment of inertia about wing elastic axis and attachment point
k_1	linear stiffness coefficient
k_3	cubic stiffness coefficient
m	wing sectional mass
m_s	store mass
q	generalized coordinate
S_α	wing sectional static imbalance about elastic axis
S_{α_s}	store static imbalance about attachment point

U	flow velocity
x	streamwise distance
y	spanwise distance
z	normal distance
α	wing sectional pitch about elastic axis
δ	amplitude of freeplay gap
ϕ, ψ	modeshape
ζ	damping factor

Subscripts and Superscripts

ea, α	elastic axis
s	store, store attachment point
h	bending, plunge, heave
α	torsion, pitch
0	initial condition

Abbreviations

CFD	Computational Fluid Dynamics
DOF	Degree Of Freedom
HB	Harmonic Balance
LCO	Limit Cycle Oscillation
LFS	Linear Flutter Speed
RANS	Reynolds Averaged Navier Stokes
VLM	Vortex Lattice Method

Acknowledgements

The PhD experience has been a wonderful one, for which I must thank many people and acknowledge many things.

First of all my advisor, Professor Earl Dowell of brilliant method and gentle manner. In addition to imparting knowledge and providing insights, his mentoring style subtly reinforces the words of Walt Whitman, "All music is what awakens from you when you are reminded by the instruments,...It is nearer and farther than they." It is a great honor to be associated with Dr Dowell and to have the opportunity to work with him.

I thank Professors Kenneth Hall, Laurens Howle, Donald Bliss, Thomas Witelski and Jeffrey Thomas for being on my dissertation committee, and for their approachability and encouragement. I have benefited from each and every course they taught me. (By a happy coincidence, the courses became available to me in just the right order of sophistication over successive semesters.) A significant part of my dissertation hinges on the CFD results that were generated by Dr Jeff Thomas.

It has been very pleasant to get to know and work with Dr Crystal Pasiliao, my supervisor at the AFRL, Eglin Air Force Base. She (along with my good friend Maciej Rysz) helped me and my family settle in during our first summer at Eglin. She then started me off on a research problem and has been providing professional and personal guidance and support ever since. The funding received from AFOSR Test and Evaluation Portfolio (LRIR 12RW01COR) during the summers of 2012-2014 is

acknowledged. Thanks are also due to Dr Charles Denegri and Dr Vin Sharma, AFSEO for information and helpful discussions regarding the F-16 LCO problem.

I was introduced to Dr Dowell by Dr Gautam SenGupta of Boeing Commercial Aircraft. I am extremely thankful to him for that, and for his guidance and encouragement in matters professional and personal. My long time co-worker and boss, Dr A. R. Upadhya of the Aeronautical Development Agency and subsequently the National Aerospace Laboratories, Bangalore has been a pillar of strength. Among other things, his careful and considerate approach enabled me to acquire a working knowledge of industrial aeroelasticity and aeroservoelasticity even without the academic background that I now possess. I also recall conversations with my brother, Dr A. Ramachandran that have stimulated my thoughts on various social, scientific and philosophical topics.

When my family and I arrived 'out of the blue' at Duke, Dr Geetha of UNC and Professor Ganesan Vaidyanathan of Duke University provided a home away from home and went out of their way to help us make the cultural transition. We are grateful to them for making us a part of their family. Dr Jennifer Parkhurst has been a supportive friend and neighbor, and we greatly appreciate her many acts of assistance and companionship.

Permission given by my employer, the Aeronautical Development Agency, Bangalore to pursue the PhD degree is acknowledged. I also thank my colleagues and friends, Dr E. Hemalatha, Mr R. V. Vaidyanathan, Mr J. V. Kamesh, Mrs Lochana Krishnamurthy, Mr S. R. Venugopalan and Mr R. Sivaramanivas who have been supportive and helpful even across the seas.

We are all linked by intangible threads to numerous others, across miles and years. I acknowledge those unnamed here who have played a role in making me the person that I am today.

1

Introduction

1.1 Background

Aeroelasticity is an important consideration in modern aerospacecraft. Aeroelastic effects can result from linear as well as nonlinear interactions between structure and aerodynamics. In the conventional aircraft context, the well known linear instabilities such as static divergence, flutter and control reversal are usually designed out of the system, hence they are rarely encountered in practice. On the other hand, the nonlinear phenomenon of Limit Cycle Oscillation (LCO) is not usually addressed at the design stage, and is much more likely to be seen in flight. For example, the F-16, the F-18, and other high performance aircraft experience 'store-induced' LCO when they carry certain combinations of under-wing stores [1, 2, 3, 4]. The associated response levels are high enough to cause structural fatigue concerns as well as pilot discomfort and loss of operational effectiveness.

The F-16 exhibits LCO for a wide range of store configurations, and these have been classified into 'typical' and 'nontypical' types based on the response magnitude-Mach number profile (see Fig. 1.1,1.2 taken from [2]). The F-18 LCO behavior

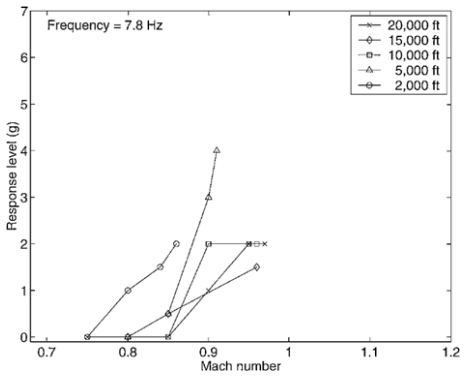

FIGURE 1.1: Typical LCO

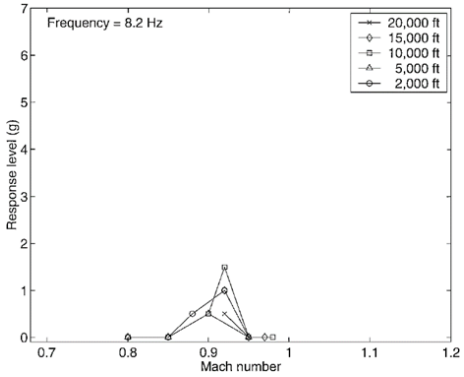

FIGURE 1.2: Nontypical LCO

appears to be more benign in the sense that only one type of LCO is reported. This may be because all of its store stations, other than the wing tip stations, are bunched closer to the wing root when compared to the F-16. Second and third harmonics present in the flight test data indicate the existence of quadratic and cubic nonlinearities in the system [5, 4]. Although several nonlinear mechanisms - structural as well as aerodynamic, have been proposed to explain the observations, their exact roles are not yet well understood. The often considered aerodynamic factors including transonic shock, flow separation and viscous effects can become significant at transonic, or even subsonic, speeds depending on the store geometry. Structural factors such as nonlinear stiffness, freeplay and friction typically exist in built-up structures. Also, stores are attached to the aircraft wing and restrained via non-homogeneous elements such as rails, sliders, hooks, crutch pads, and so on, all of which provide scope for nonlinear response.

The volume of research into aeroelastic LCO in general, and store induced LCO in particular, has been increasing over the years. The state-of-the-art in nonlinear aeroelasticity was surveyed and the relevant literature summarized in [6, 7]. The studies vary in terms of model sophistication (airfoil section/wing/aircraft level models) and analysis method (time marching/perturbation methods/harmonic balance). Many have used the 2-degree of freedom (DOF) airfoil model due to simplicity of

analysis and testing. For example, an airfoil with a rigidly attached store was studied analytically and experimentally in [8]. The system was kinematically nonlinear due to vertical offset between the aerodynamic center, elastic axis and center of mass, and was also constrained by a nonlinear spring in the pitch DOF. The latter nonlinearity turned out to be the dominant cause for LCO.

Three dimensional wings are sometimes represented by the 'typical section' airfoil at 70% semispan, which is acceptable for nearly uniform, high aspect ratio wings according to [9]. But this approximation is not reasonable for most real wings that exhibit spanwise variation of properties, and/or carry stores. It is then necessary to model the entire wing to obtain realistic results. A theoretical and experimental study of LCO in a wing-store combination was reported in [10], where a von Karman nonlinear plate model of the wing was coupled to linear vortex lattice aerodynamics for the wing and slender body aerodynamics for the store. Nonlinearity was also present in the wing-store attachment in the form of freeplay. The effects of various parameters on the LCO response, including freeplay gap, store spanwise location and initial conditions were explored in detail. The dependence of the response on initial conditions was shown to be quite complex.

Modeling an aircraft in its full (nonlinear aeroelastic) glory is of course a much more involved task; it has been attempted to various degrees of fidelity, with mixed results. Notable among these were two attempts to obtain entire LCO response curves as functions of Mach number for the F-16 aircraft. A total of eight different store configurations was studied in [11], which considered aerodynamic nonlinearity by representing the wing geometry accurately and using a RANS solver coupled to the Harmonic Balance method. Some promising correlations were obtained (see Fig. 1.3). An LCO-prone configuration was studied in [12], based on linear aerodynamics, amplitude dependent structural damping and time marching simulations. The damping profile was tuned to match some of the flight test results (see Fig. 1.4).

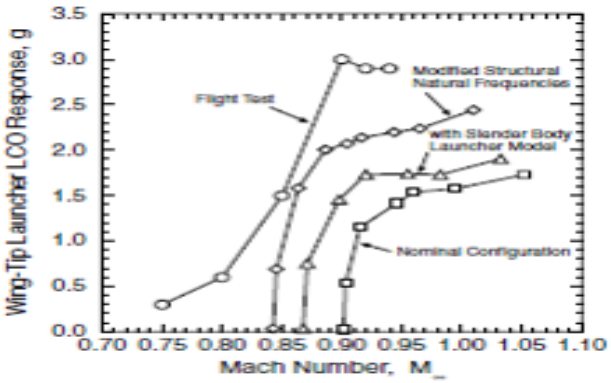

FIGURE 1.3: F-16 result for transonic aerodynamics

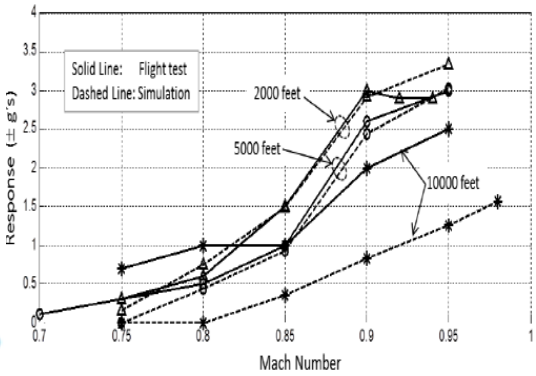

FIGURE 1.4: F-16 result for nonlinear structural damping

In the F-16 LCO studies to date, more detailed attention has been paid to aerodynamic than to structural nonlinearity. For example, attempts have been made to understand how transonic flow patterns could cause and influence LCO by imposing rigid body oscillations on the aircraft CFD model [13]. However, there are clear and repeated instances of LCO at subsonic velocities, where the primary nonlinearity is presumably a structural one. Static structural tests have shown the stiffness of the wing itself to be largely linear [14], however these tests were not designed to capture the mechanical complexity of wing-store connections. Figure 1.5 taken from [15] shows a typical heavy store pylon/weapon rack whose sway braces may sustain intermittent contact when the store vibrates. Ground Vibration Tests have revealed hardening and softening effects at higher excitation levels (e.g., see Fig. 1.6 taken from [16]). The former was attributed to impacts on mechanical stops and the latter to opening of the wing-store connection. Some correlations between LCO occurrence and store inertia properties at wing stations 3/7 may be seen in Figure 4 of [1]. Examples of the effect of store attachment stiffness on flutter velocity can be seen in the F-16 decoupler pylon studies [17].

Studies on the softening effect of freeplay in control surface linkages e.g., [18], [19] have reported excellent agreement between theory, numerical simulation and exper-

FIGURE 1.5: Heavy store pylon/rack

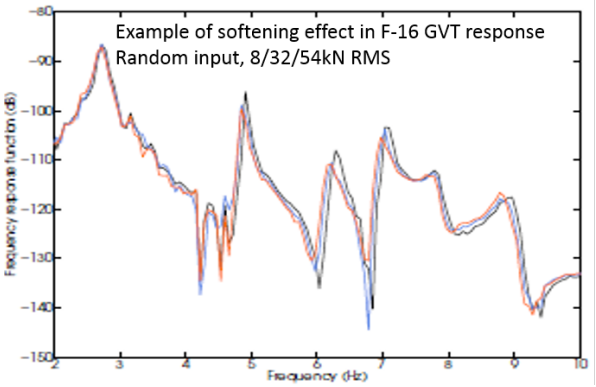

FIGURE 1.6: F-16 GVT response

iment. Also notable was an excercise carried out on the F-22 to establish safe limits for control surface freeplay based on allowable LCO response levels and confirm them by flight testing [20].

1.2 Focus of this Work

We can say that theoretical models currently do not *accurately and reliably* predict the store-induced LCO onset airspeed and magnitude. Indeed, at times the LFS obtained from analysis is imprecise, and therefore it is not possible to say whether the LCO observed in flight is purely supercritical i.e. above the Linear Flutter Speed (LFS) or not. In [2], the V-g curves from F-16 flutter analyses cross zero with shallow slopes, which adds uncertainty to the LFS estimate. In the F-16 case, the usual response to the problem has been to place restrictions on the store carriage envelope based on flight test experience and live with the reduced mission performance. The F-18 does incorporate an LCO controller, which was developed wholly by in-flight testing [21]. Since no suitable analytical LCO model was available, the feedback gain and phase were manually tuned by the test pilots to minimize the response. Thus it is of crucial importance to explore nonlinear aeroelastic phenomena and establish theoretical methods and models whose predictions correlate well with flight

test results. Such a capability will greatly aid the understanding and control of LCO, and contribute to improving the overall design and usage patterns of aircraft.

This work was undertaken to better understand nonlinear aeroelastic phenomena and their relation to classical flutter and divergence, with a particular focus on store-induced LCO in fighter aircraft. The following systems, of graded complexity, were examined.

- A 'simple' wing, with a flexible and nonlinear *root attachment*
- A 'generic' wing, with a flexible and nonlinear *wing-store attachment*
- The F-16 aircraft, with a flexible and nonlinear *wing-store attachment*

While structural nonlinearity was present in all cases, aerodynamic nonlinearity was also included in the F-16 case by the use of CFD to model the underlying steady flow, although dynamic linearization of the CFD model was used for the present computations.

Due to the variety of structural nonlinear mechanisms that may be considered and the lack of systematic techniques to analyze them in a common framework, studies of wing-store attachment nonlinearity as a cause for LCO have been rather ad hoc. Hence, a parallel goal of this work was to carry out the analyses in a computationally efficient way that would be amenable to use in a design and/or certification and flight clearance environment. This was achieved by adopting Harmonic Balance as the primary analysis method, with time marching simulations and closed form solutions being used selectively to confirm the findings.

1.3 Organization of the Thesis

The problem under study is stated in Chapter 1, and the state-of-art and available literature are discussed. Chapter 2 deals with the formulation of the simple wing and

the generic wing models, and also the Harmonic Balance methodology for obtaining LCO responses. Simulation results for the simple wing and the generic wing are provided in Chapter 3 and Chapter 4, respectively. The F-16 model formulation is given in Chapter 5 and the associated results are presented in Chapter 6. Chapter 7 summarizes the work done and lists some promising directions for future research.

2

Simple Wing and Generic Wing Models

This chapter deals with the modeling of a wing-with-store containing a spatially localized structural nonlinearity. Two models, (1) a 'simple wing' with a flexible and nonlinear root attachment and (2) a 'generic wing' with a flexible and nonlinear wing-store attachment were formulated. The parameters listed in Table 2.1 are representative of those used in the simulations, and were arrived at by modifying the properties of the 2D airfoil system of [8].

2.1 Structural Modeling

The wing was represented by a beam-rod with spanwise varying plunge, $h(y,t)$ and pitch, $\alpha(y,t)$ as shown in Figs. 2.1, 2.2. This is a reasonably realistic approximation since airfoil sections are often the most rigid sections in a wing. The equations of motion may be derived from a fundamental approach such as Hamilton's principle. For a linear wing model, these are the partial differential equations given in Eqn. 2.1 where the wing sectional properties, namely mass/span (m), moment of inertia/span (I_α) & static imbalance/span (S_α) with respect to wing elastic axis, bending stiffness (EI) and torsional stiffness (GJ) may vary along the span.

Table 2.1: Wing model properties

	Wing	Store
Geometry	$b = 0.1064\,m$ $a = -0.4$ $L = .6\,m$	Attachment point: $0.01\,m$ aft of LE, 70% span
Inertia	$m = 11.066\,kg/m$ $S_\alpha = 0.830\,kg$ $I_\alpha = 0.074\,kgm$	$m_s = 1.955\,kg$ $S_{\alpha_s} = 0.104\,kgm$ $I_{\alpha_s} = .00544\,kgm^2$
Stiffness	$EI = 49.77\,Nm^2$ $GJ = 5 - 100\,Nm^2/rad$ Root spring $k_1 = 6.861\,Nm/rad$ $k_3 = 663.29\,Nm/rad^3$	$K_{h_s} = 250\,N/m$ $K_{\alpha_s} = 2.5\,Nm/rad$
Modal damping, ζ	$\approx 2\%$	$\approx 2\%$

$$m(y)\ddot{h} + S_\alpha(y)\ddot{\alpha} + (EI(y)h'')'' = -L(y,t) \tag{2.1a}$$

$$S_\alpha(y)\ddot{h} + I_\alpha(y)\ddot{\alpha} - (GJ(y)\alpha')' = M_y(y,t) \tag{2.1b}$$

In this work however, the Rayleigh-Ritz approach was adopted in combination with the primitive modes method as described in [22, 23]. This is a convenient and powerful way to handle non-uniform wings with sweep, taper and stores at multiple spanwise stations. (In the present work, the wing models were unswept and without taper.) The number of primitive modes used is variable, and the minimum number needed for actionable accuracy depends on the level of static imbalance and on how the wing deviates from spanwise uniformity. Thus, h and α were expressed in terms of the bending eigenmodes, $\phi_k^h(y)$ and torsional eigenmodes, $\phi_n^\alpha(y)$ of a uniform beam and rod respectively (Eqn. 2.2) and these were substituted into the kinetic and elastic potential energy expressions for the wing-with-store. Application of Lagrange's equations with respect to the generalized coordinates $q_k^h(t)$, q_k^α (and also the store DOF in the case of the generic wing) yielded a system of ordinary differential equations.

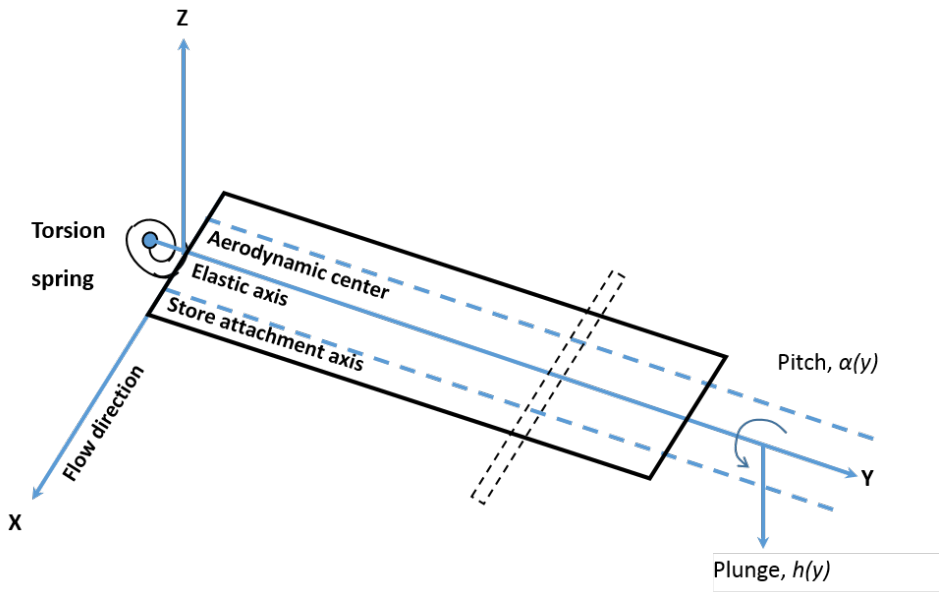

FIGURE 2.1: Simple wing schematic

$$h(y,t) = \sum_{1}^{K} q_k^h(t)\phi_k^h(y) \tag{2.2a}$$

$$\alpha(y,t) = \sum_{1}^{N} q_n^\alpha(t)\phi_n^\alpha(y) \tag{2.2b}$$

2.1.1 Simple Wing: Nonlinear Wing Root

Since the wing root could rotate (subject to a stiffness/damping constraint), the appropriate primitive modes were used, namely the free-free modes in torsion including the rigid-body mode, and the clamped-free modes in bending (Fig. 2.3). The store was rigidly attached at 70% semispan and was considered an integral part of the wing in deriving Equation 2.3.

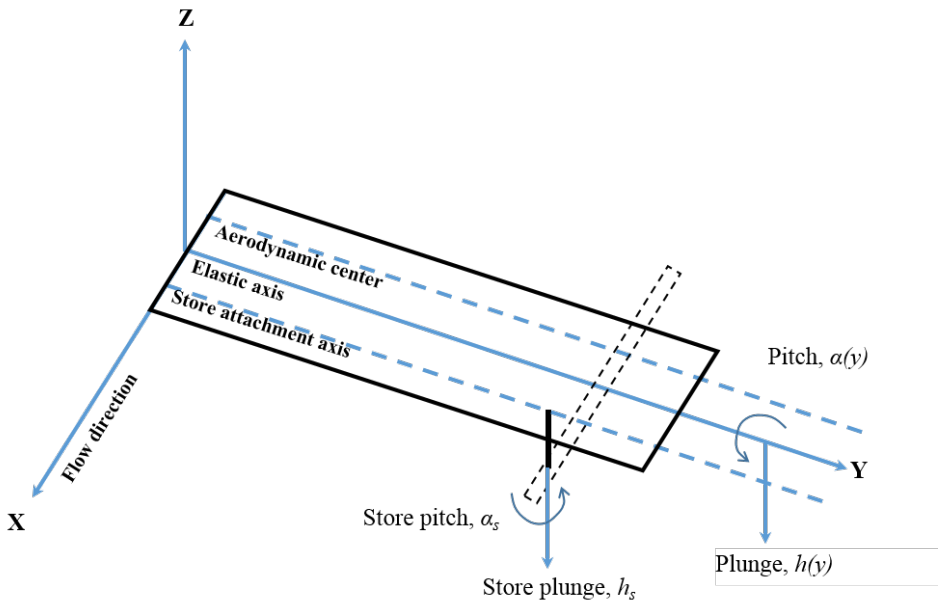

FIGURE 2.2: Generic wing schematic

$$\begin{bmatrix} M^{hh} & M^{\alpha h} \\ M^{h\alpha} & M^{\alpha\alpha} \end{bmatrix} \begin{Bmatrix} \ddot{q}_k^h \\ \ddot{q}_n^\alpha \end{Bmatrix} + \begin{bmatrix} C^{hh} & 0 \\ 0 & C^{\alpha\alpha} \end{bmatrix} \begin{Bmatrix} \dot{q}_k^h \\ \dot{q}_n^\alpha \end{Bmatrix} + \begin{bmatrix} K^{hh} & 0 \\ 0 & K^{\alpha\alpha} \end{bmatrix} \begin{Bmatrix} q_k^h \\ q_n^\alpha \end{Bmatrix}$$
$$+ \begin{Bmatrix} 0 \\ k_1 \left(\sum_1^N \phi_r^\alpha(0) q_r^\alpha \right) \phi_n^\alpha(0) \end{Bmatrix} + \begin{Bmatrix} 0 \\ k_3 \left(\sum_1^N \phi_r^\alpha(0) q_r^\alpha \right)^3 \phi_n^\alpha(0) \end{Bmatrix} = \begin{Bmatrix} -L_k^h \\ M_n^\alpha \end{Bmatrix} \tag{2.3}$$

where

$$M^{hh} = \int_0^l m(y)\phi_r^h \phi_s^h dy \qquad r, s = 1, 2, \ldots, K$$

$$M^{\alpha\alpha} = \int_0^l I_\alpha(y)\phi_r^\alpha \phi_s^\alpha dy \qquad r, s = 1, 2, \ldots, N$$

$$M^{\alpha h} = \int_0^l S_\alpha(y)\phi_r^\alpha \phi_s^h dy \qquad r = 1, 2, \ldots, N; s = 1, 2, \ldots, K$$

$$K^{hh} = \int_0^l EI(y) \frac{d^2\phi_r^h}{dy^2} \frac{d^2\phi_s^h}{dy^2} dy \qquad r, s = 1, 2, \ldots, K$$

$$K^{\alpha\alpha} = \int_0^l GJ(y) \frac{d\phi_r^\alpha}{dy} \frac{d\phi_s^\alpha}{dy} dy \qquad r, s = 1, 2, \ldots, N$$

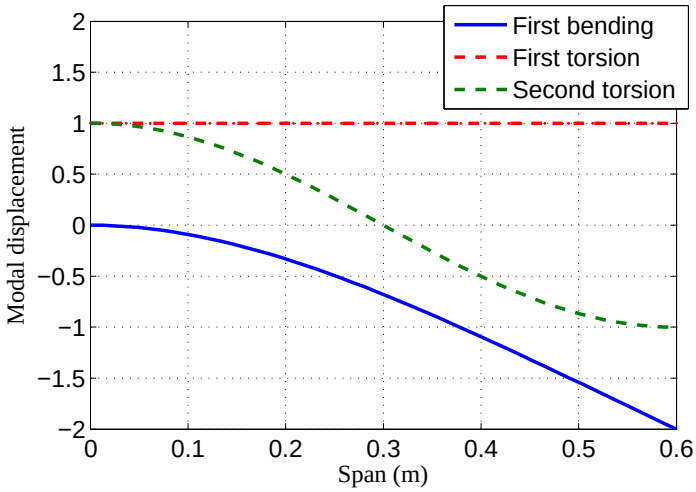

FIGURE 2.3: Primitive modeshapes for the simple wing

and the forcing is from the aerodynamics.

To ensure the LCO tendency was present, the wing model was made mathematically equivalent to the original typical section model by using exactly one bending mode ($K = 1$) and one torsion mode ($N = 1$) and its properties were tuned to recover the original structural frequencies as closely as possible.

2.1.2 Generic Wing: Nonlinear Wing-Store Attachment

The root of the generic wing was clamped, hence the appropriate primitive modes in torsion were now the fixed-free modes of a uniform rod, rather than the free-free modes used for the simple wing. Making the wing-store attachment flexible led to two additional DOF, namely store plunge, $h_s(t)$ and pitch, $\alpha_s(t)$ relative to the wing (see Fig. 2.2). The resulting formulation is given by Eqn. 2.4, where y_s and z_s are store spanwise location and z-offset; m_s, S_{α_s} and I_{α_s} are the store mass, static imbalance and moment of inertia with respect to x_s; S^s_α is the store static imbalance with respect to wing elastic axis; I^s_α is the store cross moment of inertia with respect to x_s and wing elastic axis, also expressible as $I_{\alpha_s} + S_{\alpha_s}(x_s - x_{ea})$; and

$$M_s^{\alpha\alpha} = m_s \phi_r^{\alpha}(y_s)\phi_s^{\alpha}(y_s) \quad for \quad r, s = 1, 2, \ldots, N.$$

$$\begin{bmatrix} M^{hh} & M^{\alpha h} & m_s\phi_k^h(y_s) & S_{\alpha_s}\phi_k^h(y_s) \\ M^{h\alpha} & M^{\alpha\alpha} + M_s^{\alpha\alpha} z_s^2 & S_\alpha^s \phi_n^\alpha(y_s) & I_\alpha^s \phi_k^h(y_s) \\ m_s\phi_k^h(y_s) & S_\alpha^s \phi_n^\alpha(y_s) & m_s & S_{\alpha_s} \\ S_{\alpha_s}\phi_k^h(y_s) & I_\alpha^s \phi_k^h(y_s) & S_{\alpha_s} & I_{\alpha_s} \end{bmatrix} \begin{Bmatrix} \ddot{q}_k^h \\ \ddot{q}_n^\alpha \\ \ddot{h}_s \\ \ddot{\alpha}_s \end{Bmatrix}$$

$$+ \begin{bmatrix} K^{hh} & 0 & 0 & 0 \\ 0 & K^{\alpha\alpha} & 0 & 0 \\ 0 & 0 & K_{h_s} & 0 \\ 0 & 0 & 0 & K_{\alpha_s} \end{bmatrix} \begin{Bmatrix} q_k^h \\ q_n^\alpha \\ h_s \\ \alpha_s \end{Bmatrix} = \begin{Bmatrix} -L_k^h \\ M_n^\alpha \\ -L_s \\ M_s \end{Bmatrix} \quad (2.4)$$

2.1.3 Structural Nonlinearity and the Harmonic Balance Method

Introduction of nonlinearities at the root (of the simple wing) and the store attachment (of the generic wing) led to additional terms in Eqns. 2.3 and 2.4 respectively.

Time marching of the governing equations is generally the most straightforward way to obtain a nonlinear response. However, this can become a computationally intensive, hit-or-miss process when looking for flutter or LCO in a realistic aircraft (or even wing) model. Harmonic Balance (HB) can be a much more efficient technique, especially when the models are of high dimension. In this work, a concise 3-step HB method suitable for separable/spatially localized nonlinearities was used.

- First, a series of linear flutter analyses were conducted for various levels of stiffness or damping (whichever was nonlinear) and the flutter velocity (and frequency) boundary was drawn.

- Next, simple harmonic motion of the form, $x(t) = \bar{x}\cos(\omega t)$ was assumed in the nonlinear DOF and the first term in the Fourier series of the resulting restoring force was calculated. This term yielded the effective stiffness/damping of the nonlinear element as a function of LCO amplitude, $\bar{x}$.

- Finally, the flutter boundary and the effective stiffness/damping curve were combined to obtain the LCO amplitude and frequency as functions of flow velocity. Since both these curves had stiffness/damping as a common axis, all that was required was to plot $\bar{x}$ against flutter velocity for various chosen values of k_{eff} (or c_{eff}). The LCO frequency curve was similarly obtained by plotting flutter frequency against flutter velocity for various chosen values of k_{eff} (or c_{eff}). In cases of nonlinear *damping*, the effective damping depended on the frequency as well as amplitude, hence the flutter frequency curve was also used in calculating $\bar{x}$.

An important and valuable aspect of HB is that it yields unstable as well as stable LCO branches, and a perturbation analysis is usually done for each branch of interest to assess its stability. In the present method, LCO stability was determined by a simpler, calculation-free procedure that required only the visual inspection of relevant segments of the flutter boundary and the effective stiffness/damping curve. (see Section 3.1.5 for details.) Another benefit of the method is that the same flutter boundary can be used to generate a family of LCO response curves corresponding to different base linear stiffness/damping values.

The HB method does rely on the assumption that the response is dominated by a small number of harmonics. (This work uses the one/two harmonic approximation depending on whether the zeroth harmonic is excluded or included.) Continuation methods such as that implemented in the software AUTO [24] do not make this assumption. However their use is generally restricted to moderate system sizes on the order of a hundred equations, and that would be possible only with simplified aerodynamics. On the other hand, the HB method outlined here is compatible with very high dimensional models such as full aircraft CFD models.

Effective stiffness/damping can be derived from the nonlinear restoring force

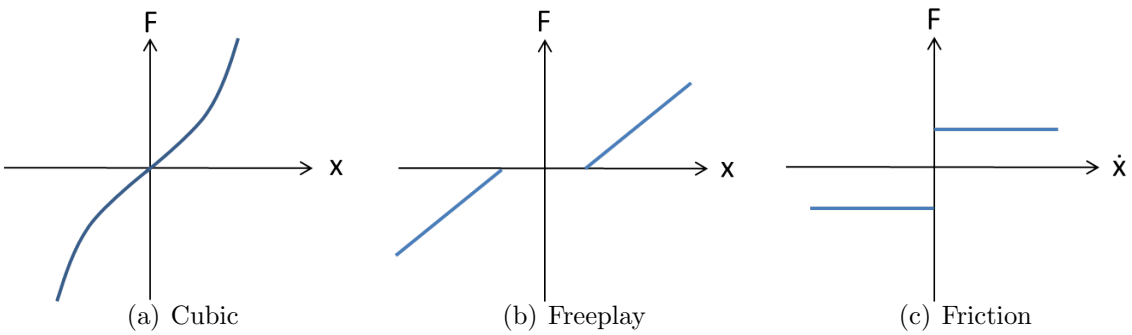

(a) Cubic (b) Freeplay (c) Friction

FIGURE 2.4: Nolinear restoring force

and expressed in terms of a dimensionless Describing Function (DF) such that $k_{eff} = k_1 DF$, $c_{eff} = c_1 DF$. For the nonlinearities considered here, the restoring force profiles are shown in Fig. 2.4. The corresponding DF are listed in Table 2.2 and plotted in Fig. 2.5.

Table 2.2: Nonlinearities and their describing functions

Type	Restoring force	DF	Scaling, $S = x/x_{ND}$
Cubic stiffness	$k_1 x + k_3 x^3$	$1 + \frac{3}{4}\frac{k_3}{k_1}\bar{x}^2$	$\sqrt{\frac{k_1}{k_3}}$
Cubic damping	$c_1\dot{x} + c_3\dot{x}^3$	$1 + \frac{3}{4}\frac{c_3}{c_1}(\omega\bar{x})^2$	$\frac{1}{\omega_{ref}}\sqrt{\frac{c_1}{c_3}}$
Freeplay stiffness	$k_1(x \pm \delta),\ \lvert x\rvert > \delta$	$1 - \frac{1}{\pi}[2\tau + \sin(2\tau)]$	δ
	0, otherwise	where $\tau = sin^{-1}(\frac{\delta}{\bar{x}})$	
Freeplay damping	$c_1\dot{x}\ for\ \lvert x\rvert > \delta$	Same as above	Same as above
	0, otherwise		
Coulomb friction	$F_d sgn(\dot{x})$	$1 + \frac{4}{\pi}\frac{F_d}{c_1\omega\bar{x}}$	$\frac{F_d}{c_1\omega_{ref}}$
damping			

Clearly, cubic restoring force is more important for large $\bar{x}$ whereas freeplay and

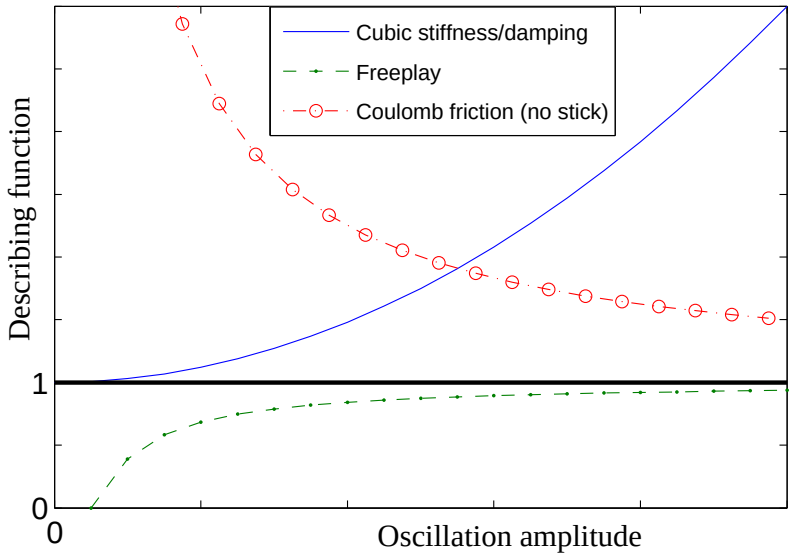

FIGURE 2.5: Nonlinearities and their describing functions

friction effects are most significant for small $\bar{x}$. A comparison of the first and third harmonics of the restoring force for freeplay indicates that the nonlinear effects will be strongest for $\bar{x} \approx \delta$ (Fig. 2.6). For the freeplay analyses in [20], use has been made of the Den Hartog (DH) equivalent stiffness given in Eqn. 2.5. The DH expression has been obtained in [25] by assuming constant velocity within the freeplay gap and pure harmonic motion outside of it, calculating the total time period and converting it into a equivalent stiffness. Though the expressions for the DH and HB stiffnesses differ, the actual profiles were found to match closely.

$$k_{DH} = k_1/[1 + \frac{2}{\pi}\frac{\delta}{\bar{x} - \delta}]^2 \tag{2.5}$$

Scale factors (S, such that $x = Sx_{ND}$) to non-dimensionalize the LCO responses and make them *O(1)* are also tabulated. In exceptional cases where the given DF and scaling are undefined, the basic HB result will still be applicable, e.g., for pure friction damping with $c_1 = 0$, $c_{eff} = (4/\pi)F_d/(\omega\bar{x})$.

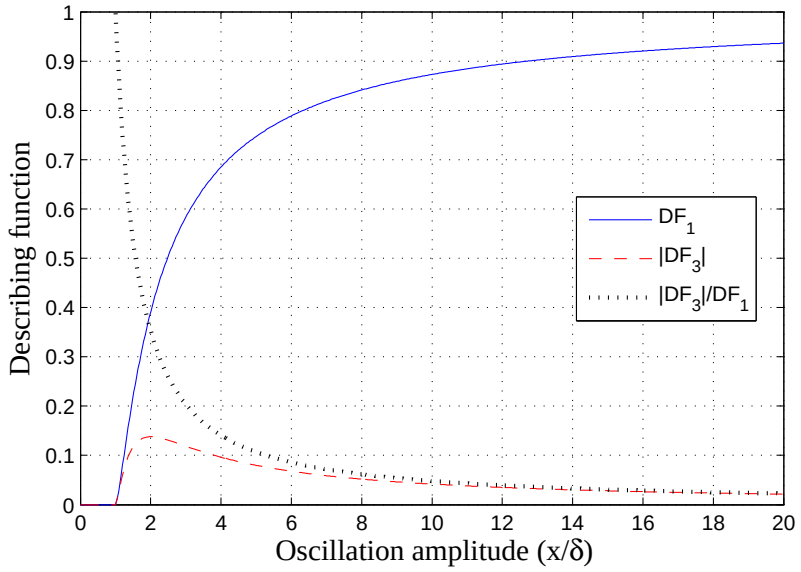

FIGURE 2.6: Freeplay harmonics

Velocity-squared damping is qualitatively somewhat similar to the tabulated cubic damping case, with a restoring force of $c_1\dot{x} + c_2\dot{x}|\dot{x}|$ and a DF of $1 + \frac{8}{3\pi}\frac{c_2}{c_1}(\omega\bar{x})$.

Note that the HB method can be used to map the static divergence boundary of the linear system to a nonlinear static equilibrium/'static LCO' curve, just as the flutter boundary is mapped to a dynamic LCO curve. In such cases, the DF for cubic stiffness is $[1 + (k_3/k_1)\bar{x}^2]$ (i.e., without the factor of 3/4) and for freeplay it is $[1 - sin(\tau)]$. Nonlinear damping cannot give rise to a static LCO.

It is straightforward to extend the HB method outlined here to account for certain additional effects. For example, if more than one type of nonlinearity exists in either the stiffness or the damping of a single DOF - say cubic stiffness and freeplay in α_s, they can be combined into a single DF. If two different DOF are involved, it will be necessary to construct a 2-dimensional flutter boundary by varying paramers in each DOF independently. If both stiffness and damping are nonlinear but restricted to a single DOF, a 2-dimensional flutter boundary may still be required. The inclusion

of a static preload along with a cubic nonlinearity is discussed in Section 4.5.2.

2.2 Aerodynamic Modeling

2.2.1 Simple Wing: Quasisteady Aerodynamics

A quasisteady form of linear potential flow aerodynamics, suitable for high aspect ratio wings at low reduced frequencies, was applied in 2D (stripwise) fashion to the simple wing. For this Theodorsen's equations [9] were simplified by (i) ignoring the wake effects by setting the Theodorsen function, $C(k)$ to unity and (ii) omitting the apparent mass terms. The resulting aerodynamic forces were proportional to the downwash at the three-quarter-chord point, as given by Eqn. 2.6 where $\alpha_{eff} = \alpha + \dot{h}/U + b(\frac{1}{2} - a)\dot{\alpha}/U$.

$$L = \rho U^2 b S C_{L\alpha} \alpha_{eff} \tag{2.6a}$$

$$M_y = \rho U^2 b^2 S C_{L\alpha} \alpha_{eff} (\frac{1}{2} + a) \tag{2.6b}$$

The forcing terms in Eqn. 2.3 were obtained from Eqn. 2.7.

$$L_k^h = \int_0^l L \phi_k^h dy \quad ; \quad M_n^\alpha = \int_0^l M_y \phi_n^\alpha dy \tag{2.7}$$

2.2.2 Generic Wing: Vortex Lattice Method

The linear Vortex Lattice Method (VLM) was applied to the generic wing. While VLM accounts for fully unsteady flow and spanwise aerodynamic induction effects, it is restricted to subsonic velocities because of its incompressible flow assumption. The VLM code was developed based on the formulation given in [26]. First, the time domain aerodynamic version applicable to a thin 2D airfoil was coded in MATLAB. This was validated by reproducing the Wagner function[1] in response to a step change

[1] The inverse Fourier transform of the Theodorsen function

in the angle of attack (Fig. 2.7). Next, VLM was coupled to the wing structural

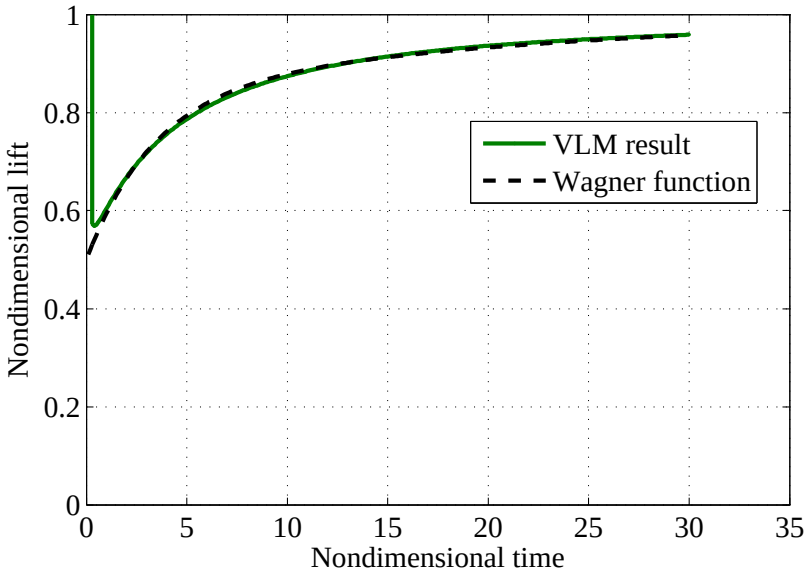

FIGURE 2.7: Airfoil lift due to step change in the angle of attack

model in 2D stripwise fashion to create the aeroelastic version of the code. Flutter calculations were performed using Theodorsen theory as well as VLM to confirm that the unsteady flow had been modeled properly (Fig. 2.8). Deviations were noticed at low flow velocities due to inadequate capture of flow unsteadiness, and this was overcome by finer discretization in time and space. Finally, the 2D VLM kernel was replaced by the 3D kernel [26] to include the spanwise aerodynamic induction effect. The VLM grid is shown in Fig. 2.9. The store aerodynamics was not modeled therefore $L_s = M_s = 0$ in Eqn. 2.4.

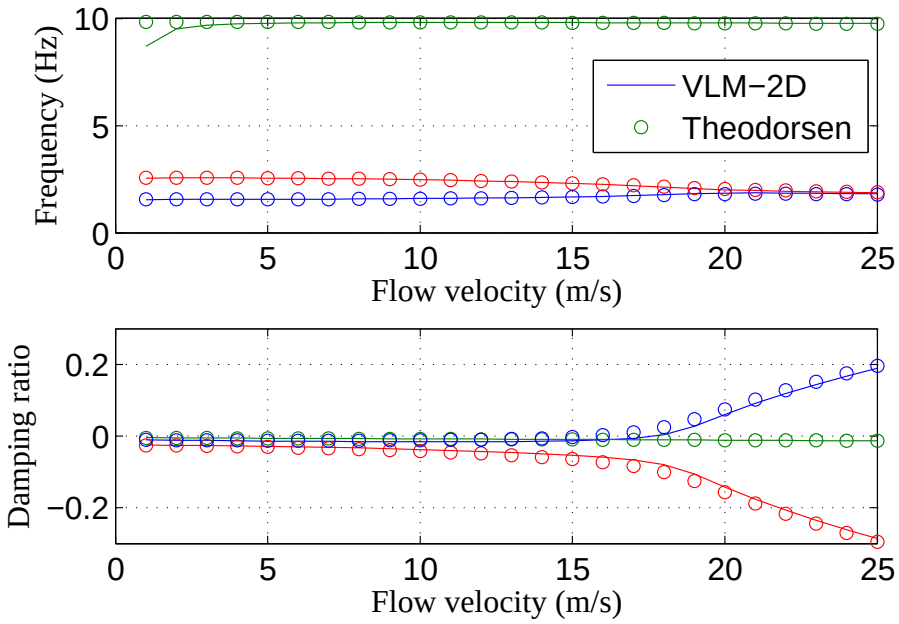

FIGURE 2.8: Wing flutter results with fully unsteady aerodynamics

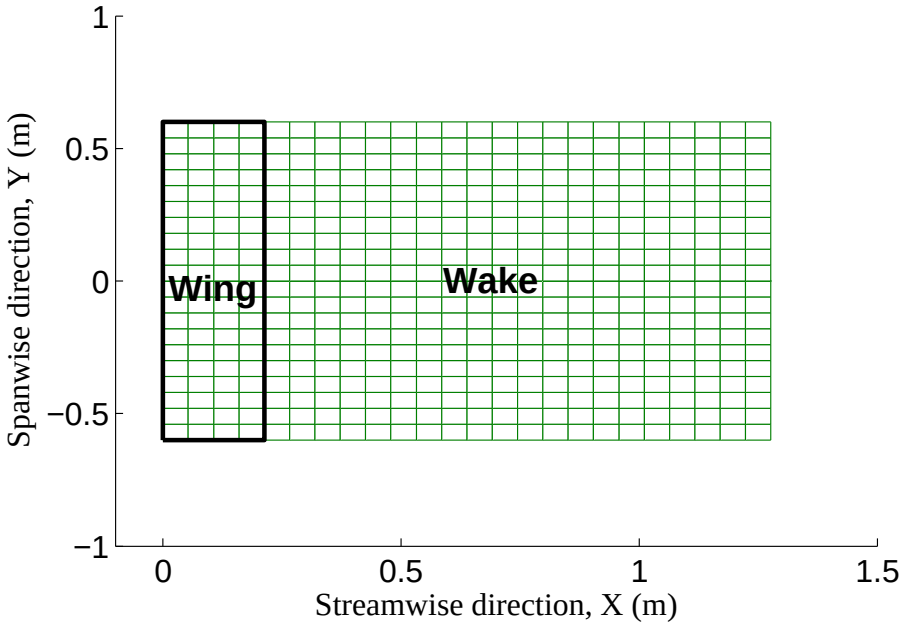

FIGURE 2.9: VLM grid for generic wing

3

Simple Wing Results

This chapter documents how the presence of a localized cubic stiffness/damping at the root of an aircraft wing can influence its aeroelastic behavior. Quasisteady aerodynamics of the form described in Section 2.2.1 was assumed. First, the linearized system was considered, and its structural dynamic and aeroelastic characteristics were obtained using eigenanalysis. Then, the nonlinear system was studied via time marching, Harmonic Balance and sometimes by solution of closed form equations. The various forms of LCO observed were correlated to the properties of the underlying linear system.

The results discussed here pertain mainly to two models abbreviated as B1T1 and B1T2, which differ in the number of structural modes included.[1]. B1T1 was the smallest model that could exhibit mode coalescence flutter when linearized, and consquently aeroelastic LCO when the nonlinearity was retained. With one bending mode and one (rigid) torsion mode, it was mathematically equivalent to a beam-rod with infinite GJ. On the other hand, the B1T2 model had an elastic torsion mode and therefore the value of GJ had a bearing on the results. While B1T2 provided

[1] BxTy means x primitive bending modes and y primitive torsion modes

a better representation of a fixed wing, B1T1 could be considered to mimic an all-moving control surface.[2]

3.1 B1T1 Model

Table 3.1 lists four cases of B1T1 with with hardening cubic stiffness. Two kinds of cases were discernible based on the in-vacuo frequencies of the linearized system in bending, ω_b and torsion, ω_t. In Cases I and III, $\omega_b > \omega_t$ and in Cases II, IV, the converse was true. Either situation is conceivable in real aircraft, expecially when stores are carried on the wing.

Table 3.1: Summary of B1T1 results

Case	$\frac{k_1}{k_{1nominal}}$	Torsion frequency (Hz)	Bending frequency (Hz)	Flutter speed (m/s)	LCO hysteresis
I	1	1.85	2.14	16.70	Yes
II	2	2.67	2.10	15.05	No
III	0.98[3]	1.83	2.14	18.92	Yes
IV	3	3.26	2.11	23.01	No

3.1.1 Case I: Base Aeroelastic System

The base aeroelastic system, with a wing root stiffness of k_1 in torsion, was characterized by generating the aeroelastic eigenvalues as a function of flow velocity. The V-g/V-f plots (Fig. 3.1) showed torsion mode flutter at a Linear Flutter Speed (LFS) of 16.7 m/s. Since the damping curve returned to the stable side a little beyond 25 m/s, this was a case of 'hump mode' flutter.

Next, a cubic term, k_3 was added to the torsion spring and the root restoring

[2] Reduction in frequency of the first torsion mode due to freeplay, and its impact on flutter/LCO, are important for actuation system design in all-moving surfaces.

[3] Lower k_1 led to static divergence instead of flutter; this has been experimentally observed in an all-moving horizontal stabilizer [27]

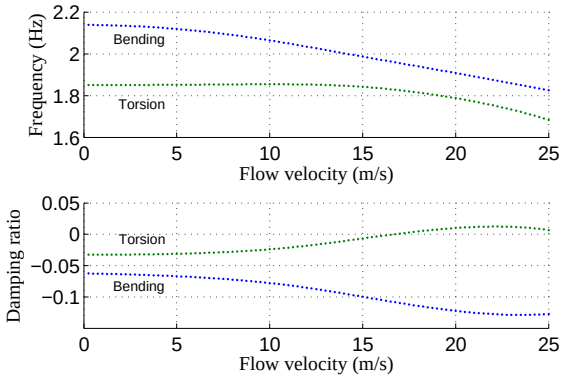

FIGURE 3.1: Linear flutter results - Case I

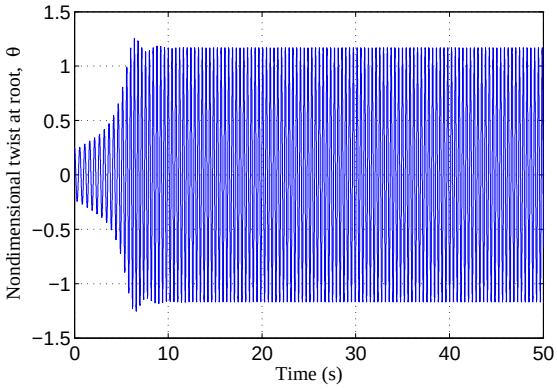

FIGURE 3.2: Nonlinear response, flow velocity = 15 m/s

force in torsion became

$$F(t) = k_1\alpha(y=0,t) + k_3\alpha^3(y=0,t) = k_1\alpha(1+\frac{k_3}{k_1}\alpha^2) \tag{3.1}$$

Based on Eqn. 3.1 the small magnitude LCO was inferred to be $O(\sqrt{k_1/k_3})$, hence a non-dimensional coordinate, θ given by the relation, $\alpha = (\sqrt{k_1/k_3})\theta$ was introduced and the equations of motion were rewritten accordingly. The LCO magnitude in terms of θ was expected to be insensitive to k_3 per se as well as $O(1)$. However, it would depend on k_1 because the linear flutter behavior - from which the nonlinear LCO behavior may be considered a perturbation, was itself a function of k_1.

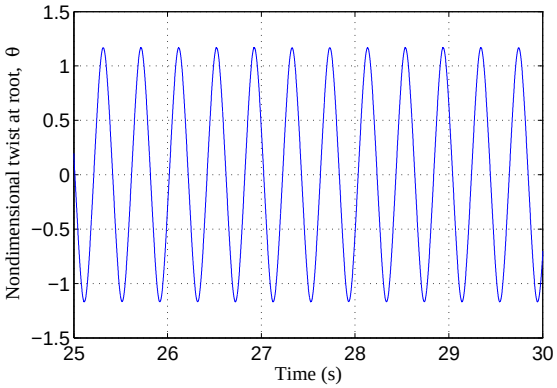

FIGURE 3.3: Steady LCO segment

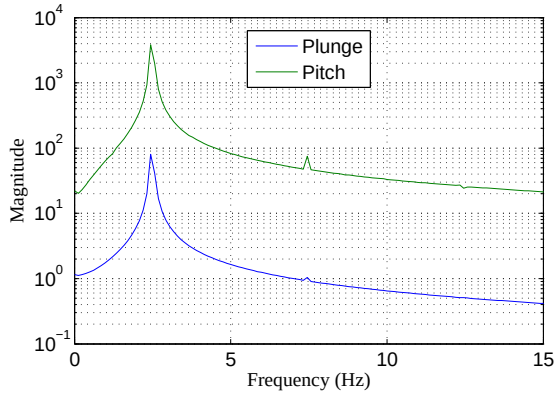

FIGURE 3.4: FFT of LCO segment

Time marching the nonlinear system with nonzero initial pitch, θ_0 at various fixed flow velocities (using MATLAB's 4th order Runge-Kutta solver, *ode45*) yielded responses that either died down completely, or settled into an LCO upon decay of the initial transient. Figure 3.2 shows an LCO time history at a flow velocity of 15 m/s - a 'subcritical' LCO since it occurred below the LFS. The expanded view of the LCO waveform (Fig. 3.3) appeared to be sinusoidal. However the frequency spectrum (Fig. 3.4) revealed the presence of $3f$ and $5f$ higher harmonics caused by the cubic stiffness.

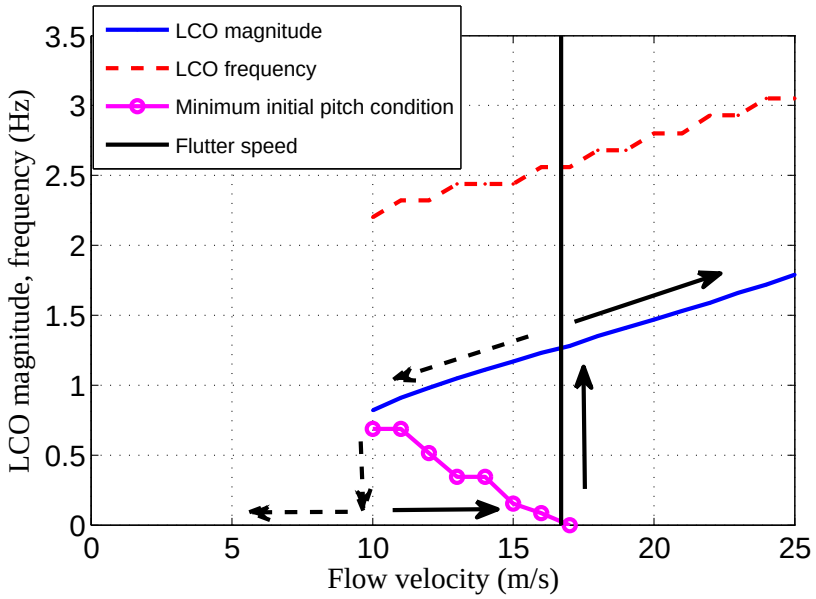

FIGURE 3.5: LCO response - Case I

LCO magnitude and frequency were plotted against flow velocity (Fig. 3.5), and the magnitude was $O(1)$ as anticipated. Since the LCO was partly subcritical, the causative nonlinearity can be labeled as 'detrimental' according to [7]. Arrows placed in the plot indicate the hysteresis loop that would be traced if one were to increase and then decrease the flow velocity. The minimum speed for LCO to occur was roughly half the LFS at about 10 m/s. Below the LFS, a minimum θ_0 was required

to initiate LCO - still smaller θ_0 led to a (sometimes non-exponentially) decaying response. Above the LFS, any small θ_0 was adequate to initiate LCO. The LCO frequency increased with magnitude as a result of the hardening stiffness ($k_3 > 0$).

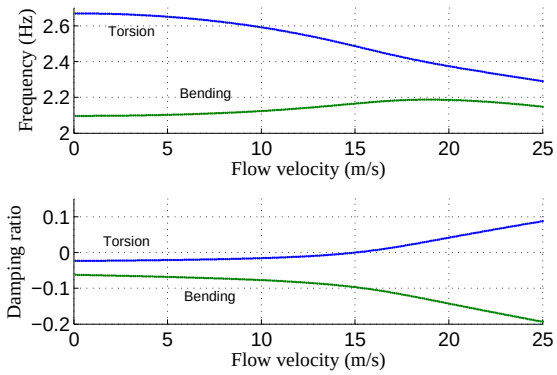

FIGURE 3.6: Flutter results - Case II

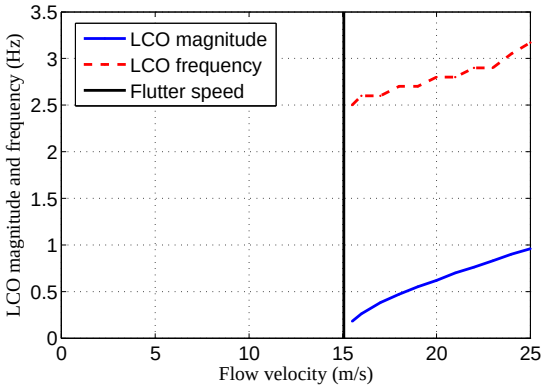

FIGURE 3.7: LCO response - Case II

3.1.2 Case II: Effect of Frequency Ordering on LCO Behavior

In Case I, ω_t was less than ω_b and this was thought to be the cause of the subcritical LCO. Therefore for Case II, ω_t was raised above ω_b by doubling k_1 while keeping the ratio k_1/k_3 the same. The resulting linear aeroelastic behavior was similar to that of Case I, with the torsion mode fluttering at 15.05 m/s (Fig. 3.6). However, the nonlinear behavior was quite different - the LCO was wholly supercritical and the hysteresis went away (Fig. 3.7).

3.1.3 Cases III and IV: Effect of Flutter Speed on LCO Behavior

Two additional cases (III and IV) were considered, with both exhibiting higher flutter speeds than the preceding cases. Their LCO responses are plotted in Fig. 3.8 3.9 respectively. (The linear aeroelastic eigenvalue trends were qualitatively similar to the preceding cases and are not provided here.) Among the four cases considered, LCO hysteresis existed for Cases I and III, i.e., when $\omega_t < \omega_b$. Upon superposing the results (Fig. 3.10), it was seen that the minimum flow velocity for LCO to exist

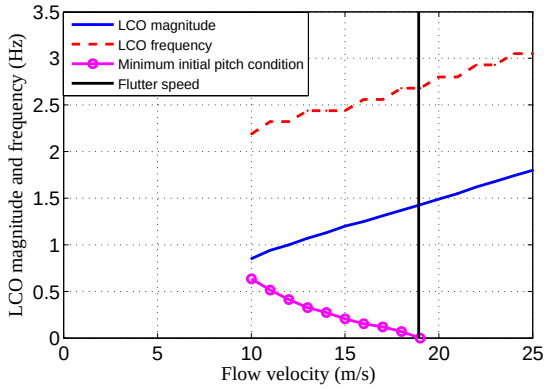

FIGURE 3.8: LCO response - Case III

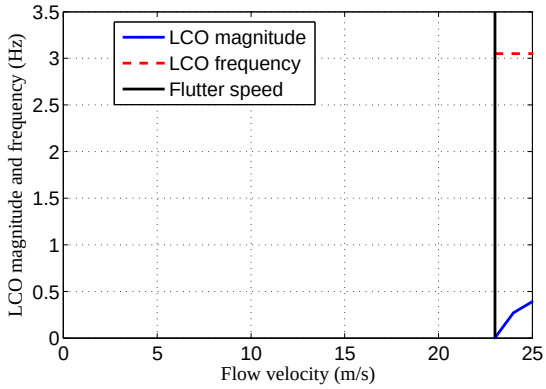

FIGURE 3.9: LCO response - Case IV

was the same for both cases whereas the minimum θ_0 required to enter LCO went to zero at the case-specific LFS.

In the literature (e.g., [28]), LCO hysteresis is more often linked to freeplay and the associated stiffness reduction rather than to cubic stiffness. However, the above results show that a *hardening* stiffness can also lead to LCO hysteresis, depending on the ordering of ω_b and ω_t. This nature of this dependence is discussed next.

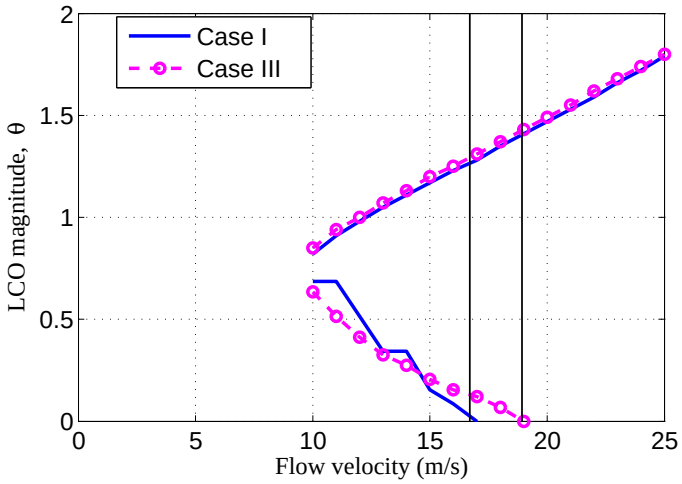

FIGURE 3.10: Comparison of LCO pitch magnitudes for Cases I and III

3.1.4 Stiffness-Flutter Velocity Dependence and its Relevance to LCO

Returning to Case I, the LFS and flutter frequency were calculated as functions of k_1 and these are shown in Fig. 3.11. When they were considered along with the in-vacuo frequency separation between the modes ($\Delta\omega = |\omega_t - \omega_b|$), the following interesting facts emerged. The LFS reached its minimum value when the in-vacuo frequencies were very close to each other, at $k_1/k_{1nominal} = 1.3$. Cases I, III fell to the left of the minimum point ($\omega_t < \omega_b$) while Cases II and IV fell to the right of the minimum ($\omega_t > \omega_b$). The minimum flow velocity at which LCO could occur in Cases I, III was the LFS minimum of 9.24 m/s.

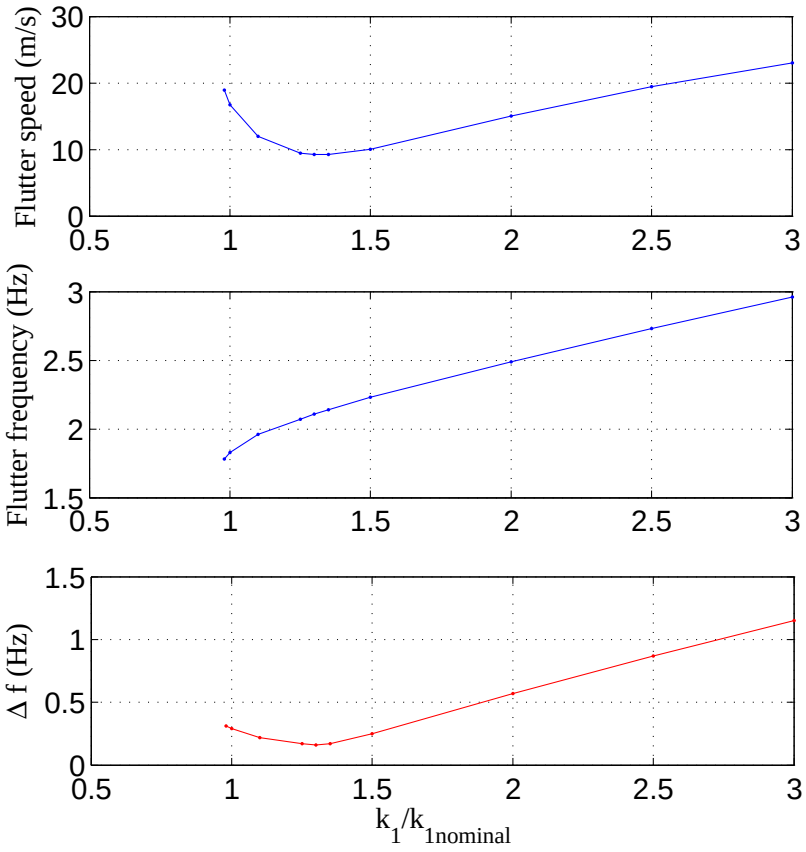

FIGURE 3.11: Variation of flutter speed and frequency separation with stiffness, k_1

3.1.5 Harmonic Balance Results

The k_{eff} for cubic stiffness (see Table 2.2) was derived as follows. The system was assumed to undergo harmonic oscillations and the expression, $\alpha = \bar{\alpha}\cos\omega t$ was inserted into the restoring force of Eqn. 3.1. The Fourier series for the cubic term contained two harmonics, as Eqn. 3.2 shows. The higher harmonic was truncated and k_{eff} was obtained as a function of oscillation amplitude (Eqn.3.3, Fig. 3.12).

$$\cos^3(\omega t) = \frac{3}{4}\cos(\omega t) + \frac{1}{4}\cos(3\omega t) \tag{3.2}$$

$$k_{eff} = k_1 + \frac{3}{4}k_3\bar{\alpha}^2 = k_1\left(1 + \frac{3}{4}\bar{\theta}^2\right) \tag{3.3}$$

The LCO (magnitude) curve of Fig. 3.13 was obtained by cross-plotting the upper curve in Fig. 3.11 against Fig. 3.12. The stable branch precisely matched the time marching solution but is expected to deviate at higher magnitudes, when the nonlinearity is stronger and the one-harmonic assumption breaks down. The unstable branch happened to lie close to the minimum θ_0 required to cause LCO in the time marching. We note that the unstable branch given by HB is a *system property* whereas the θ_0 (only) condition obtained from time marching is not; a precise match would require a specific combination of θ_0 and h_0 dictated by the flutter eigenvector. The LCO frequency curve (Fig. 3.14) was obtained similarly by cross-plotting the upper and middle curves in Fig. 3.11.

3.2 B1T2 Model

3.2.1 System with Nominal Root Stiffness

The presence of an elastic torsion mode brought GJ into the B1T2 model, and its effect on the in-vacuo torsion frequencies can be seen in Fig. 3.15. As GJ

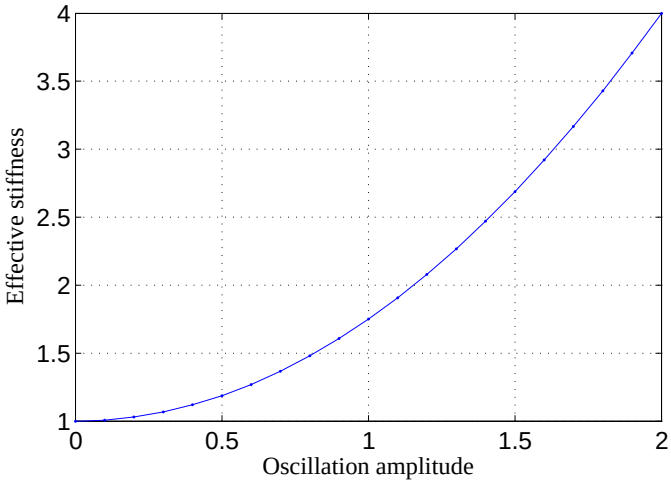

FIGURE 3.12: Effective stiffness of cubic spring

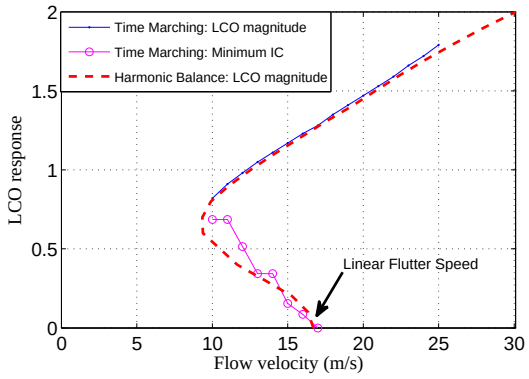

FIGURE 3.13: LCO magnitudes from HB and time march

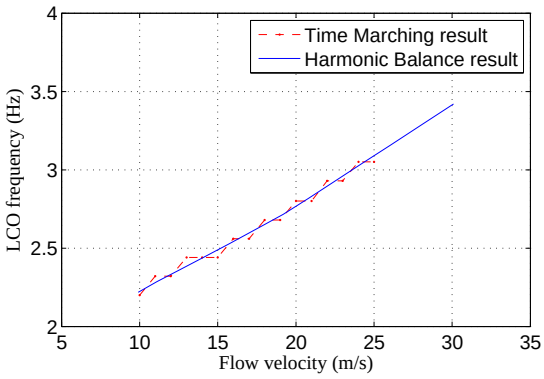

FIGURE 3.14: LCO frequencies from HB and time march

was reduced from a very high value to zero, the first frequency fell from the (root stiffness-dependent) B1T1 value and asymptoted to the (GJ-dependent) first classical clamped-free mode value; the second frequency went from the (GJ-dependent) first classical free-free mode value to 1.85 times the B1T1 value. When the closed form equations for a uniform rod with a root spring were solved, a factor of $\sqrt{3}$ was obtained (see Appendix A). The 1.85 in the B1T1 case, rather than $\sqrt{3}$, was attributed to bending-torsion coupling and lack of spanwise uniformity due to presence

of the store.

The lowest flutter velocity, caused by interaction of the first torsion mode with the bending mode, is plotted as a function of GJ in Fig. 3.16. The curves terminated abruptly because this was hump mode flutter similar to Fig. 3.1 and the V-g curves were entirely stable for sufficiently low GJ ($< 30\ Nm^2/rad$ for nominal k_1; $< 2\ Nm^2/rad$ for higher k_1).

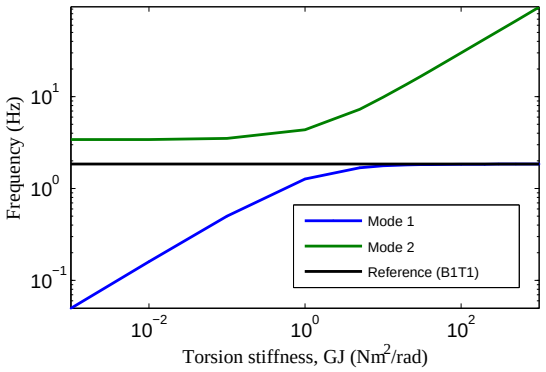

FIGURE 3.15: B1T2 torsion frequency variation at nominal k_1

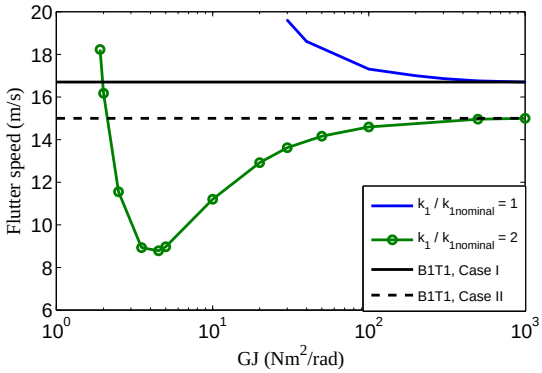

FIGURE 3.16: Effect of GJ on B1T2 flutter speed

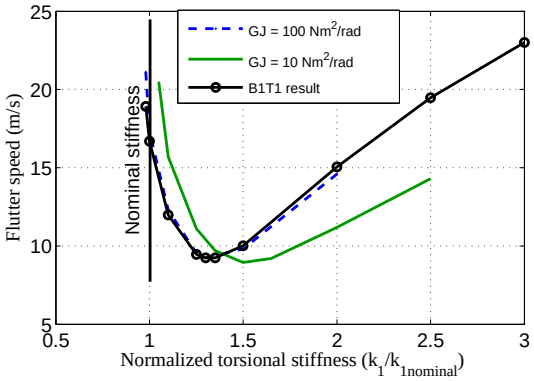

FIGURE 3.17: Flutter boundaries for various fixed torsion stiffness, GJ

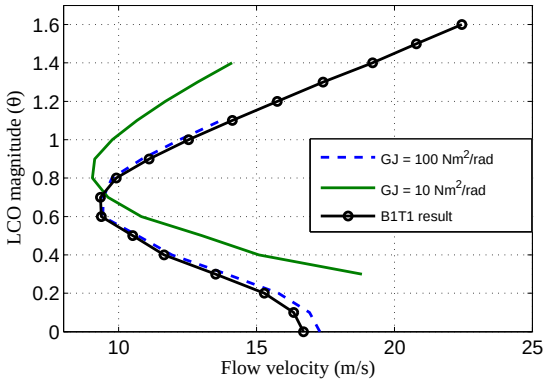

FIGURE 3.18: LCO responses for various GJ

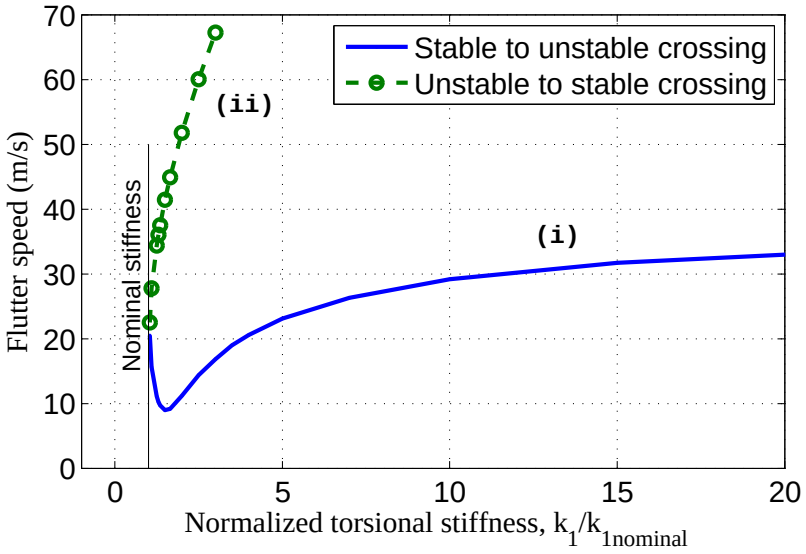

FIGURE 3.19: Extended flutter boundary, $GJ = 10Nm^2/rad$

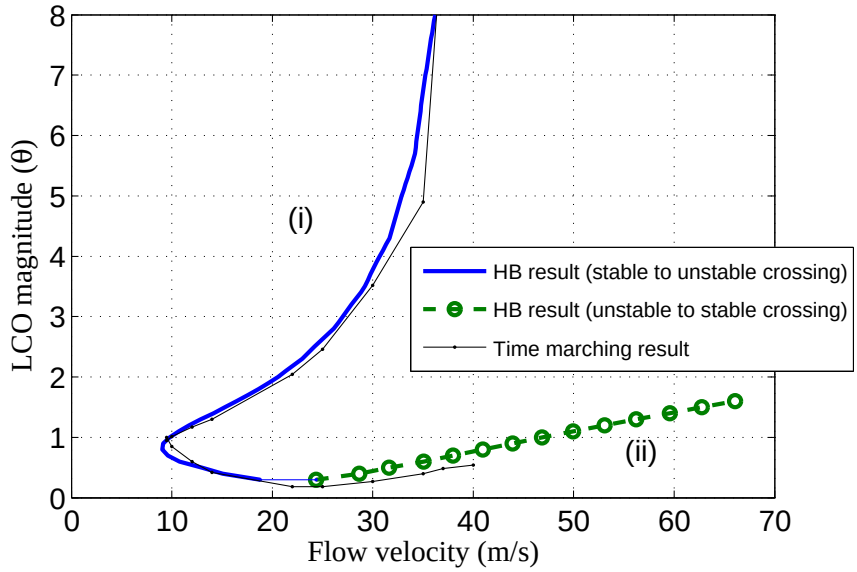

FIGURE 3.20: Extended LCO response, $GJ = 10Nm^2/rad$

Next, flutter boundaries versus k_1 were generated independently for two fixed values of GJ (Fig. 3.17) and used to calculate the LCO response (Fig. 3.18). The results for $GJ = 100\ Nm^2/rad$ were close to the B1T1 results. On the other hand for $GJ = 10\ Nm^2/rad$, the nominal linear system did not flutter because of the hump mode behavior discussed above. The unstable branch of the LCO curve obtained via HB appeared to terminate at about 20 m/s without going to zero magnitude.However, when the critical velocities related to the V-g curves crossing back from unstable to stable were also considered, the flutter boundary and consequently the LCO response curve got extended. (In Figs. 3.19,3.20 the primary and 'returning' branches are labeled (i) and (ii) respectively.) Thus the unstable LCO existed beyond 20 m/s, with a gradually increasing magnitude. In time marching simulations, the zero state was found to be locally stable beyond 20 m/s (and up to 38 m/s), with non-zero α_0 required to enter into LCO. Thus the absence of nominal linear flutter did not wholly preclude LCO, instead it created a minimum initial condition for LCO to occur. This was consistent with the Hartman-Grobman theorem, a formal statement regarding linearization of nonlinear systems [29].

Beyond 38 m/s, there was a marked change in the character of the time marching responses which included pure static response, combined static and harmonic response, and broadband response. These did not correlate with the HB results obtained so far, but were found to be related to linear system static divergence, wherein a real eigenvalue moved to the right half plane at 38.5 m/s.[4] The effective static stiffness to be considered (Eqn.3.4) differed from the effective dynamic one (Eqn. 3.3), due to the fact that the higher harmonic got combined with the first harmonic when ω was set to zero in Eqn.3.2.

$$k_{eff-static} = k_1 + k_3\alpha^2_{static} \tag{3.4}$$

[4] Linear static divergence tendency leads to 'static LCO' just as linear flutter tendency leads to dynamic LCO. For this situation in the 2D airfoil case, see [22].

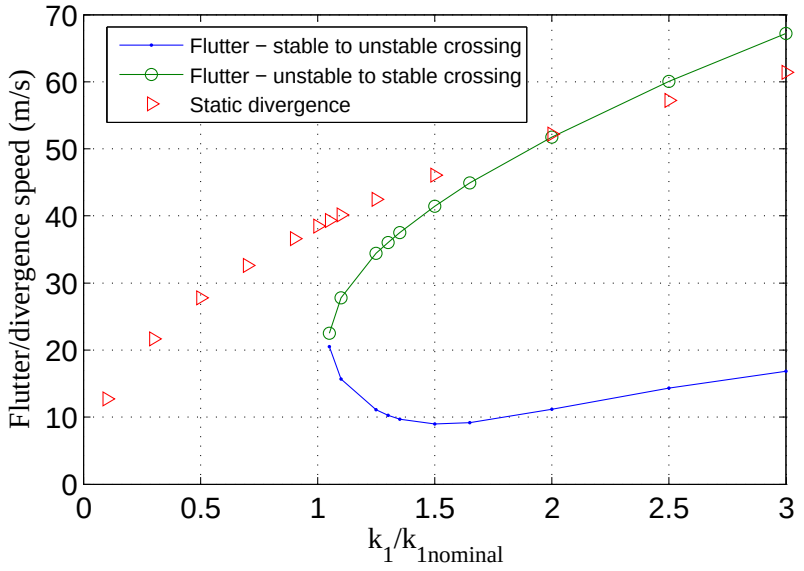

FIGURE 3.21: Flutter and divergence boundaries, $GJ = 10Nm^2/rad$

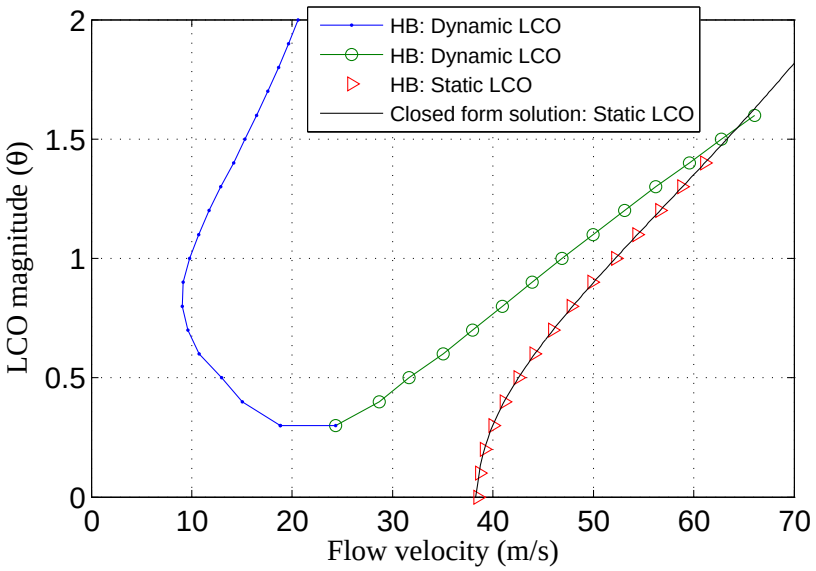

FIGURE 3.22: Static and dynamic LCO magnitudes

Figures 3.21, 3.22 show the static divergence boundary and corresponding static LCO response obtained via HB for $GJ = 10Nm^2/rad$ and nominal k_1. The LCO magnitudes were confirmed by time marching and also by solving the nonlinear static B1T2 equations in closed form (see Appendix B). Linear stability analysis of the static LCO solution showed that it turned unstable beyond 41.2 m/s, a fact that was not immediately obvious from the HB result. However, it was recognized that beyond the static LCO starting velocity of 38 m/s, the effective stiffness was determined by the combined static and dynamic response as given in Eqn. 3.5.[5]

$$k_{eff} = k_1 + k_3(\frac{3}{4}\bar{\alpha}^2 + 3\alpha_{static}^2) \tag{3.5}$$

When this expression was used in the HB method, the resulting LCO response (Fig. 3.23) differed significantly from the earlier construct in Fig. 3.20. When plotted in a conventional bifurcation diagram format by superimposing the static and dynamic response components (Fig. 3.24), it was seen that the primary bifurcation was a supercritical pitchfork, the minimum initial condition arose from a subcritical Hopf and the stable LCO was made possible by a supercritical saddle-node. The bifurcation points and LCO magnitudes predicted by HB agreed with the time marching results. (In Fig. 3.24, the HB results are shown as solid and broken lines for stable and unstable LCO branches respectively; the time marching results are shown as 'o' and '*' for stable response and initial condition threshold respectively.)

As is common in engineering practice, the aeroelastic model here was linearized about the origin. It thus appeared that a mere tendency toward flutter in the linear system (without flutter being actually present) was sufficient to cause LCO in the nonlinear system. However, if the system had been linearized about the static LCO instead of about zero, it would have exhibited flutter.

[5] For the derivation of this expression, see Eqn. 4.1.

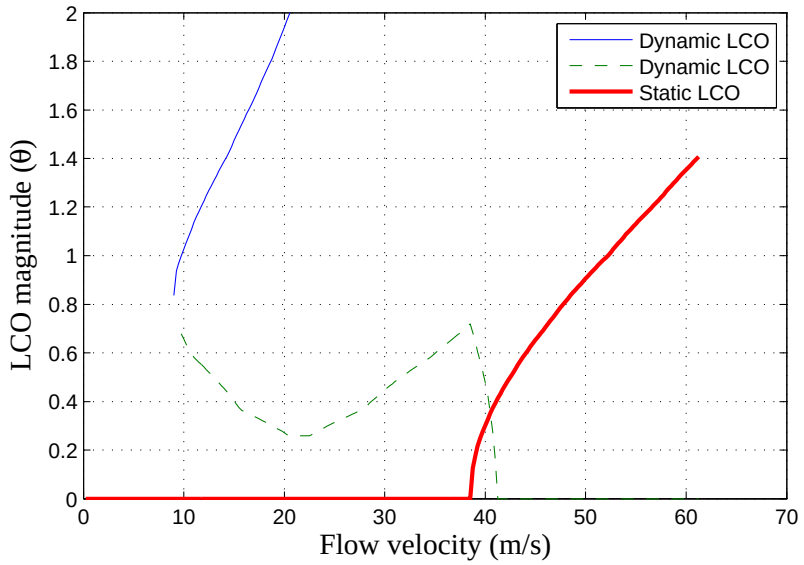

FIGURE 3.23: Corrected LCO response, $GJ = 10Nm^2/rad$

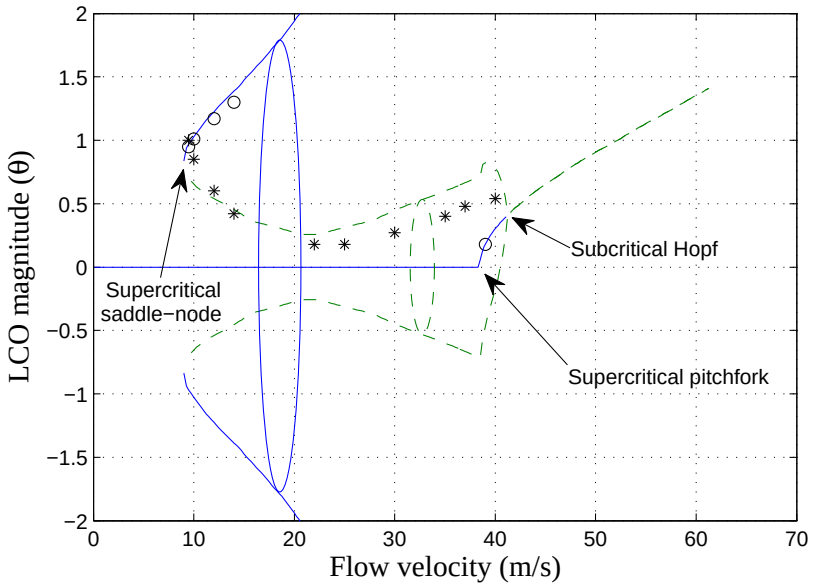

FIGURE 3.24: Bifurcation diagram, $GJ = 10Nm^2/rad$

At high $k_1 \approx 200$, the LFS asymptoted to about 40 m/s, and this was reflected in the LCO magnitude shooting up at that velocity (Fig. 3.20). Thus the nonlinearity served only to delay the flutter to a higher velocity (equal to the flutter velocity for a clamped wing) without reducing it wholly to a finite magnitude LCO. This feature was not seen in the B1T1 model, and is probably more characteristic of a fixed wing than an all-moving surface.

3.2.2 Further Explorations

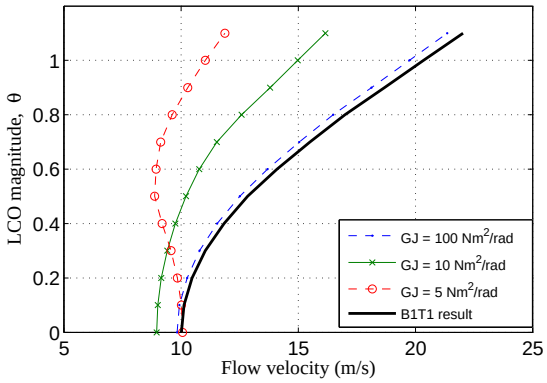

FIGURE 3.25: Effect of GJ on LCO magnitude, $k_1/k_{1nominal} = 1.5$

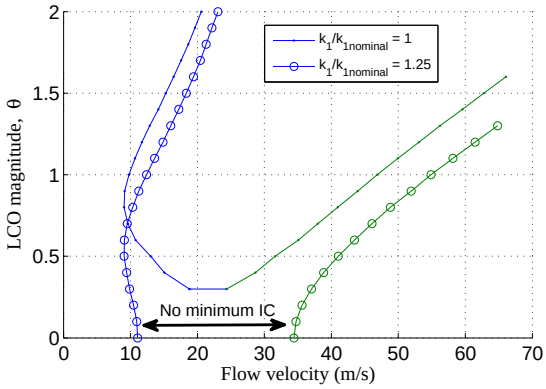

FIGURE 3.26: Atypical LCO in a limited flow velocity range

Other interesting features were observed as the B1T2 model was explored further by varying its parameters, and these are discussed below.

The presence or absence of LCO hysteresis was seen to depend on GJ when k_1 was held fixed (Fig. 3.25). Note that each plotted curve goes to zero amplitude at the LFS for that case.

When $k_1/k_{1nominal}$ was increased to 1.25, an 'atypical' LCO was obtained (Fig. 3.26). It was named so on account of some similarities to the 'nontypical' LCO exhibited by the F-16 [2] - the zero state was unstable over a bounded range of flow velocities and locally stable outside of that range.

If the cubic stiffness was made softening ($k_3 < 0$) instead of hardening, a nontypical LCO was obtained (Fig. 3.27). The meeting of the primary and returning flutter curves at low k_1 in Fig. 3.21 caused the LCO to be bounded in magnitude as well as flow velocity range. Additionally, the static divergence boundary led to an unstable static LCO of higher magnitude. Time marching responses for $\theta_0 = 0.01$ matched the dynamic LCO curve, and diverged beyond 45 m/s.

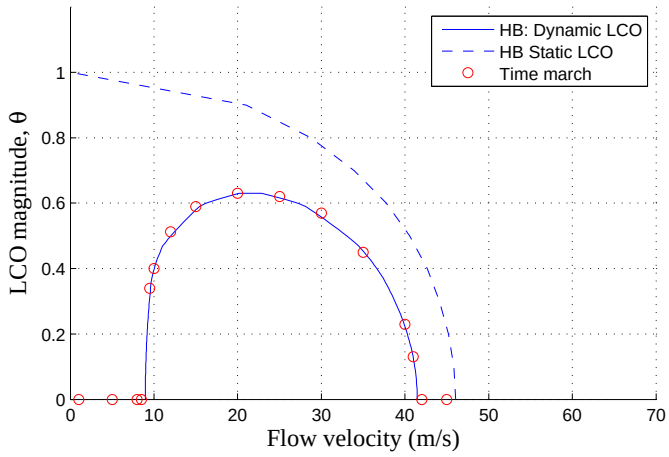

FIGURE 3.27: LCO response to due to softening cubic stiffness, $k_1/k_{1nominal} = 1.5$

The flutter boundary with versus damping is shown in Fig. 3.28 for $k_1/k_{1nominal}$ of 1.1. The primary and returning flutter velocity curves met at high c_1, hence a positive cubic damping with $c_1/c_{1nominal} = 0.1$ led to the nontypical LCO shown in Fig. 3.29. Time marching responses for $\theta_0 = 0.01$ matched the HB curve, and diverged beyond the static divergence velocity of 40 m/s.

In summary, nonlinear aeroelastic behavior obtained for the simple wing included (i) presence of unstable LCO / hysteresis due to positive cubic stiffness, depending on the ordering of bending and torsion frequencies and on GJ, (ii) delayed catastrophic flutter in the nonlinear system, due to LCO turning into flutter at a higher (but finite) flow velocity as compared to the linear system, (iii) linear flutter tendency but

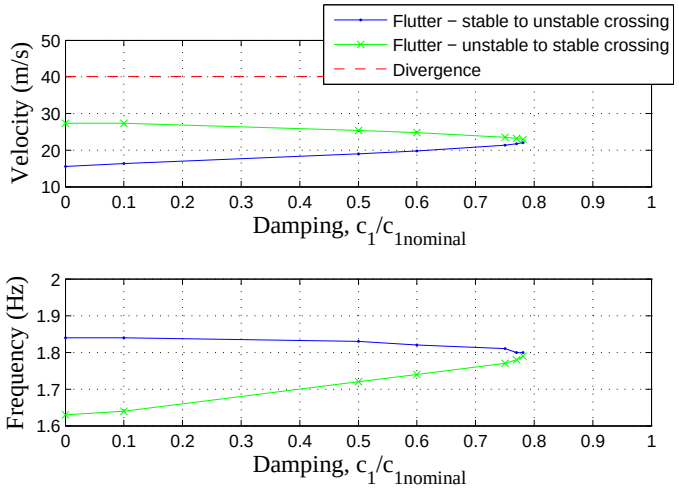

FIGURE 3.28: Flutter boundary vs damping, $k_1/k_{1nominal} = 1.1$

without actual flutter (due to a hump in the flutter damping curve) manifesting as a minimum initial condition for entry into LCO, (iv) nonlinear static LCO related to linear system static divergence, (v) atypical LCO, with the zero state being unstable over a finite flow velocity range and locally stable outside of it, and (vi) nontypical LCO due to cubic stiffness/damping existing over a finite flow velocity range. It

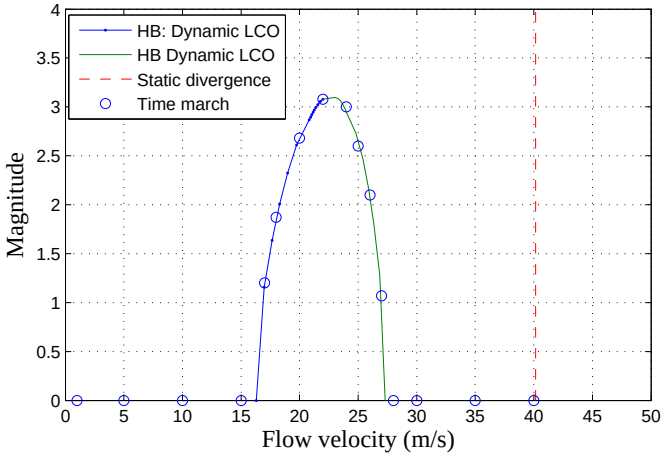

FIGURE 3.29: LCO response to due to positive cubic damping, $k_1/k_{1nominal} = 1.1$

was found possible to construct the bifurcation diagram of the nonlinear system by applying the HB method to the flutter and divergence boundaries of the model linearized about the origin.

3.3 Applicability to Larger Models

Table 3.2: BxTy mode convergence study ($k_1/k_{1nominal} = 1$)

# of bending modes	# of torsion modes	Flutter speed (m/s): $GJ = 100Nm^2/rad$	Divergence speed (m/s): $GJ = 10Nm^2/rad$
1	1	16.7	40.1
1	2	17.3	38.5
1	3	17.5	38.1
1	4	17.6	38
1	5	17.7	37.9
1	6	17.7	37.8
2	1	16.2	40.1
2	2	16.8	38.5
3	1	16.2	40.1
3	2	16.7	38.5
3	3	16.9	38.1
4	2	16.7	38.5
4	4	17	38
5	5	17	37.9

Until now, the discussion pertained to a simple wing model with a small (indeed minimal) set of structural modes and approximate (quasisteady, strip) aerodynamics. Therefore the question naturally arose as to their applicability to larger and more realistic systems, and was addressed by (1) adding more modes to the model and (2) replacing the aerodynamic model with VLM. As the model size was increased, the flutter and divergence velocities varied marginally (Table 3.2), and the flutter boundary for B5T5 was essentially the same as that for B1T2 (Fig. 3.30). The results

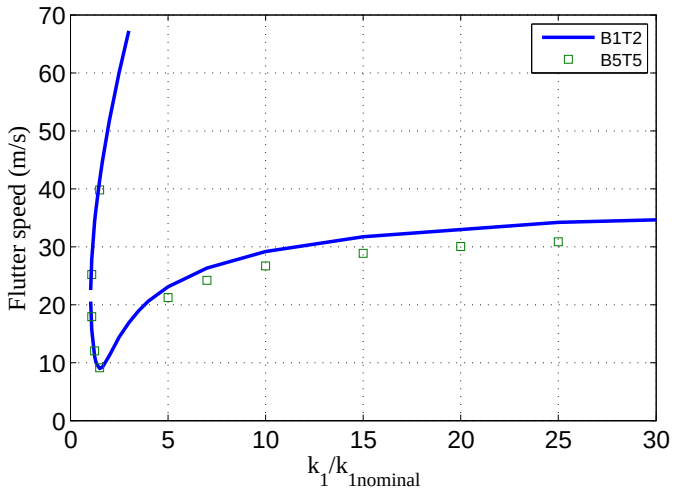

FIGURE 3.30: Effect of model size on flutter boundary

with VLM aerodynamics were qualitatively similar to the earlier results, as can be seen by comparing Fig. 3.31 with Figs. 3.11, 3.13. Therefore the above analysis approach and results were felt to have broad applicability beyond the simple wing that had been examined.

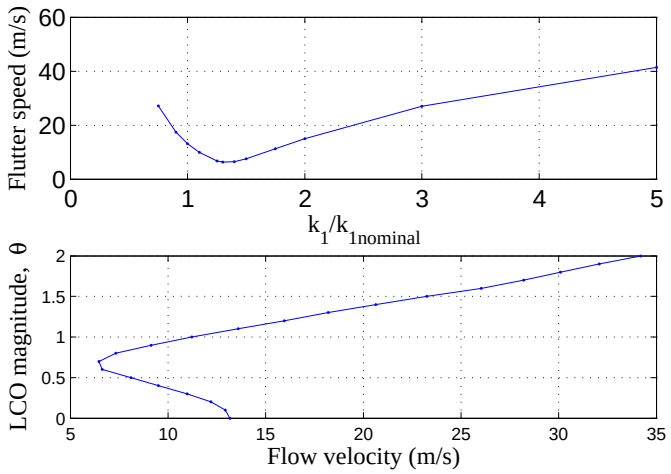

FIGURE 3.31: Flutter and LCO with VLM aerodynamics

4

Generic Wing Results

This chapter documents how the presence of a localized nonlinearity in the wing-store attachment of an aircraft wing can influence its aeroelastic behavior. The wing was clamped at the root and the nonlinearity was introduced in store pitch, α_s. VLM aerodynamics was assumed for the wing and the store aerodynamics was neglected. Structural dynamic and linear aeroelastic characteristics of the system were determined using eigenanalysis. Various nonlinear mechanisms (cubic restoring force, freeplay and Coulomb friction) were examined using Harmonic Balance and time marching, and the results were correlated to the system linear properties.

4.1 Structural Dynamics and Flutter

The structural model was constructed using five primitive modes namely (i) uniform beam 1^{st} bending, (ii) uniform rod 1^{st} torsion, (iii) uniform rod 2^{nd} torsion, (iv) store plunge relative to wing and (v) store pitch relative to wing. The resulting eigenmodes are shown in Fig. 4.1, where the h_s and α_s values have been normalized by the h and α at wing tip respectively.

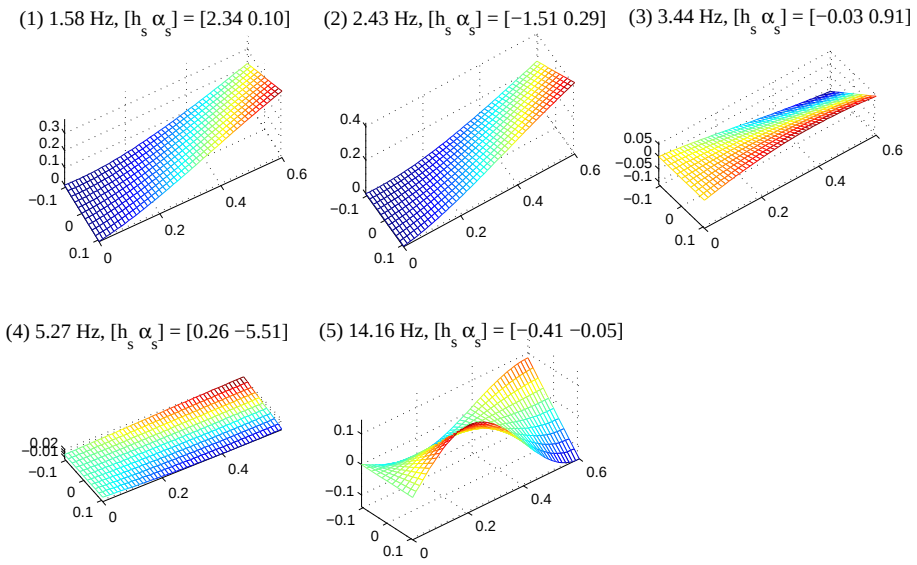

FIGURE 4.1: Generic wing eigenmodes

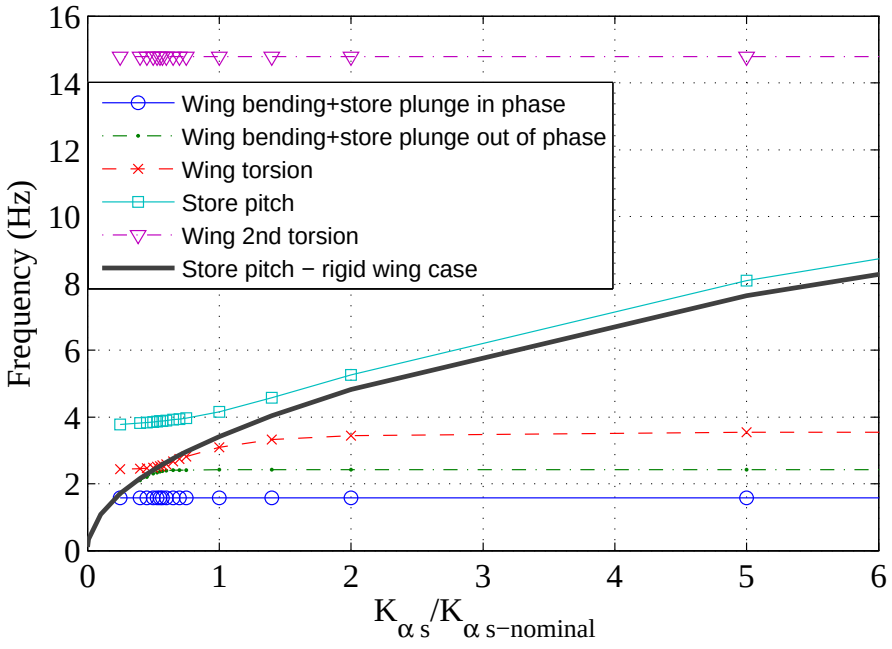

FIGURE 4.2: Natural frequencies as a function of K_{α_s}

In-vacuo natural frequencies were mapped as a function of the store pitch stiffness, K_{α_s} (normalized by $K_{\alpha_s - nominal}$) as shown in Fig. 4.2. The accompanying mode descriptions are for very high K_{α_s}. As K_{α_s} was reduced from a high value, initially the store pitch frequency (Mode 4) fell while the others were largely unchanged. Subsequently the other modes were also affected and the dominant α_s content moved gradually to Mode 3 and to Mode 2 as K_{α_s} was reduced to 2 and 0.5 respectively. At the same time, wing torsion content moved from Mode 3 to Mode 4 and wing bending content moved from Mode 2 to Mode 3. The α_s content of Mode 3 peaked for $K_{\alpha_s} = 0.55$, when its frequency was very close to that of Mode 2.

The VLM grid points were equi-spaced. There were 4 aerodynamic panels along the chord, 20 panels along the wake and 10 panels along the span. The circulations of these 240 panels constituted the aerodynamic states. When combined with the 10 structural states coming from the 5 modes, the aeroelastic model size became 250.

Linear flutter velocity and frequency were computed for various K_{α_s} with K_{h_s} fixed at a nominal value and the store mode damping levels, ζ_{α_s} and ζ_{h_s} fixed at 2%. The resulting flutter boundary is shown in Fig. 4.3. The ends of the velocity curve corresponded to store free-in-pitch and fixed-in-pitch cases respectively. The dip at $K_{\alpha_s} \approx 0.62$ was close to where the in-vacuo $|\Delta f|$ of the interacting modes reached a minimum - also true for the simple wing (see Fig. 3.11). When the store pitch frequency, f_{α_s} passed the wing mode frequencies, a sharp peak was seen due to a switch in the flutter-interacting modes from (2, 3) to (3, 4). Mode 1 was primarily a store plunge mode that did not participate in flutter. In the transition region, wing bending (Mode 2), wing torsion (Mode 3) and store pitch (Mode 4) interacted to cause flutter (see Fig. 4.4).

The linear flutter boundary was also computed as a function of ζ_{α_s} with all other parameters fixed (Fig. 4.5). The flutter velocity increased monotonically with ζ_{α_s} but the variation was over a relatively small range as compared to the K_{α_s} case.

Note that very high ζ_{α_s} had the same effect as very high K_{α_s}, resulting in a rigid (in pitch) wing-store attachment and a flutter velocity around 30 m/s.

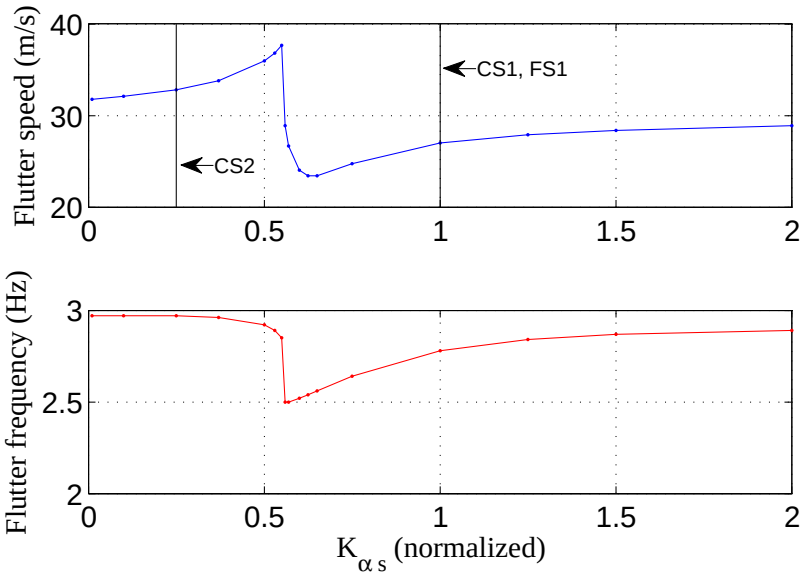

FIGURE 4.3: Flutter boundary vs stiffness

4.2 LCO due to Nonlinear Stiffness

LCO responses were calculated via HB for cubic stiffness and freeplay stiffness using the flutter boundary of Fig. 4.3. For the cubic stiffness case, time marching with nonzero initial store pitch, α_{s0} was also done. All responses were scaled as per Table 2.2 and plotted using solid lines for stable branches and broken lines for unstable ones, along with a vertical marker to indicate the LFS of the linearized system.

4.2.1 Cubic Stiffness

Two cases with linear stiffness, K_{α_s} of 1 and 0.25, from either side of the transition region in Fig. 4.3 were considered. These cases were labeled CS1 and CS2, and their LCO responses are shown in Fig. 4.6, 4.8 respectively.

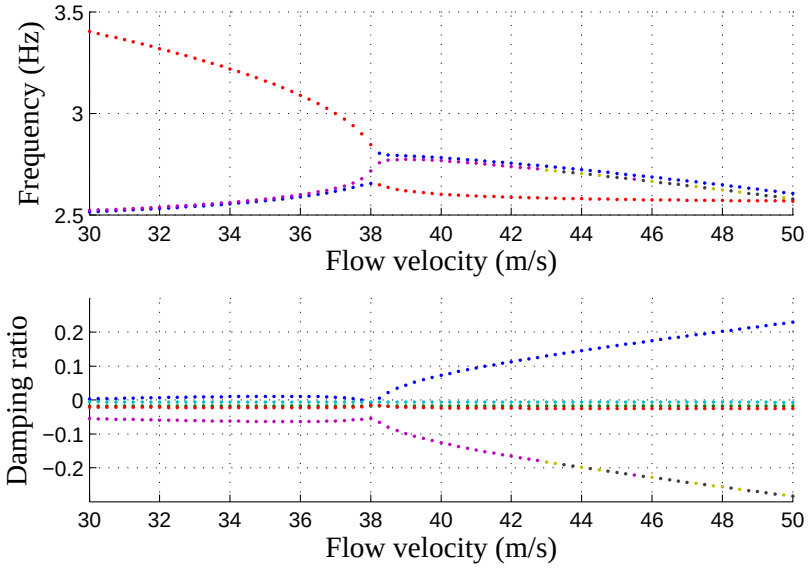

FIGURE 4.4: Interaction of three modes leading to flutter

The CS1 response was stable and supercritical, i.e. wholly above the LFS. Stability was determined by considering a point on the *flutter velocity* curve corresponding to a specific k_{eff}. An increase in LCO amplitude implied an increase in k_{eff} and the point moved to the right into the stable region, so the response would decay back to the LCO. By a similar argument, a decrease in amplitude would be followed by the response growing back to the LCO. Hence the LCO was stable. A sample LCO time history at 27.5 m/s is provided in Fig. 4.7.

The CS2 response contained stable sub- and supercritical branches, with an unstable branch connecting them. The subcritical LCO turned into catastrophic flutter at 30 m/s, which was the LFS for a rigid (in pitch) wing-store attachment. The stable branches were matched by time marching, except at large magnitudes and near the turning points where two branches met. The unstable branch was close to the minimum α_{s0} required to enter into LCO. Next, the vicinity of the turning points was studied more closely and the following observations were made.

Above 33.5 m/s, diverging oscillations occurred for any small disturbance. Such

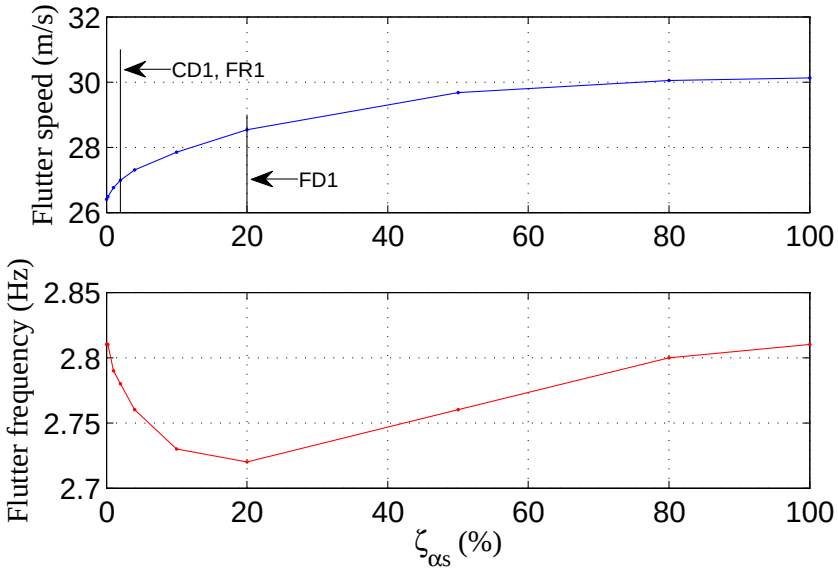

FIGURE 4.5: Flutter boundary vs $\zeta_{\alpha_s}(\%)$

disagreement between time marching and HB with one harmonic is natural near an intersection of distinct LCO branches. Additionally, the HB-derived LCO magnitudes in this flow velocity range were such that $\theta_{unstableLCO} < 2\theta_{stableLCO}$. Presumably this was not a coincidence - the same relationship existed when the wing-store attachment damping, ζ_{α_s} was increased to about 20%. To understand this better, the stable LCO at 33.5 m/s was perturbed slightly. The perturbation response showed oscillatory decay, indicating that the LCO was an underdamped attractor (Fig. 4.9).[1] At flow velocities above 33.5 m/s, a small initial disturbance from the zero state appeared to function as a large perturbation from the stable LCO, thereby making the system response overshoot the potential energy barrier represented by the unstable LCO and diverge thereafter. Such an interpretation allows an accurate LCO cutoff velocity for safe aircraft operation to be deduced from the HB result itself without resorting to time marching.

[1] In contrast, the resonant response of a linear system can be shown to be a critically damped attractor.

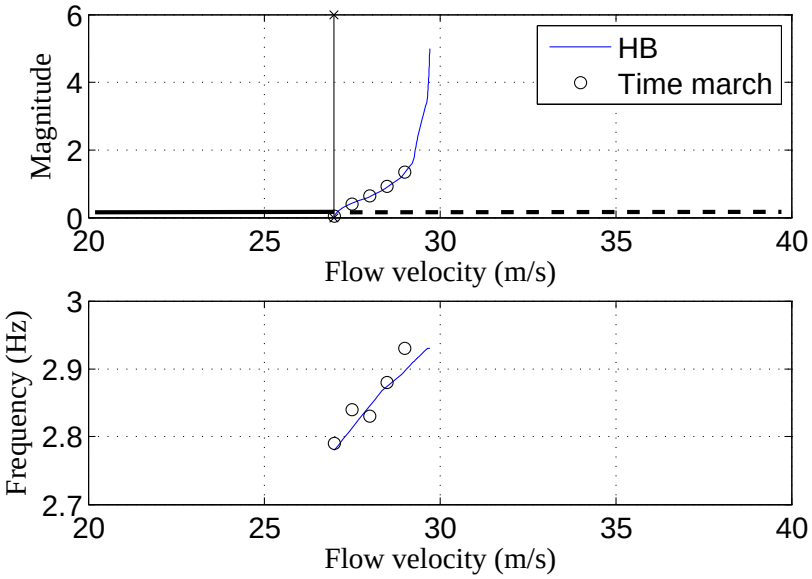

FIGURE 4.6: LCO response due to cubic stiffness, case CS1

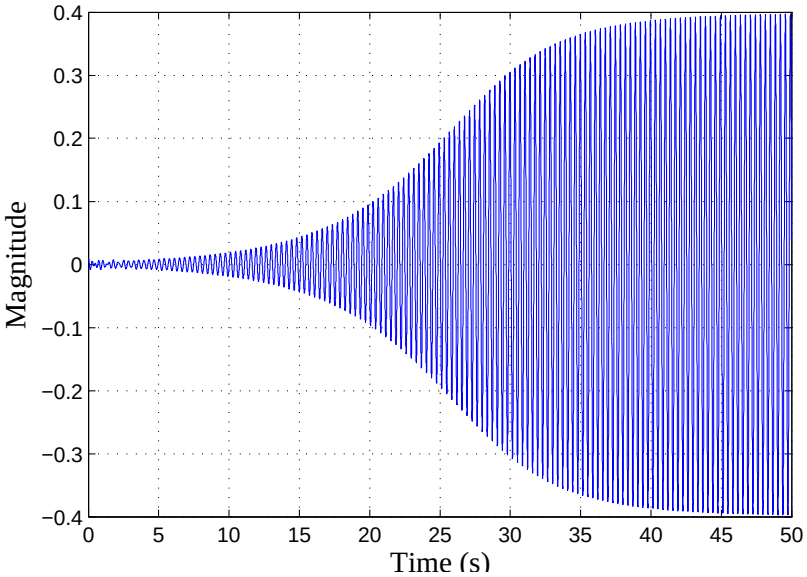

FIGURE 4.7: LCO time history at 27.5 m/s, case CS1

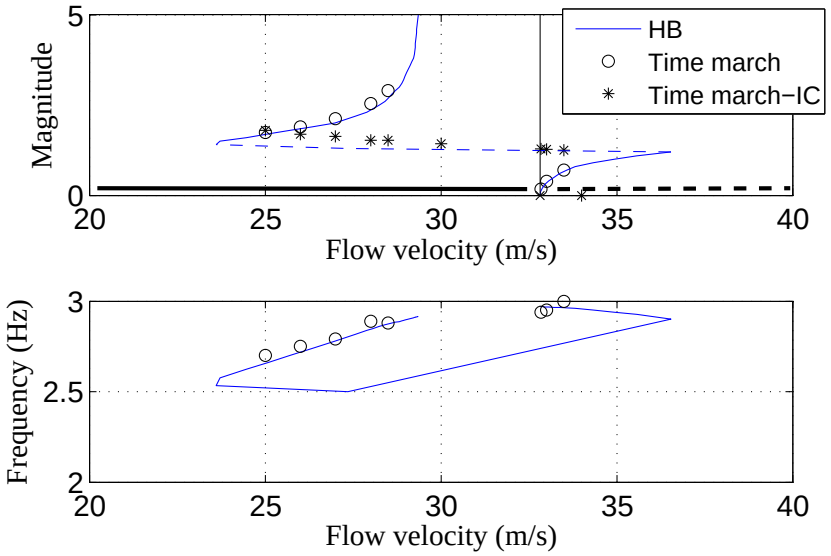

FIGURE 4.8: LCO response due to cubic stiffness, case CS2

A series of initial conditions, α_{s0} were fed in the flow velocity range 25-27 m/s. Three different outcomes are shown in Fig. 4.10, namely decay to zero (▫), entry into LCO (▵), and oscillatory divergence (◇). Basins of attraction for these outcomes can be seen clearly for 27 m/s, along with some interleaving at higher α_{s0}. The divergence at still higher α_{s0} may indicate that as the LCO curve approaches higher magnitudes, it actually turns to the left to create an unstable branch. It should be possible to confirm this using HB with higher harmonics taken into account.

4.2.2 Freeplay Stiffness

LCO response due to freeplay stiffness (case FS1) with K_{α_s} of 1 was both sub- and supercritical. In Fig. 4.11, there are two stable branches connected by an unstable branch, and the vertical branch at 31.8 m/s represents neutrally stable oscillations within the freeplay gap.

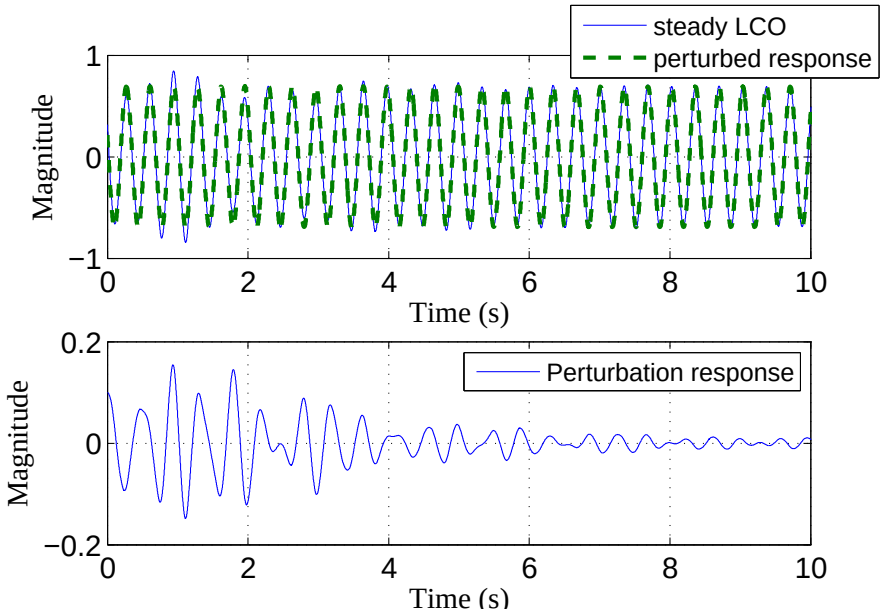

FIGURE 4.9: Perturbation of LCO at 33.5 m/s, case CS2

4.3 LCO due to Nonlinear Damping

LCO responses were calculated via HB for cubic damping, freeplay damping and friction using the flutter boundary of Fig 4.5. For the cubic damping case, time marching with nonzero α_{s0} was also done. All responses were scaled as per Table 2.2 and plotted using solid lines for stable branches and broken lines for unstable ones, along with a vertical marker to indicate the LFS of the linearized system.

4.3.1 Cubic Damping

LCO response due to cubic damping for case CD1 (nominal $\zeta_{\alpha_s} = 2\%$) is presented in Fig. 4.12, along with confirmatory time marching results. This was a supercritical stable LCO, similar to the cubic stiffness case CS1.

4.3.2 Freeplay Damping

Figure 4.13 shows LCO response due to freeplay damping for case FD1 with nominal $\zeta_{\alpha_s} = 20\%$. This was a stable subcritical LCO, unlike the freeplay stiffness case FS1.

The relatively high damping level was chosen as otherwise the LCO was restricted to an extremely narrow flow velocity range. Thus the freeplay damping effect appeared to be insignificant when compared to the freeplay stiffness effect, and this was confirmed by comparing the flutter boundaries for stiffness-alone variation and for stiffness-and-damping variation (Fig. 4.14).

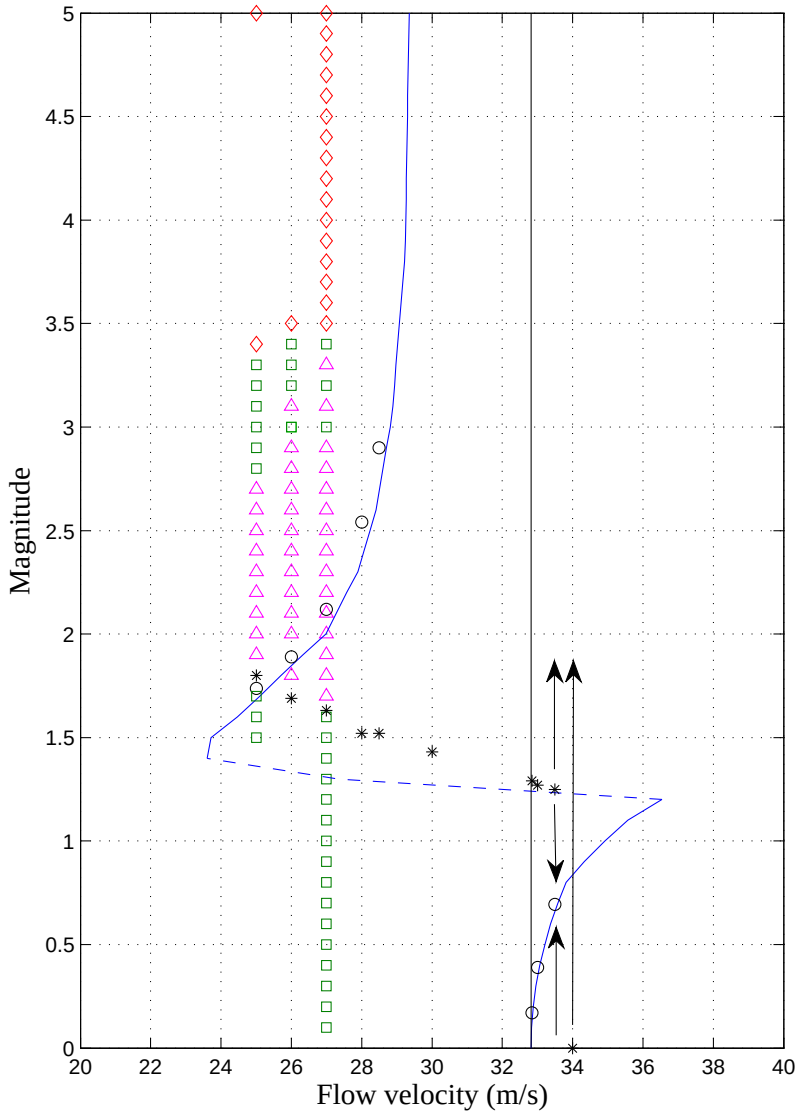

FIGURE 4.10: Effect of initial conditions on LCO, case CS2
(▫ = decay to zero, ▵ = entry into LCO, ◇ = oscillatory divergence)

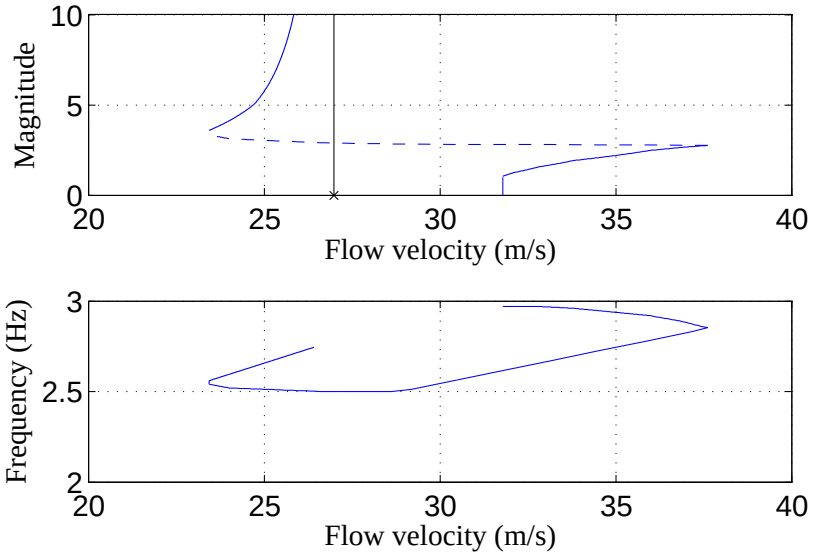

FIGURE 4.11: LCO response due to freeplay stiffness, case FS1

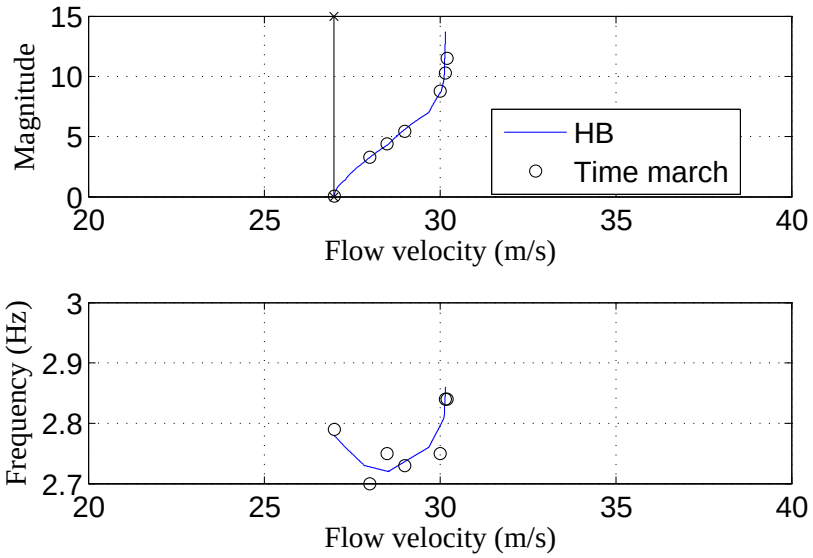

FIGURE 4.12: LCO response due to cubic damping, case CD1

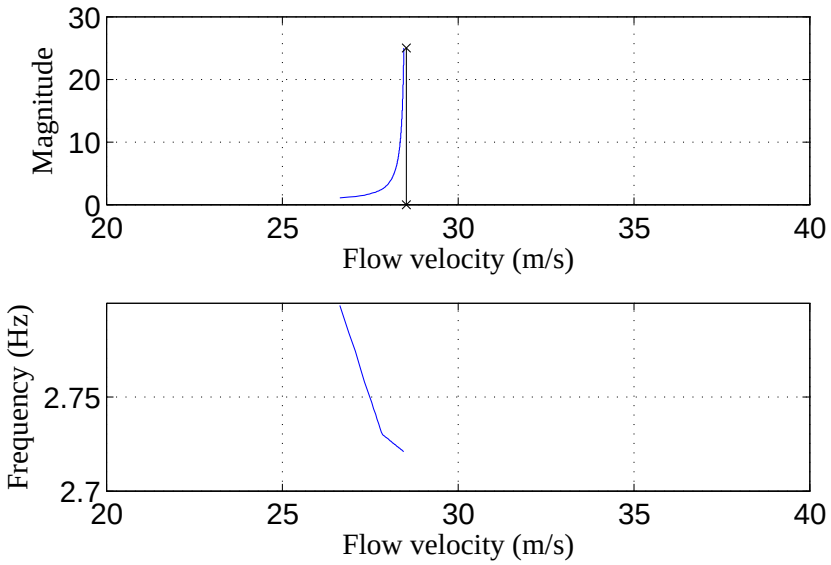

FIGURE 4.13: LCO response due to freeplay damping, case FD1

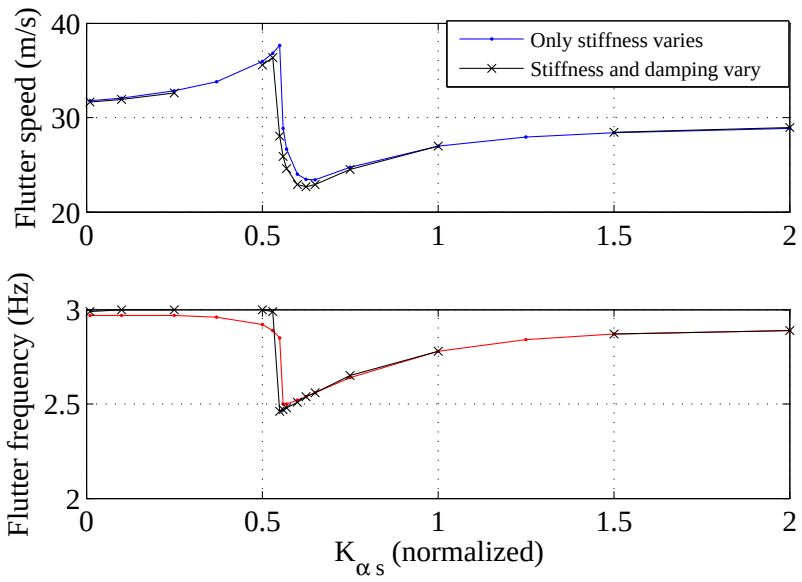

FIGURE 4.14: Flutter boundary vs stiffness and damping

4.3.3 Friction Damping

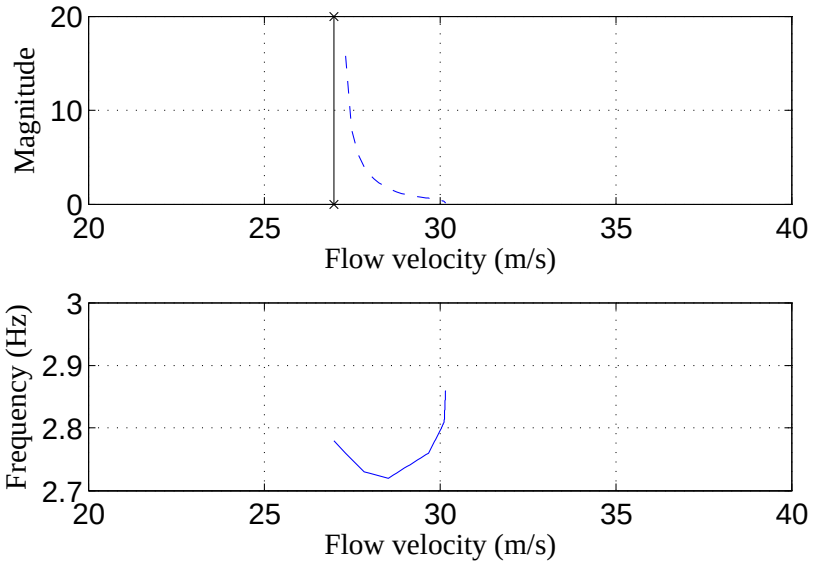

FIGURE 4.15: LCO response due to friction damping, case FR1

LCO response due to friction for case FR1 (nominal $\zeta_{\alpha_s} = 2\%$) is presented in Fig. 4.15. This was a supercritical unstable LCO with a very large magnitude near the LFS and tending to zero at 30 m/s. The implications were (i) the zero displacement state would be stable up to the LFS, conditionally stable upto the flutter velocity for a rigid (in pitch) wing-store attachment, and unstable at still higher velocities and (ii) the minimum initial disturbance that would lead to catastrophic oscillations was related to the unstable LCO magnitude. Since the assumption of perfect slip and no stick breaks down at low oscillation amplitudes, predictions at higher velocities were expected to be relatively less accurate.[2]

[2] Sticking is most prominent at the extremities of travel e.g., Fig. 7 of [30], which suggests a cutoff amplitude of F_d/k_1.

4.4 Summary of LCO Response Trends

The generic wing exhibited features that are often seen in real stores-carrying aircraft, related to the ordering of in-vacuo frequencies ($\omega_{torsion} > \omega_{bending}$ and vice versa), flutter behavior (regular and hump mode), number of flutter-interacting modes (two and three) and LCO buildup (rapid and slow). It was possible to identify the following patterns from the results. For flow velocities approaching the LFS, the LCO magnitude tended to zero for cubic nonlinearity but became unbounded for freeplay and friction. This was due to the fact that a system with cubic restoring force tends to linearity for small oscillations whereas a system with freeplay or friction does so for large oscillations. For the 'prototypical' case of linear flutter velocity increasing *monotonically* with stiffness or damping (whichever is nonlinear), the nature of LCO can be correlated to the causative nonlinear mechanism as shown in Table 4.1.

An interesting case of stable subcritical LCO was seen when an F-16 flutter test was simulated with friction included in the wing-store attachment (see Fig. 4.16 taken from [31]). This is quite possible if there is a dip in the flutter velocity boundary with respect to damping. Figure 4.17 illustrates this by comparing cases without and with a dip; the segment to the *left* of the dip maps to a stable subcritical LCO branch.

The nonlinear mechanisms examined here have figured in prior analytical as well as experimental work, mostly in contexts other than wing-store attachments. Freeplay in control surface linkages has been well studied, with excellent agreement reported between theory, computations (HB as well as time marching) and experiments. Friction in aeroelastic systems has not received much consideration, however nonlinear shimmy analyses related to friction and freeplay in aircraft landing gears are found in [32] and they tend to support the present results.[3]

[3] Shimmy and flutter are both related to Hopf bifurcations.

Table 4.1: LCO response trends for monotonically increasing flutter boundary

Nonlinear mechanism	LCO response	Effect
Hardening cubic stiffness/damping	Supercritical, stable	Beneficial
Softening cubic stiffness/damping	Subcritical, unstable	Detrimental
Freeplay stiffness/damping	Subcritical, stable	Detrimental
Coulomb friction damping	Supercritical, unstable	Beneficial

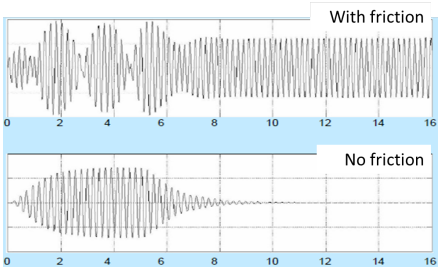

FIGURE 4.16: F-16 simulation

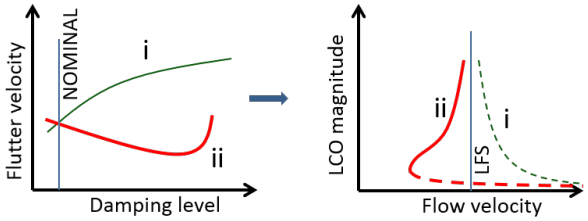

FIGURE 4.17: Friction effects

4.5 Further Explorations

4.5.1 Effect of Wing-Store Attachment Damping

The behavior of the system was studied for increased levels of damping in the wing-store attachment (uncoupled $\zeta_{\alpha_s} = 6\%$ and $\zeta_{h_s} = 24\%$, up from the earlier 2%). The flutter boundary with respect to K_{α_s} is shown in Fig. 4.18, along with the boundary for $\zeta_{\alpha_s} = 2\%$ as reference. The increased damping level had the effect of raising the flutter velocity curve and almost eliminating the dip.

Two cases of cubic stiffness with linear stiffness with K_{α_s} of 1 and 0.25, from either side of the transition region in the flutter boundary were considered. The LCO curves for these cases, labeled CS3 and CS4 respectively, are shown in Fig. 4.19, 4.20. They were broadly similar to the CS1 and CS2 cases, but were restricted to smaller velocity ranges because the dip in the flutter boundary had gone away. Time marching for the CS4 case confirmed the HB predictions upto 36 m/s, and yielded broadband, divergent responses for any small disturbance beyond this flow velocity.

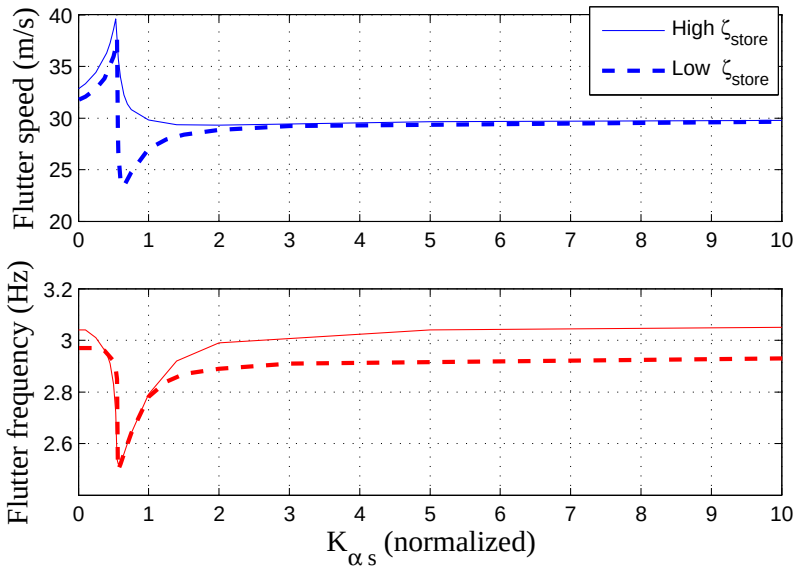

FIGURE 4.18: Flutter boundary vs stiffness

Three cases of cubic damping were studied, with K_{α_s} of 2, 0.6 and 0.25, chosen from the right, middle and left of the transition region in Fig. 4.18. Because the K_{α_s} was different in each case, the flutter boundary curves with respect to ζ_{α_s} were also different. Results for these cases labeled CD2-4 are shown in Figs. 4.21 along with some time marching comparisons. The flutter boundaries differed significantly from each other, with the CD3 and CD4 curves containing peaks instead of increasing monotonically with damping. However at very high ζ_{α_s}, they all asymptoted to the flutter velocity for a rigid (in pitch) wing-store attachment. The LCO curve for CD2 was stable, and qualitatively similar to that for CD1. The LCO curves for CD3 and CD4 had unstable branches as well; the minimum α_{s0} required to enter into LCO was about 50 times the unstable LCO magnitude, in contrast to the cubic stiffness case CS2 where it was of the same order. The reason is thought to be as follows. The unstable LCO branch comes from the 'descending' part of the flutter boundary corresponding to very high ζ_{α_s} and hence low α_s content. Therefore with all other initial states at zero, α_{s0} would need to be very high in order to enter into LCO.

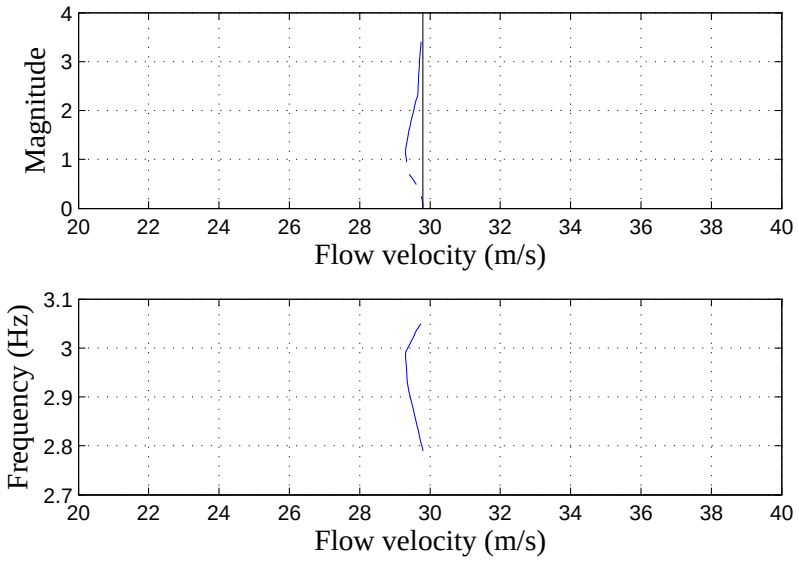

FIGURE 4.19: LCO response due to cubic stiffness, case CS3

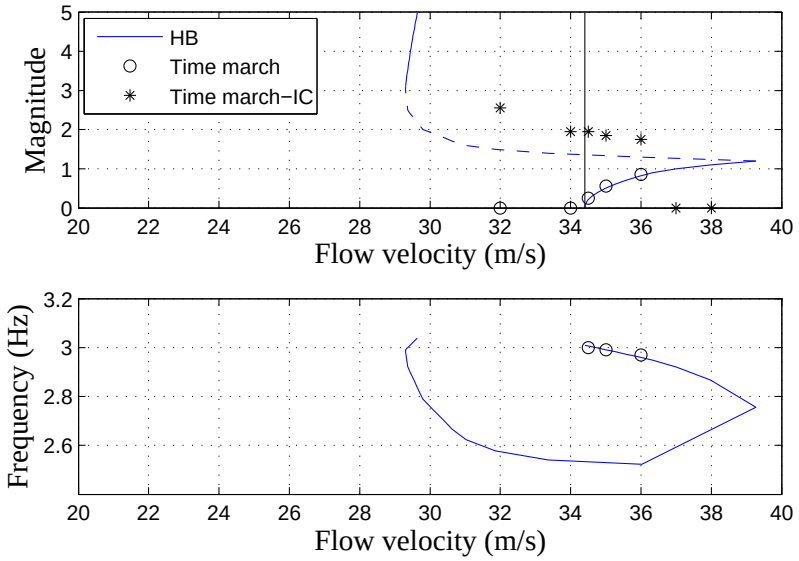

FIGURE 4.20: LCO response due to cubic stiffness, case CS4

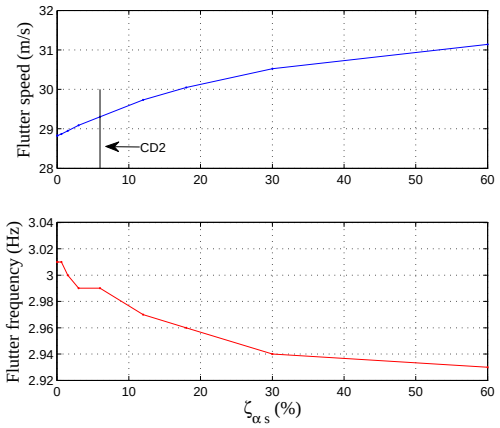

(a) Flutter, CD2

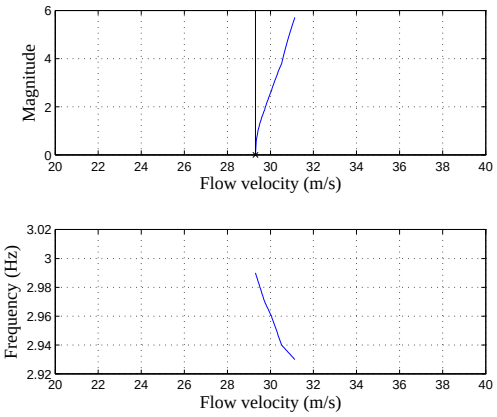

(b) LCO, CD2

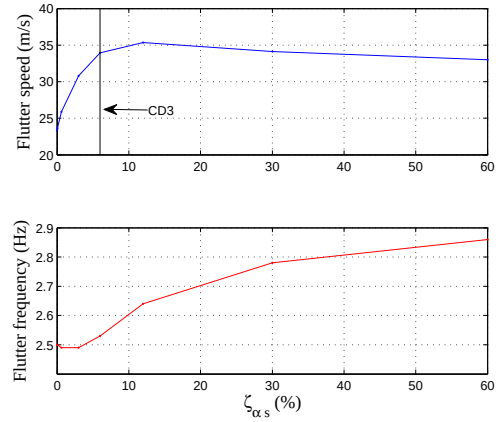

(c) Flutter, CD3

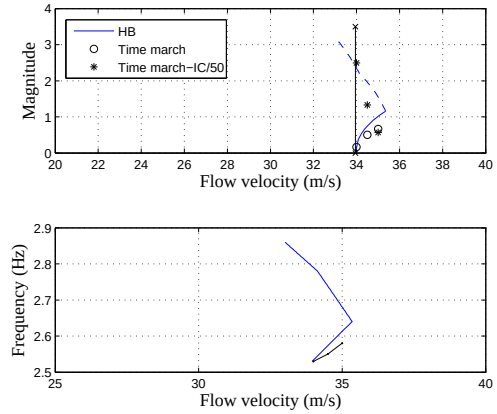

(d) LCO, CD3

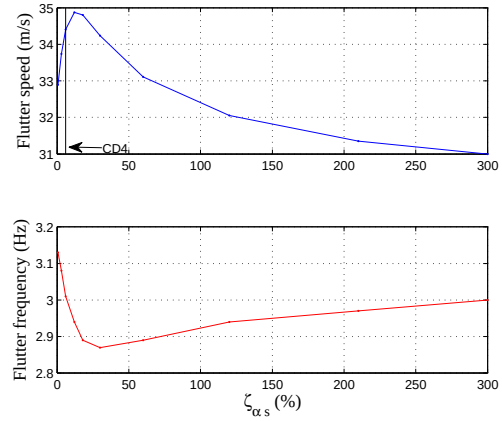

(e) Flutter, CD4

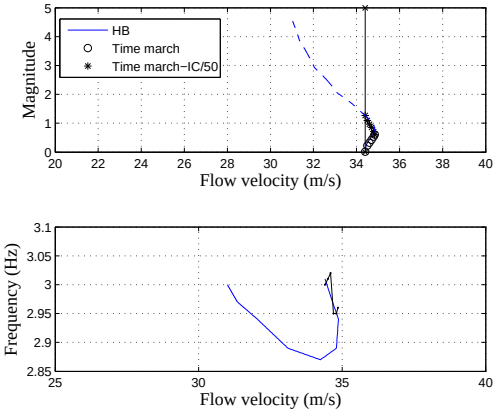

(f) LCO, CD4

FIGURE 4.21: Flutter boundaries and LCO responses due to cubic damping, cases CD2-4

4.5.2 Effect of Static Preload

Gravity and maneuver inertial loads create static loads on the store. Unlike in linear systems, the effect of this 'preload' cannot be directly added to the LCO response. An attempt was made to calculate the generic wing LCO response due to hardening cubic sitffness in the presence of a mechanical preload quantified by a static displacement, α_{pl}. When dynamic motion of the form, $\alpha_{st} + \bar{\alpha}cos(\omega t)$ was assumed, the restoring force was given by Eqn. 4.1.

$$\begin{aligned} F(t) &= k_1\alpha(t) + k_3\alpha^3(t) = k_1\big[\alpha_{st} + \bar{\alpha}cos(\omega t)\big] + k_3\big[\alpha_{st} + \bar{\alpha}cos(\omega t)\big]^3 \\ &= \left[k_1\alpha_{st} + k_3\alpha_{st}^3 + \frac{3}{2}k_3\alpha_{st}\bar{\alpha}^2\right] + \left[k_1\bar{\alpha} + k_3(\frac{3}{4}\bar{\alpha}^3 + 3\alpha_{st}^2\bar{\alpha})\right]cos(\omega t) \end{aligned} \tag{4.1}$$

The static component of F could be equated to the original preload force as shown in Eqn. 4.2. In the general case, the (mechanical) preload would be augmented by aerodynamic feedback and flow velocity would enter into the model. However that did not happen here because the store aerodynamic forces were not modeled. The static response, α_{st} in Eqn. 4.2 went from α_{pl} to zero as the LCO magnitude, $\bar{\alpha}$ grew. This was because when the oscillation was initiated about a nonzero equilibrium point, the resulting dynamic loading was unsymmetric and it acted to push the mean equilibrium point back toward zero.

$$k_1\alpha_{st} + k_3\alpha_{st}^3 + \frac{3}{2}k_3\alpha_{st}\bar{\alpha}^2 = k_1\alpha_{pl} + k_3\alpha_{pl}^3 \tag{4.2}$$

The dynamic component of F yielded the effective stiffness as a function of α_{st} and $\bar{\alpha}$ (Eqn. 4.3).

$$k_{eff} = k_1 + k_3(\frac{3}{4}\bar{\alpha}^2 + 3\alpha_{st}^2) \tag{4.3}$$

When rewritten using the relation, $\alpha = (\sqrt{k_1/k_3})\theta$, these become

$$\theta_{st} + \theta_{st}^3 + \frac{3}{2}\theta_{st}\bar{\theta}^2 = \theta_{pl} + \theta_{pl}^3 \tag{4.4}$$

and

$$k_{eff} = k_1(1 + \frac{3}{4}\bar{\theta}^2 + 3\theta_{st}^2) \tag{4.5}$$

The LCO response was calculated in three steps as follows. Choosing a series of values of $\theta_{st} < \theta_{pl}$, Eqn. 4.4 was first solved for each θ_{st} to obtain the corresponding $\bar{\theta}$. Next, the θ_{st} and $\bar{\theta}$ were used to calculate k_{eff}. Finally, the linear flutter boundary with respect to stiffness was used to obtain the flow velocity. Plotting $\bar{\theta}$ against flow velocity gave the LCO response.

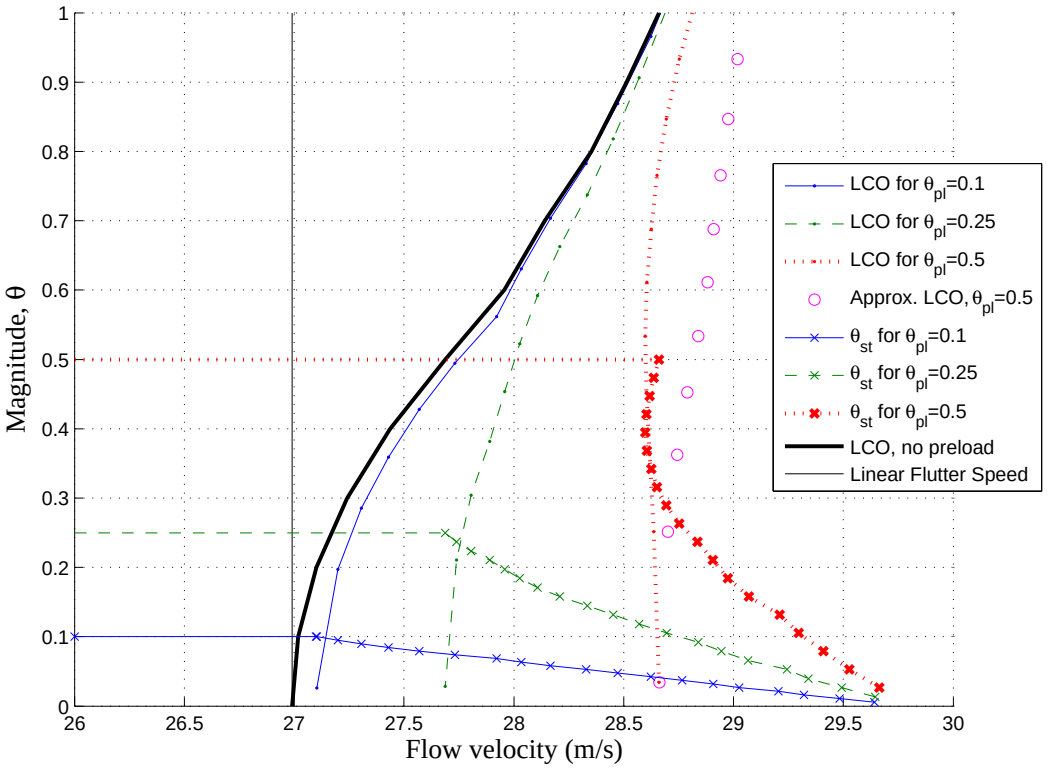

FIGURE 4.22: With-preload LCO responses from HB

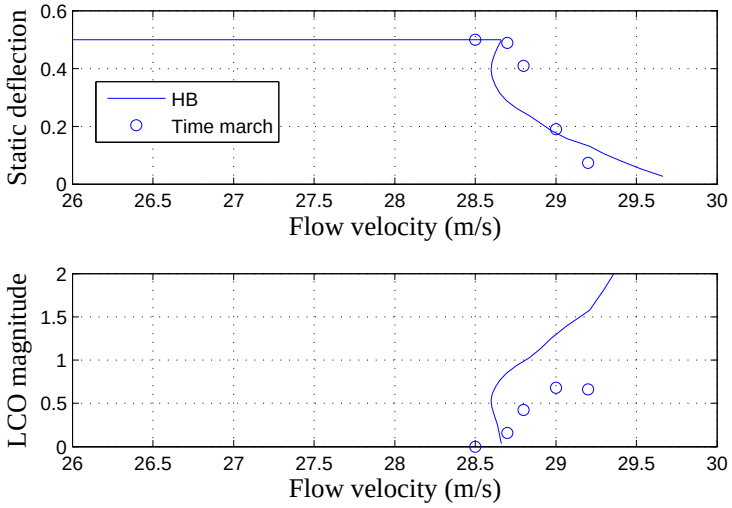

FIGURE 4.23: Static and LCO response for $\theta_{pl} = 0.5$

A transformation of variable was done using the relation, $\alpha = (\sqrt{k_1/k_3})\theta$ and results were obtained for $\theta_{pl} = 0.1$, 0.25, and 0.5, with $k_1/k_{1nominal}$ fixed at unity. These are plotted in Fig. 4.22 along with the no-preload LCO response and the Linear Flutter Speed (LFS) for reference. Also shown is an approximate response with both θ_{pl} and θ_{st} assumed to be 0.5. The LCO response began to deviate from the no-preload case as θ_{pl} increased, with a corresponding increase in LCO onset velocity and the appearance of hysteresis. Preliminary time marching simulations were done and the first two harmonics were extracted from the time histories (see Fig. 4.23). The match with the HB results was approximate, perhaps due to the presence of multiple dominant frequencies, and merits further investigation.

If the cubic nonlinearity was in damping rather than in stiffness, the restoring force, $F(t) = c_1\dot{\alpha}(t) + c_3\dot{\alpha}^3(t)$ would be a function of $\bar{\alpha}$ but independent of α_{pl}. Hence the k_{eff} and the LCO response due to cubic damping are unaffected by the static preload.

5

F-16 Aircraft Model

The wing results presented in the previous Chapters bore certain similarities to the in-flight response of the F-16 [2]. Therefore the same nonlinear mechanisms were considered in the F-16 study, and similar HB based procedures were used to calculate the LCO response. However as explained below, the F-16 modeling procedure was quite different in its details from that of the wing models.

5.1 Linear Structural Model

The Air Force Research Laboratory (AFRL) provided structural data in the form of modal masses, natural frequencies and modeshapes for 26 modes derived from a linear Finite Element (FE) model of the F-16. (The FE model itself was not provided for proprietary reasons.) The natural frequencies went up to 25 Hz, which was adequate since the flutter/LCO phenomena occurred below 10 Hz. The FE grid is shown in Fig. 5.1. It captured the basic geometry including z-offset of the stores, as can be seen by comparing with the 3-view in Fig. 5.2 taken from [33]. Note that the stores configuration in the 3-view differs slightly from the one being analyzed here.

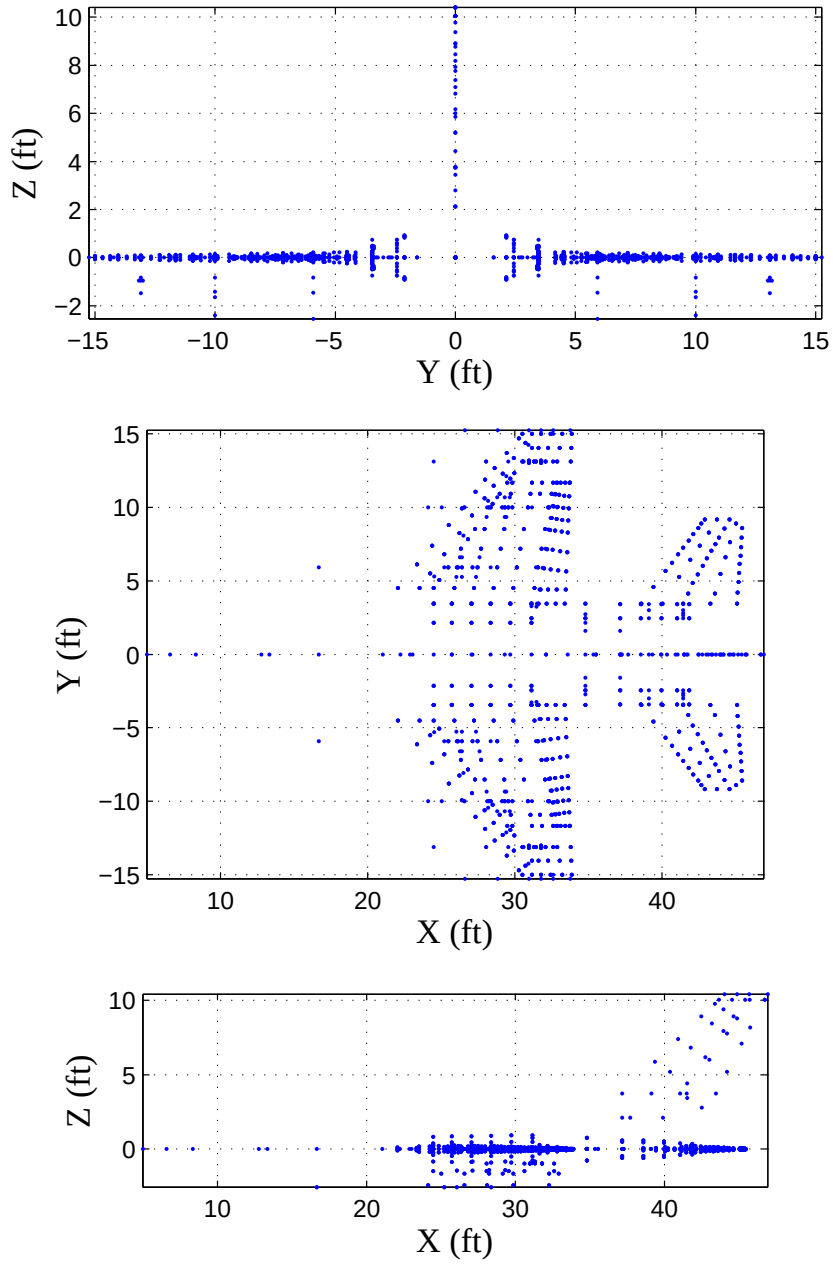

FIGURE 5.1: F-16 structural grid

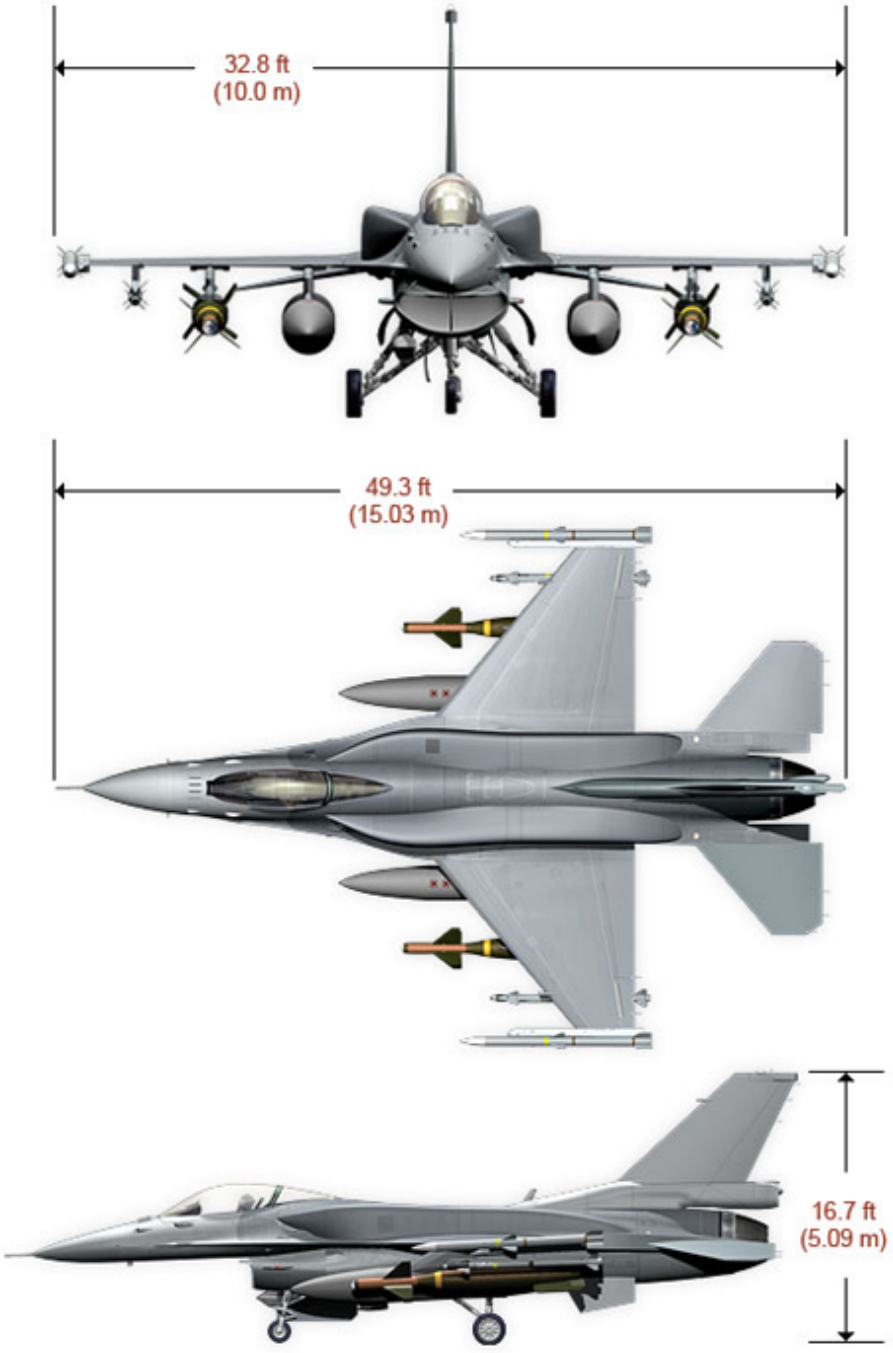

FIGURE 5.2: F-16 3-view

The data was for a symmetric multiple-store configuration that had been flight tested and found to exhibit LCO [34]. Store stations were numbered from 1 (right wingtip) through 9 (left wingtip), with the fuselage station at 5. The stores and their mass properties taken from [34] are listed in Fig. 5.3 and Fig. 5.4 respectively.

Station[a]	Location	x, in.	y, in.	z, in.	Store	Suspension equipment
1	Wingtip	380.46	180.00	92.00	None	LAU-129/A launcher
2	Underwing	371.56	157.00	91.35	AIM-9P missile	LAU-129/A launcher
3	Underwing	349.67	120.00	90.72	Air-ground missile	Launcher/pylon
4	Underwing	316.87	71.00	90.02	Empty 370-gallon fuel tank	Fuel tank pylon

FIGURE 5.3: Wing stores for LCO configuration

		Center of gravity[a]			Moments of inertia, slug-ft.^{2}		
Store	Weight, lb	x, in.	y, in.	z, in.	Roll	Pitch	Yaw
LAU-129/A wingtip launcher	84.9	−15.20	0.00	−0.01	—	13.73	13.70
AIM-9P missile, LAU-129/A underwing launcher, and missile pylon	276.3	−14.65	0.01	−13.30	1.31	68.63	67.77
Air-ground missile, launcher, and weapon pylon	898.7	−2.27	0.02	−20.72	19.72	134.74	116.95
370 gallon fuel tank (empty) and pylon	470.5	−1.85	−0.18	−10.00	—	197.93	187.64

FIGURE 5.4: Store mass properties

Earlier LCO simulation studies, e.g., [11, 35] had focused mainly on the Stations 1/9 and 2/8 stores and their associated aerodynamic nonlinearities. However, it was decided to introduce the structural nonlinearity first at Stations 3/7 because this store assembly was at least twice as heavy as the others and its pitching mode was known to participate in linear model flutter. Subsequently, nonlinearity at Stations 2/8 was also considered.

5.2 Modification of Wing-Store Attachment

To accommodate the nonlinearity for the HB method, the attachment stiffness and/or damping were modified on both wings.[1] In the absence of the FE model, this modification had to be carried out directly on the aircraft structural modes. The dynamic decoupling/coupling procedure detailed in [36] was used for this purpose, in a modified form. The method is based on constraint definitions between the wing and store, and the use of Lagrange multipliers; the wing motion must be expanded using the original eigenmodes as primitive modes, and the resulting reduced order equation solved for the new natural frequencies and other modal parameters. In the present case, where two DOF (heave, h_s and pitch, α_s relative to wing) and three inertial properties (mass, m_s; static unbalance, S_1 and moment of inertia, I_1 with respect to attachment location) need to be taken into account for each store, this approach turned out to be cumbersome. Hence, a simpler route of directly substituting the constraints into the kinetic and potential energy terms was adopted here, followed by application of Lagrange's equations. The method was applied in two steps to (i) subtract the stores from both wings assuming a rigid attachment and (ii) add them back with the desired stiffness and damping.

For purposes of clarity, the process of adding a single store is illustrated here. The kinetic energy, T and elastic potential energy, V of the wing-with-store are given by Eqn. 5.1, where M_n & q_n are *wing-without-store* modal masses and generalized coordinates respectively, and x_{12} is the distance from the store attachment point (Point 1) to the reference point for calculating store rotation (Point 2). Wing vertical displacements (positive up) at the store attachment points, η_1 & η_2 are given by Eqn. 5.2 in terms of wing-without-store eigenmodes, ψ_1 and ψ_2.

[1] 'Dynamics' models used for aircraft vibration analysis typically have very stiff/rigid wing-store attachments. Examination of wing and store modal displacements along the chord at the relevant store station confirmed that this was true of the F-16 model as well.

$$T = \frac{1}{2}\sum_{1}^{N} M_n \dot{q_n}^2 + \frac{1}{2} m_s (\dot{\eta_1} + \dot{h_s})^2 - S_1 (\dot{\eta_1} + \dot{h_s})(\frac{\dot{\eta_1} - \dot{\eta_2}}{x_{12}} + \dot{\alpha_s}) + \frac{1}{2} I_1 (\frac{\dot{\eta_1} - \dot{\eta_2}}{x_{12}} + \dot{\alpha_s})^2 \tag{5.1a}$$

$$V = \frac{1}{2}\sum_{1}^{N} M_n \omega_n^2 q_n^2 + \frac{1}{2} K_h h_s^2 + \frac{1}{2} K_\alpha \alpha_s^2 \tag{5.1b}$$

$$\eta_1 = \sum_{1}^{N} \psi_1 q_n \quad ; \quad \eta_2 = \sum_{1}^{N} \psi_2 q_n \tag{5.2}$$

Note that the S_1 term has a different algebraic sign than the others because of adopting the (positive up) store *heave* as a DOF, instead of the usual plunge. Also, if the store was to be subtracted instead of added, algebraic signs of the store inertia terms would be reversed; if the attachment was rigid ($h_s = 0 = \alpha_s$) the equations would take on a simpler form; if the attachment was flexible in the lateral direction also, additional terms would be present. After combining Eqns. 5.1 and 5.2, the application of Lagrange's equations with respect to q_n, h_s and α_s yielded the governing equations for the new system, with nonconservative generalized forces to account for the store attachment damping.

Alternatively, the damping in the wing-store attachment was modified while the stiffness was held fixed. Again, the direct substitution procedure was used. (Equations for the Lagrange multiplier approach were also derived, and are given in Appendix C.)

Finally, the modified modes were obtained by eigenanalysis: the eigenvalues provided the new natural frequencies and modal damping factors while the eigenvectors provided the weighting factors needed to linearly combine the old modeshapes and thereby obtain the new modeshapes.

5.3 HB-CFD based Aeroelastic Analysis

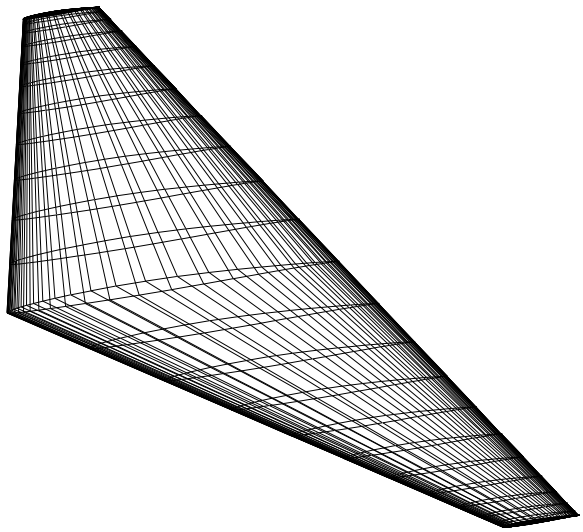

FIGURE 5.5: Wing surface CFD grid

In the aerodynamic model, the F-16 wing was extended up to the fuselage centerline, and its complete geometry in terms of thickness, camber and twist was incorporated. The CFD grid consisted of 65 points around the wing section, 33 points in the normal direction and 49 points along the span, totalling 105,105 grid points (see Figs. 5.5, 5.6). The aeroelastic models with modified wing-store attachments were analyzed using the Duke RANS CFD Harmonic Balance solver with 1 harmonic/ 3 subtime levels. With 6 flow variables per grid point, there was a total of 1,891,890 DOF. The solver yielded the neutral stability Mach number and frequency along with the aeroelastic eigenvector, ξ, when the flight altitude and the first element of the eigenvector, ξ_1 were specified. Throughout this work, ξ_1 was set to a very small value in order to achieve *dynamic linearization* of the aerodymanics. In other words, the steady flow (or static) aerodynamic nonlinearities were taken into account whereas

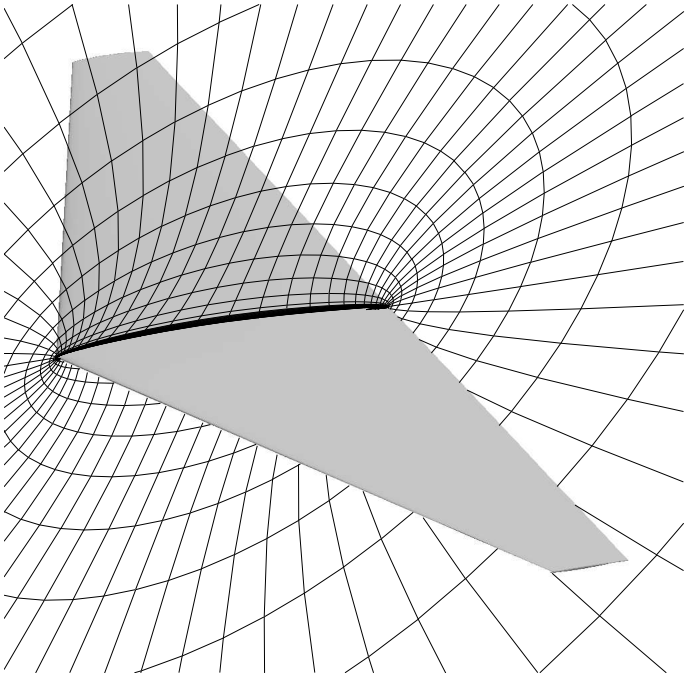

FIGURE 5.6: Symmetry plane CFD grid

the unsteady aerodynamic forces were proportional to the structural motion. Consequently the CFD results pertained to flutter rather than to LCO, as modified by steady flow nonlinearities, and this allowed the structural nonlinearity to be studied in isolation using HB. Alternatively, specifying a larger value of ξ_1 would make the aerodynamic model *dynamically nonlinear* and the neutral stability solutions would represent LCO due to aerodynamic nonlinearity. Those results can be used to obtain the combined effect of aerodynamic and structural nonlinearity, again using HB.

The highest fidelity CFD computer runs typically took several days to complete, and it was important to feed in optimized initial conditions for numerical convergence. Therefore, approximate flutter analyses were often done first to obtain trend plots of flutter altitude vs Mach number, and these were used to decide the initial conditions for the more accurate CFD simulations. In the approximate analyses, solution snapshots were computed for various frequencies at each fixed Mach number. The resulting unsteady aerodynamic loading were then curve fit, and a search in

the space of frequency and altitude was conducted to determine the combination of frequency and altitude where the determinant of the aeroelastic governing equations was closest to zero. The aerodynamic theory for the approximate analyses was the same as for the full harmonic balance aeroelastic LCO solver, namely viscous RANS.

5.4 LCO Calculation Method

LCO responses in the nonlinear DOF (h_s or α_s) were obtained by the same method that was used for the wing models, namely by combining the (dynamically linear) flutter boundary with the DF of the nonlinearity. As pointed out earlier, a single flutter boundary can yield a family of responses depending on the value assigned to the nominal linear parameter (in stiffness or damping, as the case may be). This can be a great benefit when time marching is computationally expensive.

Comparison with flight test data requires absolute accelerations at the wingtip launcher for example, and these were obtained by a two-step process. Equation 5.3 relates the flutter eigenvector, ξ to physical displacements at the wingtip, η_{tip} via intermediate eigenvectors, E.

$$\begin{Bmatrix} \{q\} \\ h_s \\ \alpha_s \end{Bmatrix} = [E]\{\xi\} \quad ; \quad \eta_{tip} = \sum_{1}^{n} \psi_n q_n = [\Psi_{wos}]\{q\} \tag{5.3}$$

Note that $\Psi_{ws} = \Psi_{wos}E$, with E obtained during the dynamic coupling process when the store was added back with finite attachment stiffness. Keeping in mind that each effective K_{h_s} had an associated $\bar{h}_s$ value (for the case of h_s nonlinearity), the corresponding ξ (and thus q), were scaled to ensure that $E\xi$ yielded *that* $\bar{h}_s$. Then, η_{tip} was obtained from either $\Psi_{wos}q$ or $\Psi_{ws}\xi$ - both gave the same results, of course. Finally, the acceleration magnitudes were obtained as $\ddot{\eta}_{tip} = \omega^2\eta_{tip}$ with ω taken from the flutter frequency curve. The procedure is illustrated in Fig. 5.7.

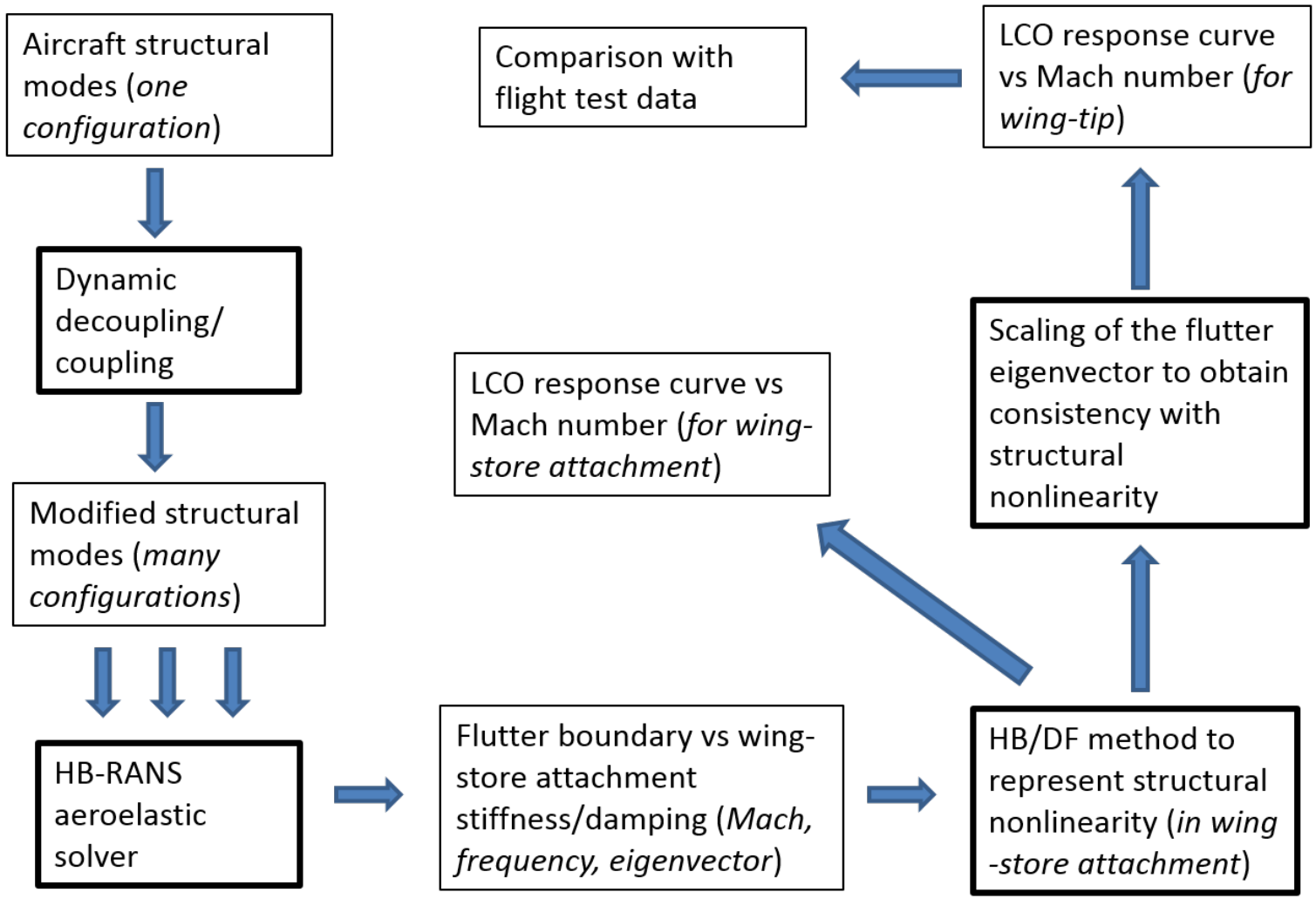

FIGURE 5.7: F-16 LCO response calculation with structural nonlinearity and steady flow aerodynamic nonlinearities combined

6

F-16 Results

The F-16 study examined the effects of nonlinear wing-store attachment stiffness and damping on LCO, independently in the h_s and α_s DOF of wing span Stations 3/7 and the α_s DOF of wing span Stations 2/8 (see Fig. 6.1). The nonlinearities considered are listed in Table 2.2.

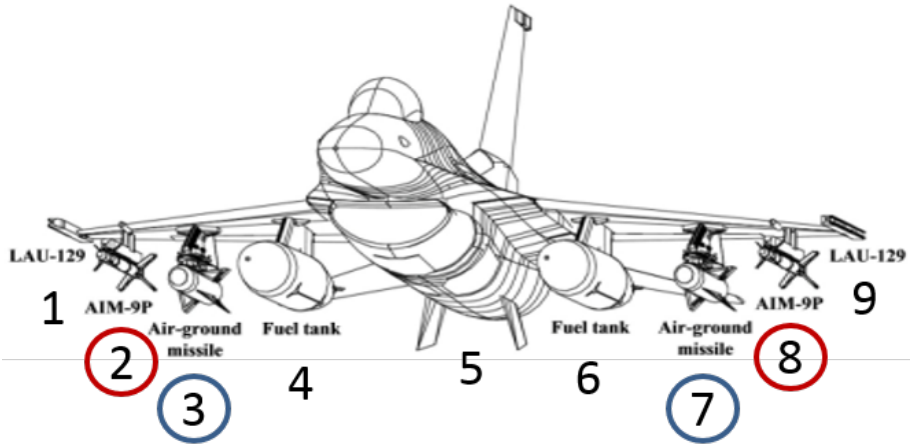

FIGURE 6.1: F-16 store locations analyzed

6.1 Structural Dynamics

From the aircraft model with stores provided by AFSEO, stores at the stations of interest were subtracted while leaving the other stores untouched. The removed stores were then added back with attachment stiffnesses corresponding to various uncoupled store plunge frequencies, f_{h_s} ranging from 0.1-25 Hz, while keeping the uncoupled store pitch frequency, f_{α_s} at a relatively rigid 25 Hz. The converse was also done, namely variation of f_{α_s} while f_{h_s} was fixed. In both cases, the structural damping was zero.

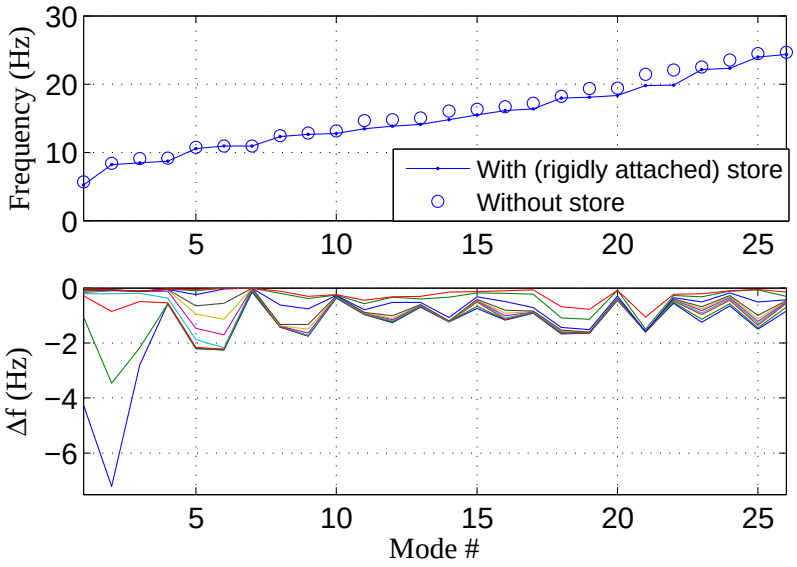

FIGURE 6.2: Effect of store removal (top) and attachment flexibility (bottom) at Stations 3/7

When the stores were removed all the natural frequencies went up, and when they were put back on flexible attachments the new frequencies were lower than the original frequencies with stores. These variations were found to be consistent with the established trends for mass/stiffness changes in elastic structures [37]. Typical results are shown in Fig. 6.2 for wing span Stations 3/7; the lower plot shows

modal frequency changes, with successive curves corresponding to increasing levels of attachment flexibility.

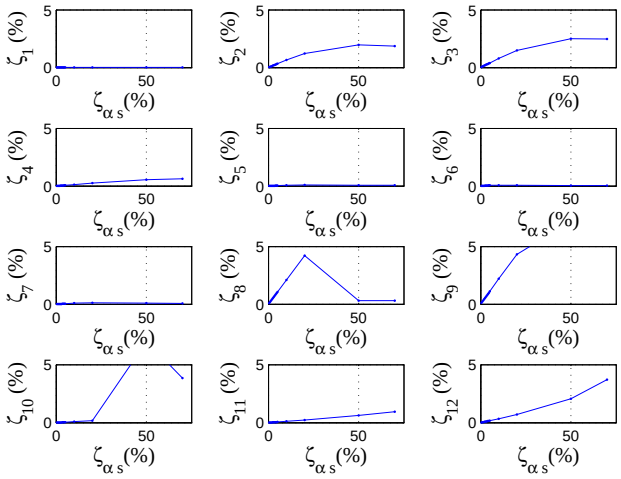

FIGURE 6.3: Modal damping due to ζ_{α_s} introduced at Stations 3/7

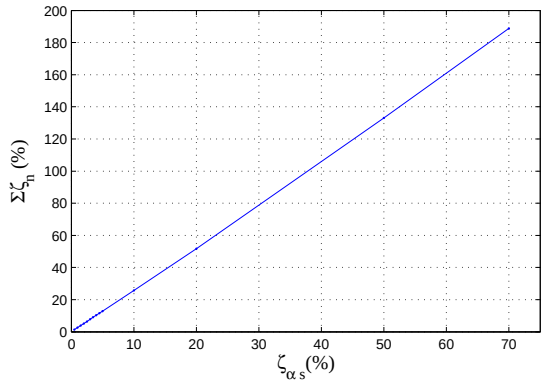

FIGURE 6.4: Sum of modal damping, Stations 3/7

Next, ζ_{h_s} and ζ_{α_s} were varied individually while f_{h_s} and f_{α_s} were fixed. (The frequency in the nonlinear DOF was 15 Hz while the other frequency was 25 Hz. These values were chosen keeping in view that too stiff an attachment would overshadow the damping effects.) Figure 6.3 plots modal damping factors, ζ_n for the first 12

modes against ζ_{α_s}. (As a rule of thumb when using primitive modes, the first half of the final modes is considered to be accurate.) The introduced damping propagated to various degrees into the aircraft modes depending on the store displacement content of the modes. As ζ_{α_s} was increased, all the ζ_n increased at first, but some of them started to decrease subsequently. While it was not clear why the latter behavior occurred, the damping summed over all modes was seen to vary linearly (with a slope of 2.7), pointing to some global simplicity (see Fig 6.4).

6.2 Flutter

For each modified case, the CFD Harmonic Balance solution was calculated for an altitude of 2000 ft and a mean angle of attack of 1.5°. The first element of the aeroelastic eigenvector, ξ_1 was set to a small value of 0.0001 ft in the analysis, so that the aerodynamic forces were dynamically linearized while accounting for steady flow nonlinearities such as airfoil profile effects. Since the flight test LCO deflections reported for this configuration were always antisymmetric, the computations were done with the first few antisymmetric modes only.

Figure 6.5 shows the flutter boundary as a function of store suspension frequency, f_{h_s}. The ends of the boundary approached (i) the rigid attachment case, for high f_{h_s} and (ii) the case of store being free in plunge but rigid in pitch, for low f_{h_s}. When f_{h_s} crossed the wing bending/torsion frequency range in the rigid attachment case (8-10 Hz), the flutter-interacting mode pair switched from (1, 2) to (2, 3) accompanied by jumps in flutter Mach number and flutter frequency.[1] Figure 6.6 shows the F-16 flutter boundary as a function of f_{α_s} to be somewhat similar, but with a greater range of flutter Mach and a broader frequency range (4-10 Hz) over which flutter did not appear to exist. Results for $f_{h_s} = f_{\alpha_s} = 15\,Hz$ also indicated that the flutter Mach number was more sensitive to f_{α_s} than to f_{h_s}.

[1] One may recall a similar switch in the generic wing case, Fig. 4.3.

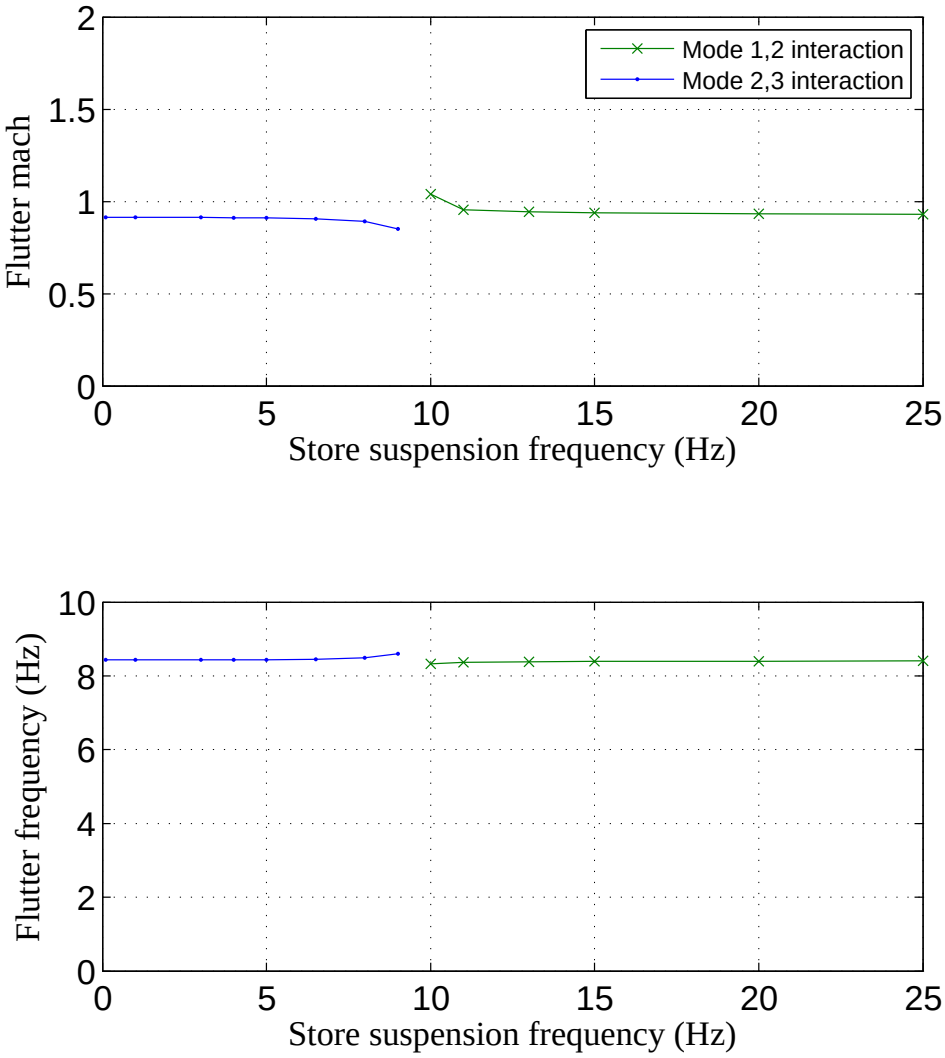

FIGURE 6.5: Flutter boundary vs f_{h_s}, Stations 3/7

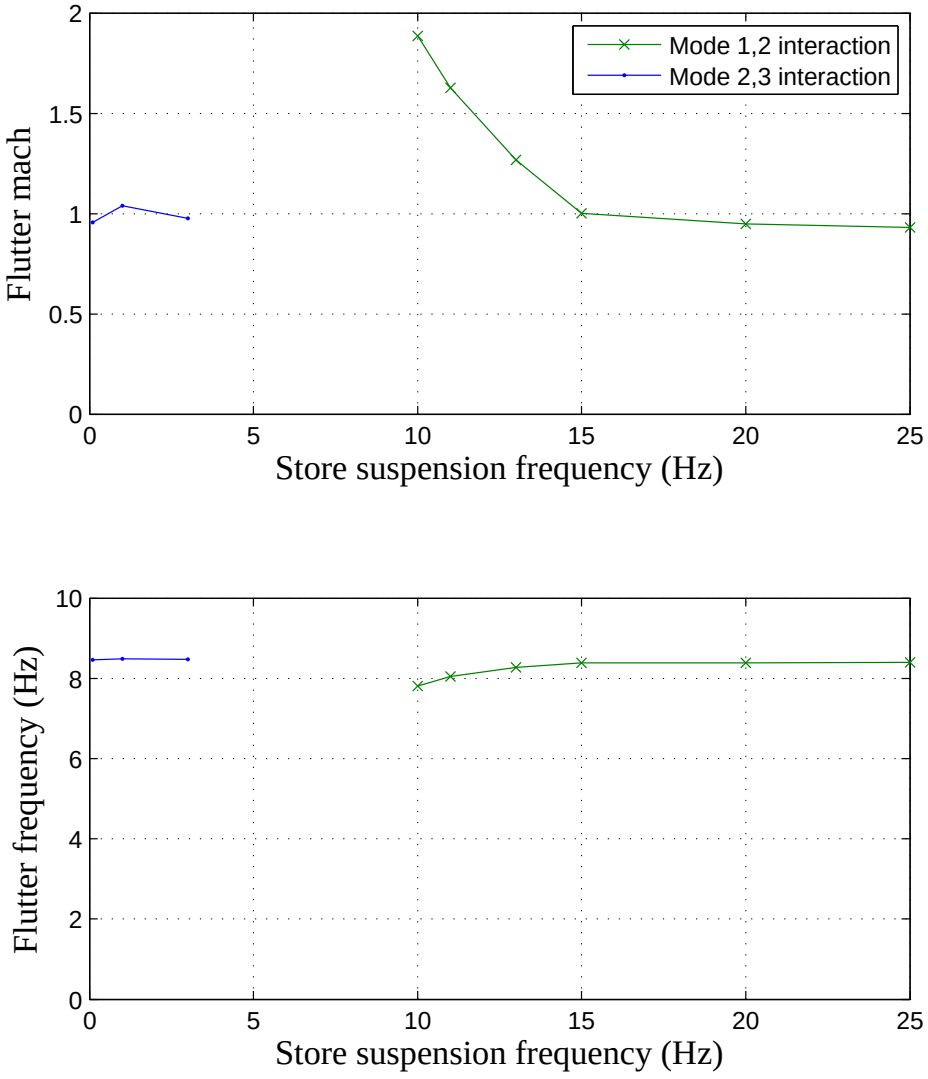

FIGURE 6.6: Flutter boundary vs f_{α_s}, Stations 3/7

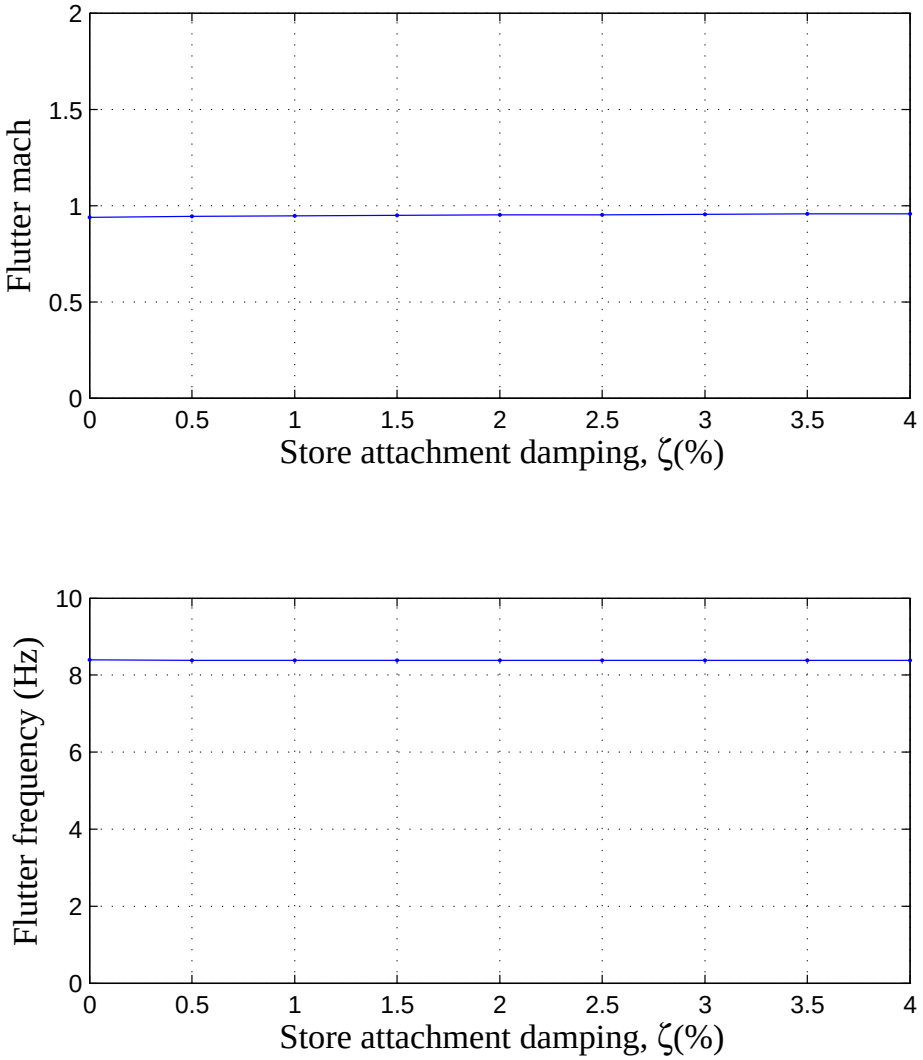

FIGURE 6.7: Flutter boundary vs ζ_{h_s}, Stations 3/7

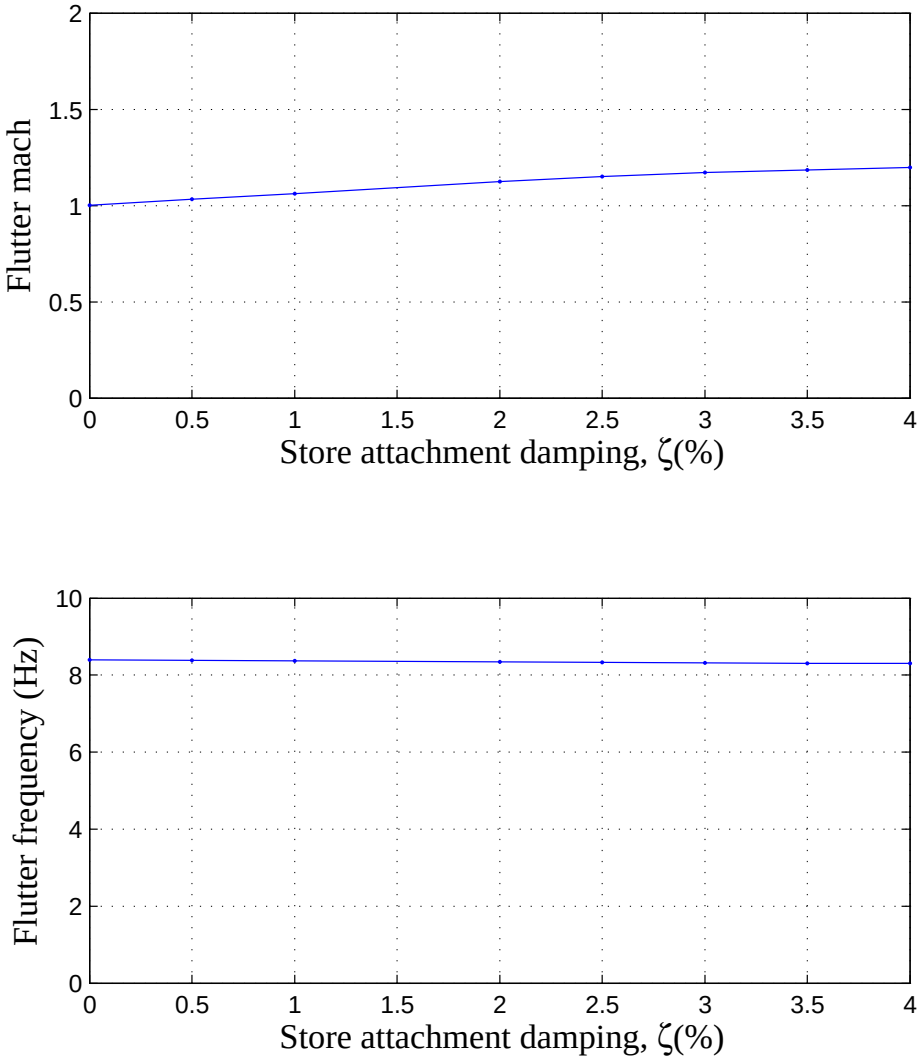

FIGURE 6.8: Flutter boundary vs ζ_{α_s}, Stations 3/7

The flutter boundary with respect to wing-store attachment damping, ζ_{h_s} for $f_{h_s} = 15\,Hz$ and $f_{\alpha_s} = 25\,Hz$ is shown in Fig. 6.7. The flutter boundary with respect to ζ_{α_s} for $f_{\alpha_s} = 15\,Hz$ and $f_{h_s} = 25\,Hz$ is shown in Fig. 6.8. The flutter velocity increased monotonically with damping and was more sensitive to ζ_{α_s} than to ζ_{h_s}.

6.3 LCO due to Nonlinear Stiffness

6.3.1 Cubic Stiffness

The above flutter boundaries in combination with cubic hardening stiffness resulted in unstable rather than stable LCO, which did not agree with the flight test data. On the other hand, cubic softening stiffness led to stable LCO. Figure 6.9 shows LCO responses for cubic softening in h_s with nominal $f_{h_s} = 25Hz$ and $k_3/k_1 = 1.25 \times 10^6\ ft^{-2}$. The responses include store acceleration, $\ddot{h}_s$ and wing tip accceleration, $\ddot{\eta}_{tip}$, along with flight test data for the latter. The h_s and η_{tip} profiles differed from each other because h_s was directly determined from the assumed nonlinearity and was $O(\sqrt{k_1/k_3})$ - 0.001 ft in this case, while η_{tip} was a function of the flutter eigenvector also.

Figure 6.10 shows LCO responses for cubic softening in α_s with nominal $f_{\alpha_s} = 25Hz$ and $k_3/k_1 = 1.25 \times 10^6\ rad^{-2}$.

6.3.2 Freeplay Stiffness

Assuming freeplay stiffness led to unstable LCO only, which did not agree with the flight test data.

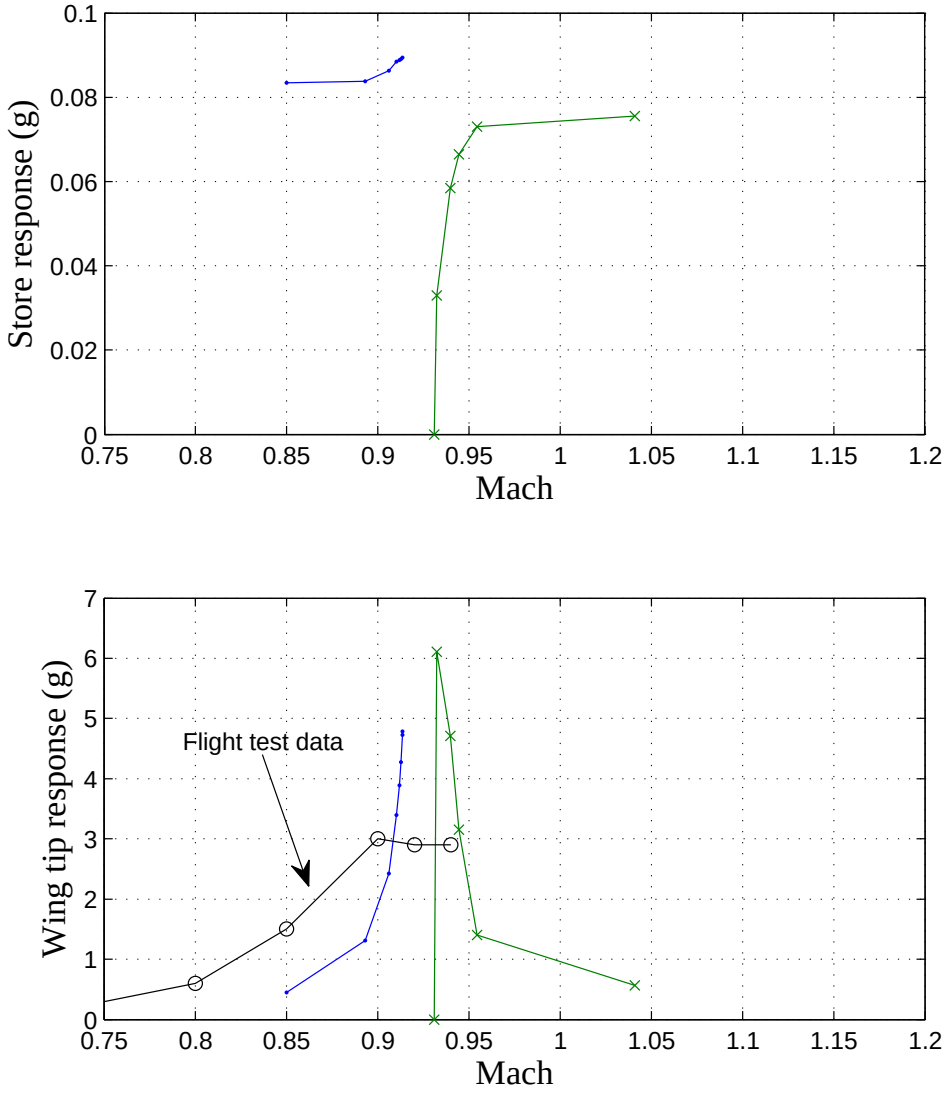

FIGURE 6.9: LCO response due to cubic softening stiffness in h_s, Stations 3/7

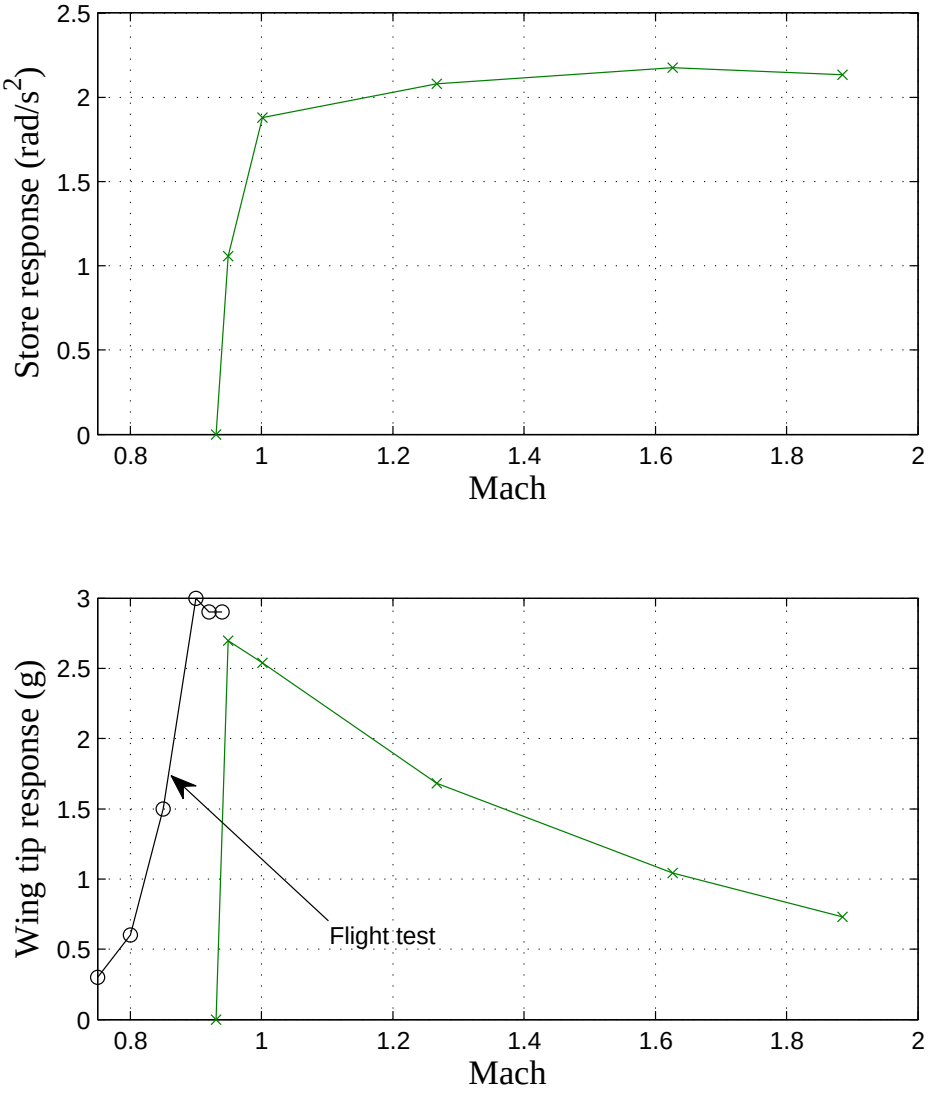

FIGURE 6.10: LCO response due to cubic softening stiffness in α_s, Stations 3/7

6.4 LCO due to Nonlinear Damping

6.4.1 Cubic Damping

Figures 6.11, 6.12 show LCO responses due to positive cubic damping in h_s and α_s respectively. They were calculated for nominal $\zeta_{h_s} = \zeta_{\alpha_s} = 2\%$ and $c_3/c_1 = 2.5 \times 2.5 \times 10^5\ s^2/ft^2$. In the nonlinear α_s case, the Mach number variation was consistent with that of the flight test data, and was accompanied by a reasonable variation of 0%-4% in ζ_{α_s} (see Fig. 6.8).

Negative cubic damping led to unstable LCO only, which did not agree with the flight test data.

6.4.2 Freeplay Damping

LCO responses due to freeplay damping in h_s and α_s are shown in Figs. 6.13, 6.14. In both cases, nominal linear damping, $\zeta = 2\%$, was present in the nonlinear DOF. In the nonlinear α_s case, the Mach number variation was consistent with that of the flight test data.

The freeplay gap, δ was $1.75 \times 10^{-4}\ ft$ for the nonlinear h_s case and $1.75 \times 10^{-4}\ rad$ for the nonlinear α_s case.

6.4.3 Friction

LCO responses due to friction damping for unit frictional force/torque in the wing-store attachment are shown in Fig. 6.15. A nominal linear damping, $\zeta = 2\%$, was present in the nonlinear DOF. Friction led to unstable supercritical LCO that represented a minimum initial condition to enter LCO. If the damping were increased further, the flutter velocity can be expected to converge to the rigid attachment case (in the corresponding DOF) and the LCO curve to go to zero magnitude at that velocity.[2] However these results were not consistent with the flight test data.

[2] This was true of the generic wing also, see Fig. 4.15

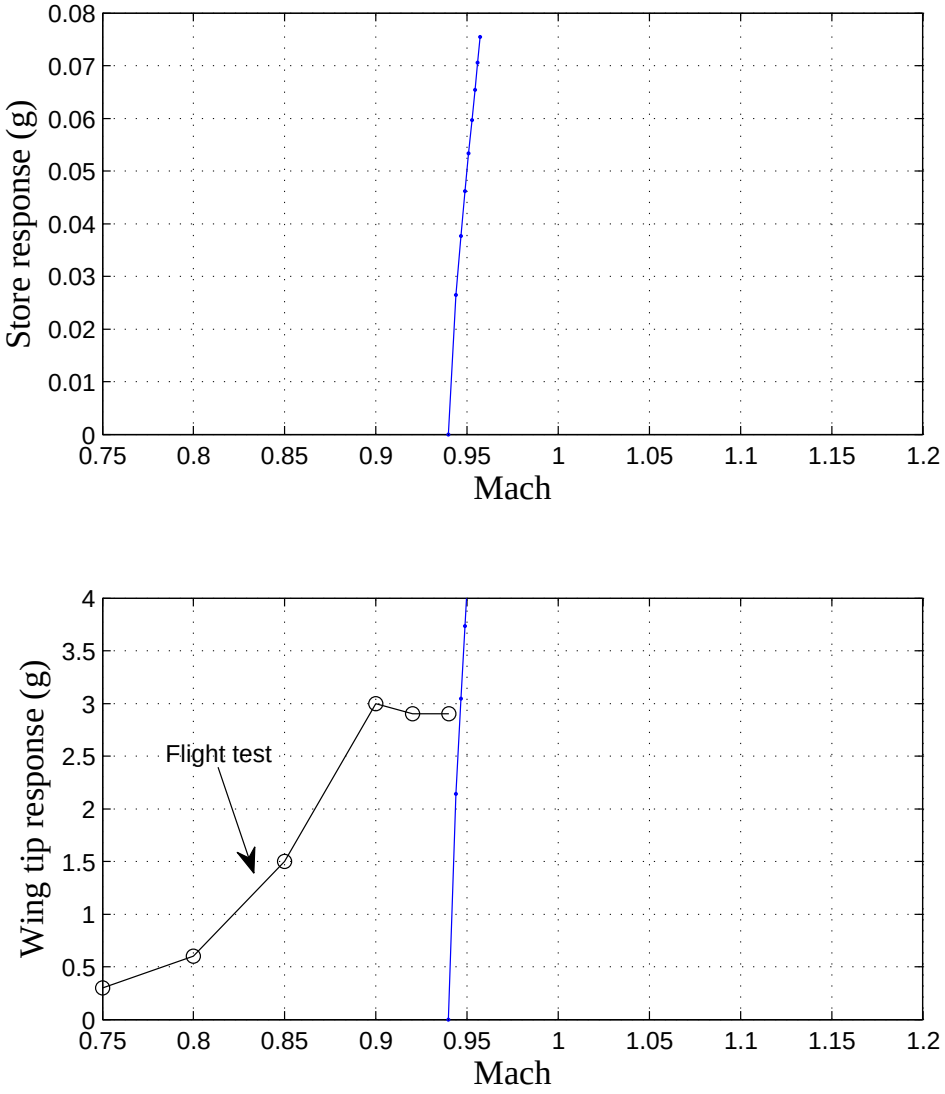

FIGURE 6.11: LCO response due to positive cubic damping in h_s, Stations 3/7

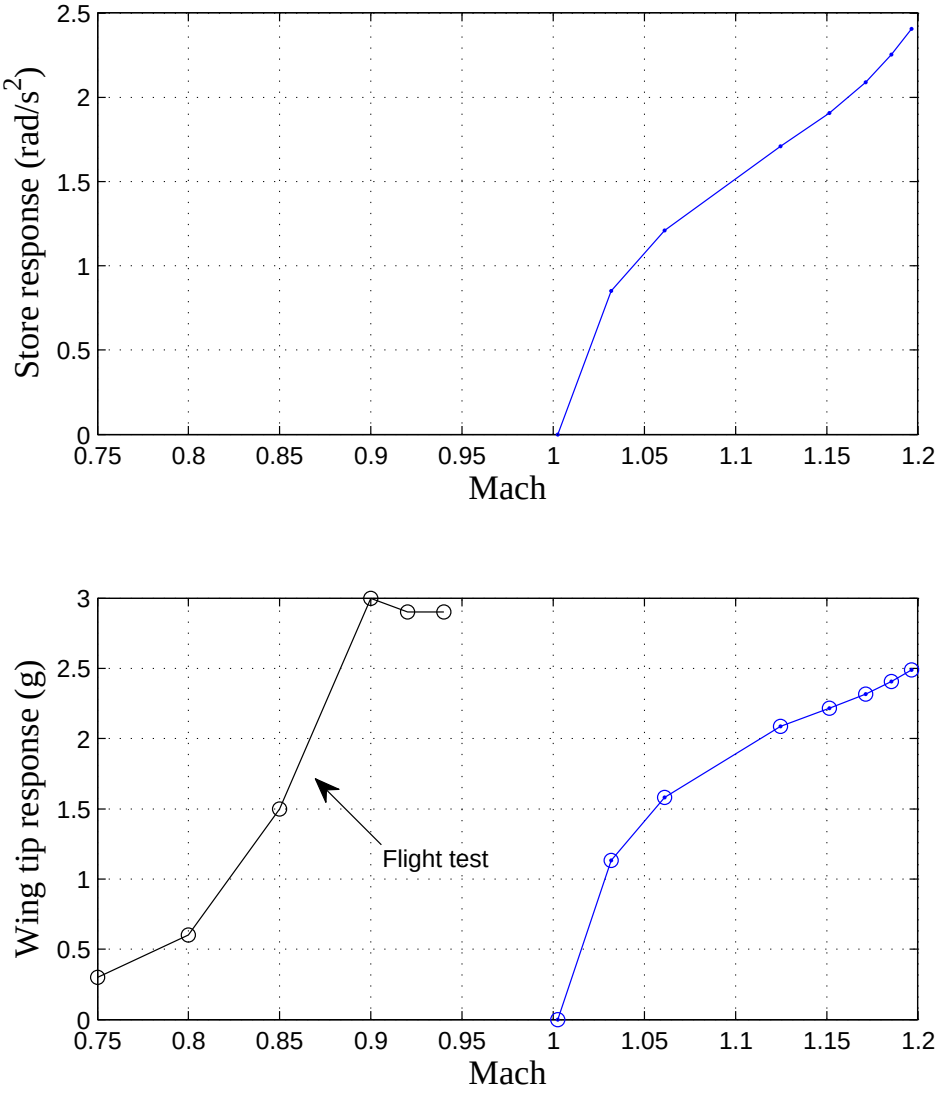

FIGURE 6.12: LCO response due to positive cubic damping in α_s, Stations 3/7

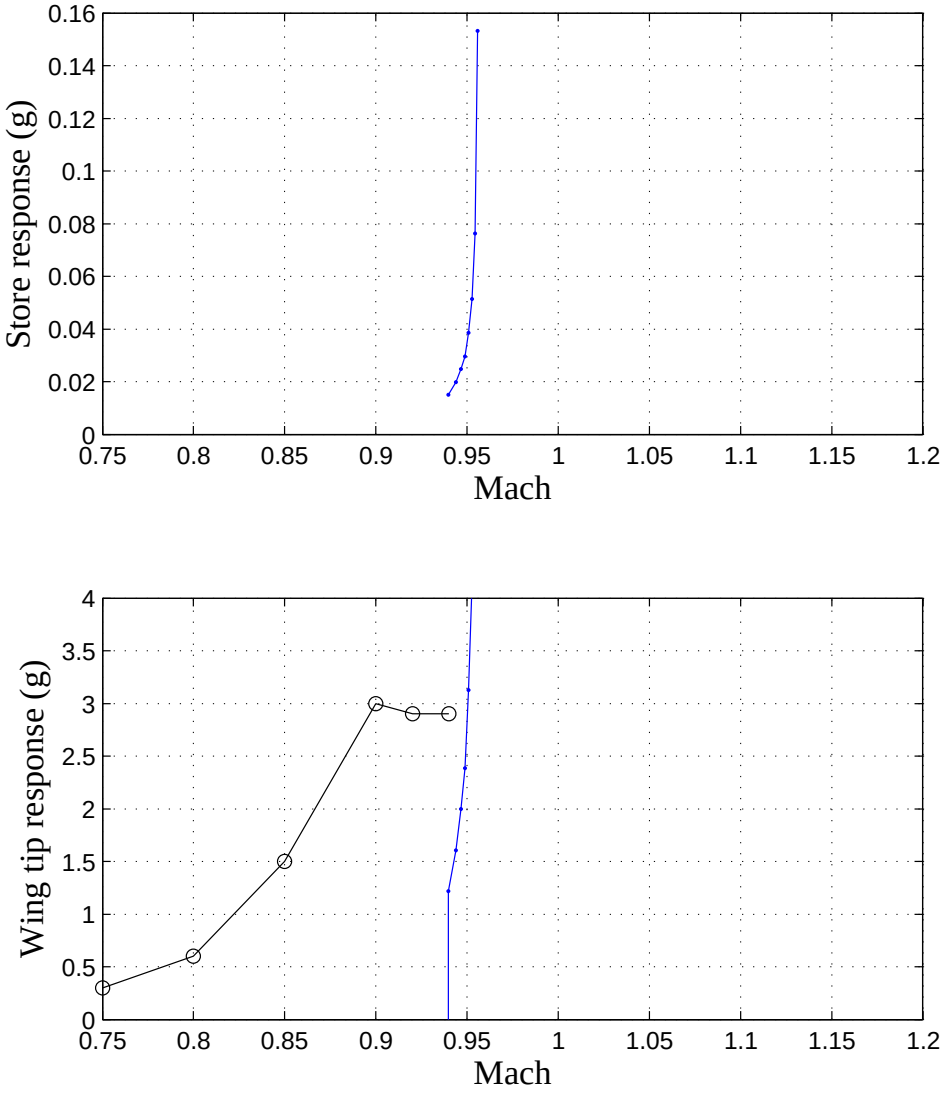

FIGURE 6.13: LCO response due to freeplay damping in h_s, Stations 3/7

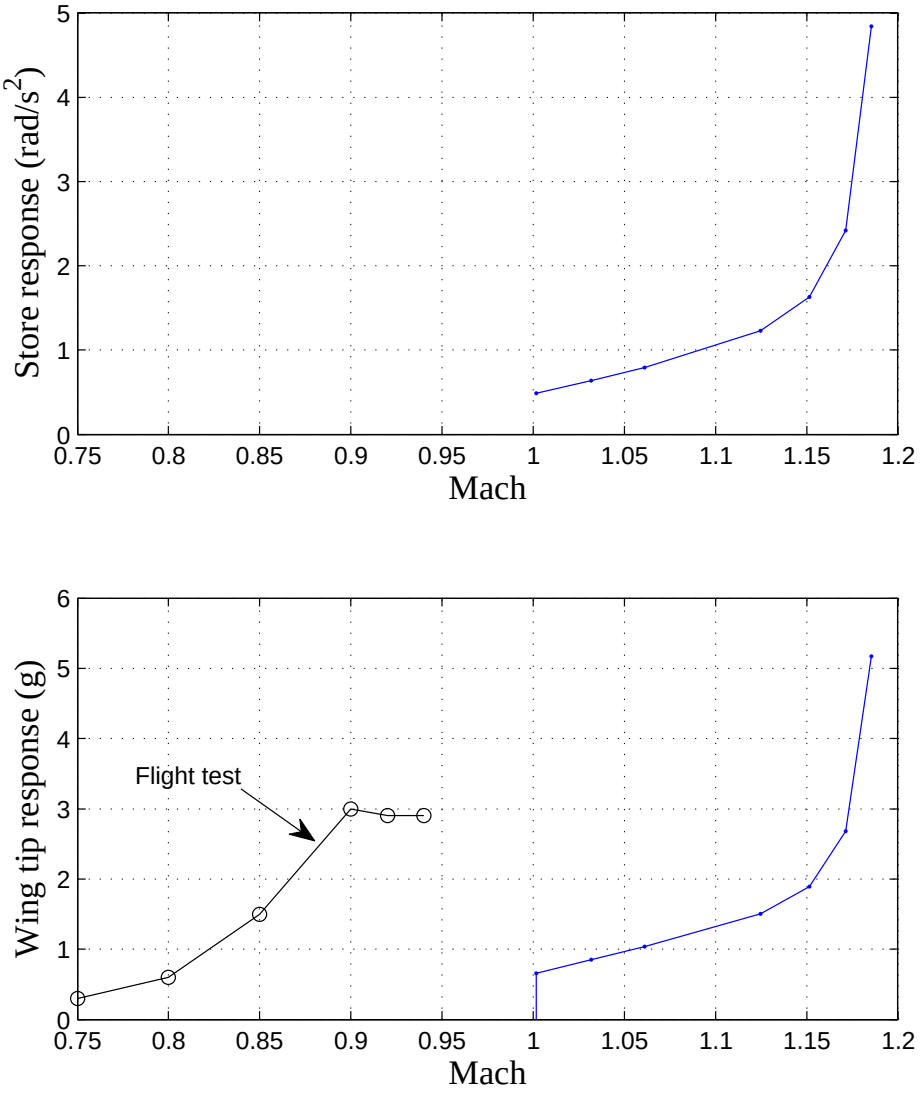

FIGURE 6.14: LCO response due to freeplay damping in α_s, Stations 3/7

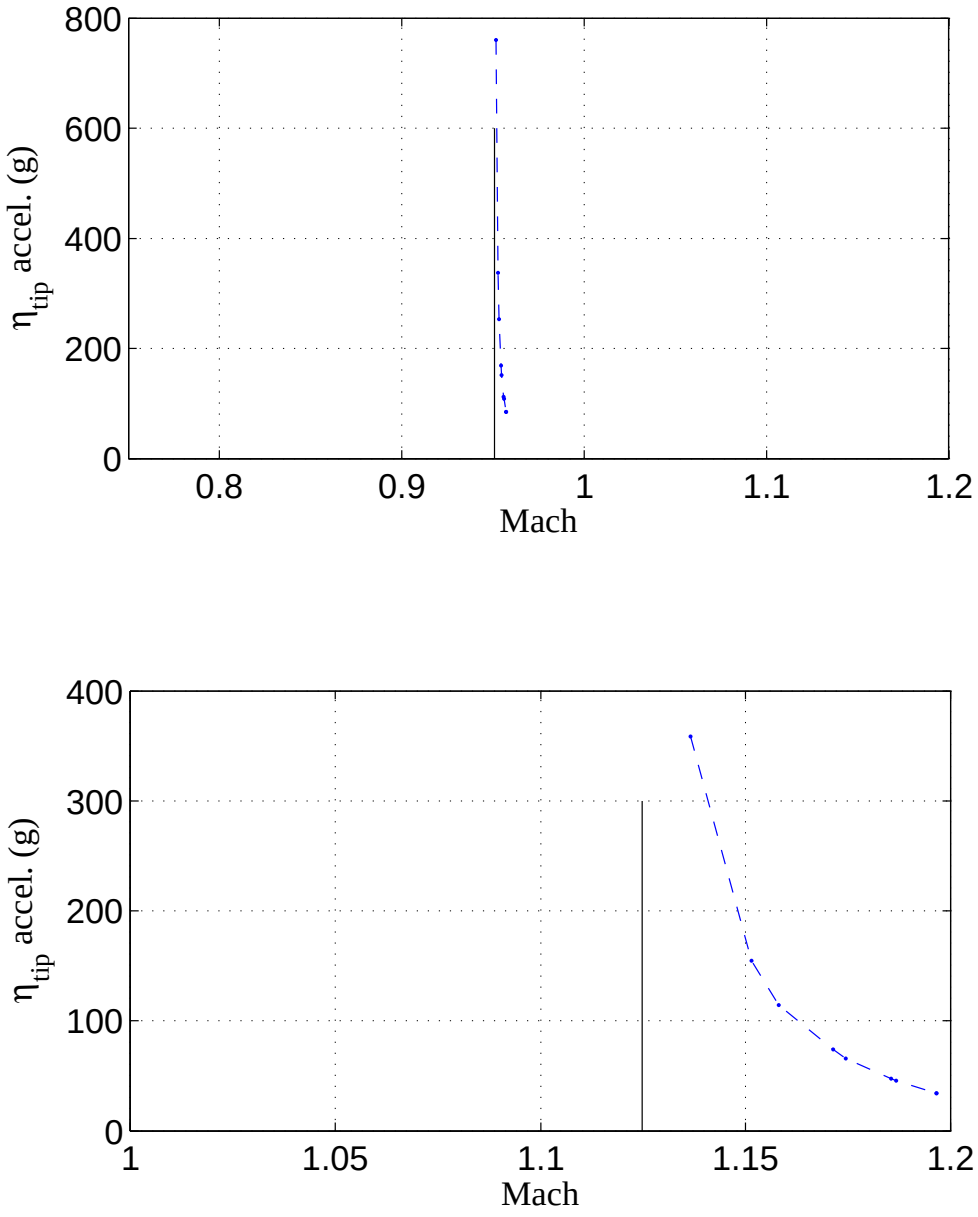

FIGURE 6.15: LCO response due to friction damping in h_s (top) and α_s (bottom)

6.5 Results for Wing Span Stations 2/8

After modifying the wing-store attachments at Stations 2/8, HB-CFD analyses were conducted with the same parameters as for the Stations 3/7 cases previously considered, namely altitude of 2000 ft, angle of attack of 1.5° and ξ_1 of 0.0001 ft.

6.5.1 Nonlinear Stiffness

The flutter boundary with respect to f_{α_s} is shown in Fig. 6.16. The flutter Mach number increased as f_{α_s} was brought down from a high value, reaching Mach 1.5 at $f_{\alpha_s} = 13\,Hz$. This behavior was comparable to the Stations 3/7 case at larger f_{α_s} (see Fig. 3.11).

LCO response due to cubic softening stiffness with nominal $f_{\alpha_s} = 20\,Hz$ and $k_3/k_1 = 2.5 \times 10^5\ rad^{-2}$ is shown in Fig. 6.17.

6.5.2 Nonlinear Damping

The flutter velocity increased monotonically but marginally with ζ_{α_s}, as shown in Fig. 6.18. LCO responses due to cubic, freeplay and friction damping are shown in Fig. 6.19. They were all restricted to a narrow Mach number range. Only the cubic damping case showed even a qualitative similarity to the flight test data.

6.6 Further Flutter Results

In some cases, the HB solver failed to converge to a solution despite refinement of the initial conditions. Examination of flutter altitude vs Mach number trends confirmed the absence of flutter in these cases due to 'hump' mode behavior (Fig. 6.20).

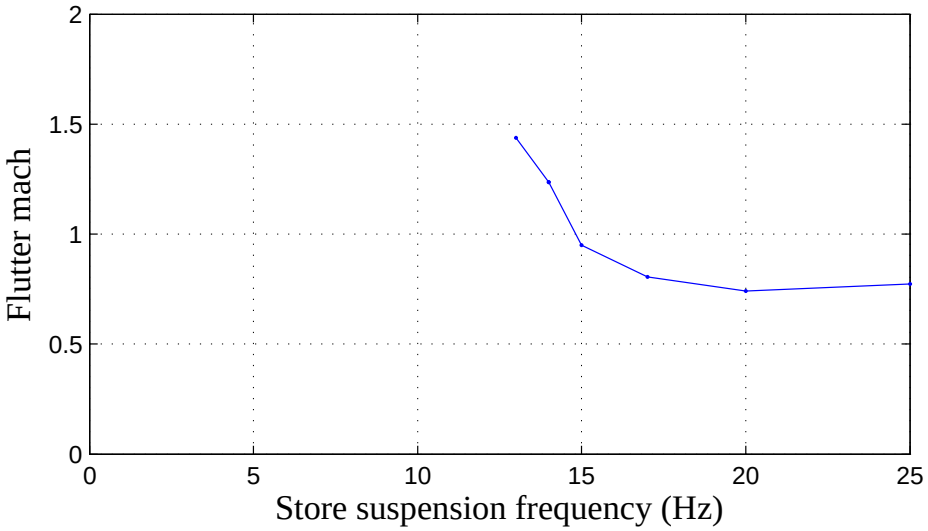

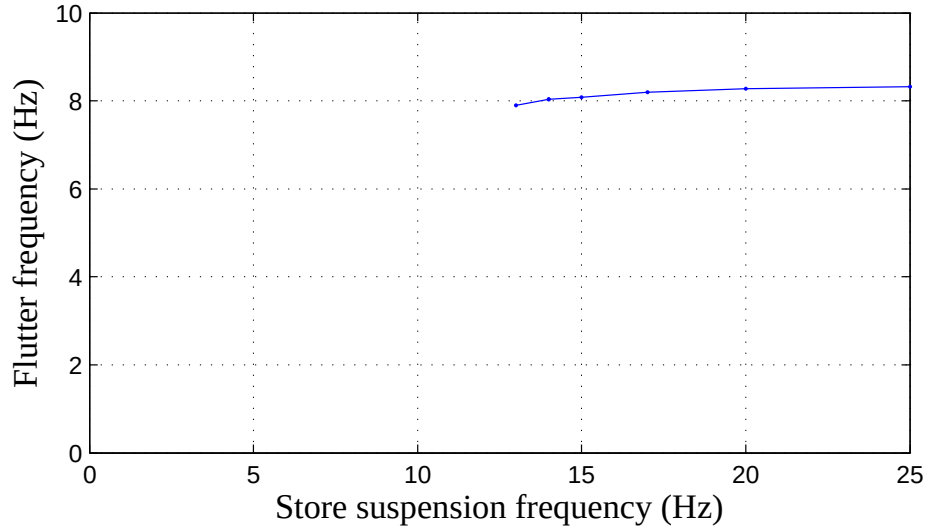

FIGURE 6.16: Flutter boundary vs f_{α_s}, Stations 2/8

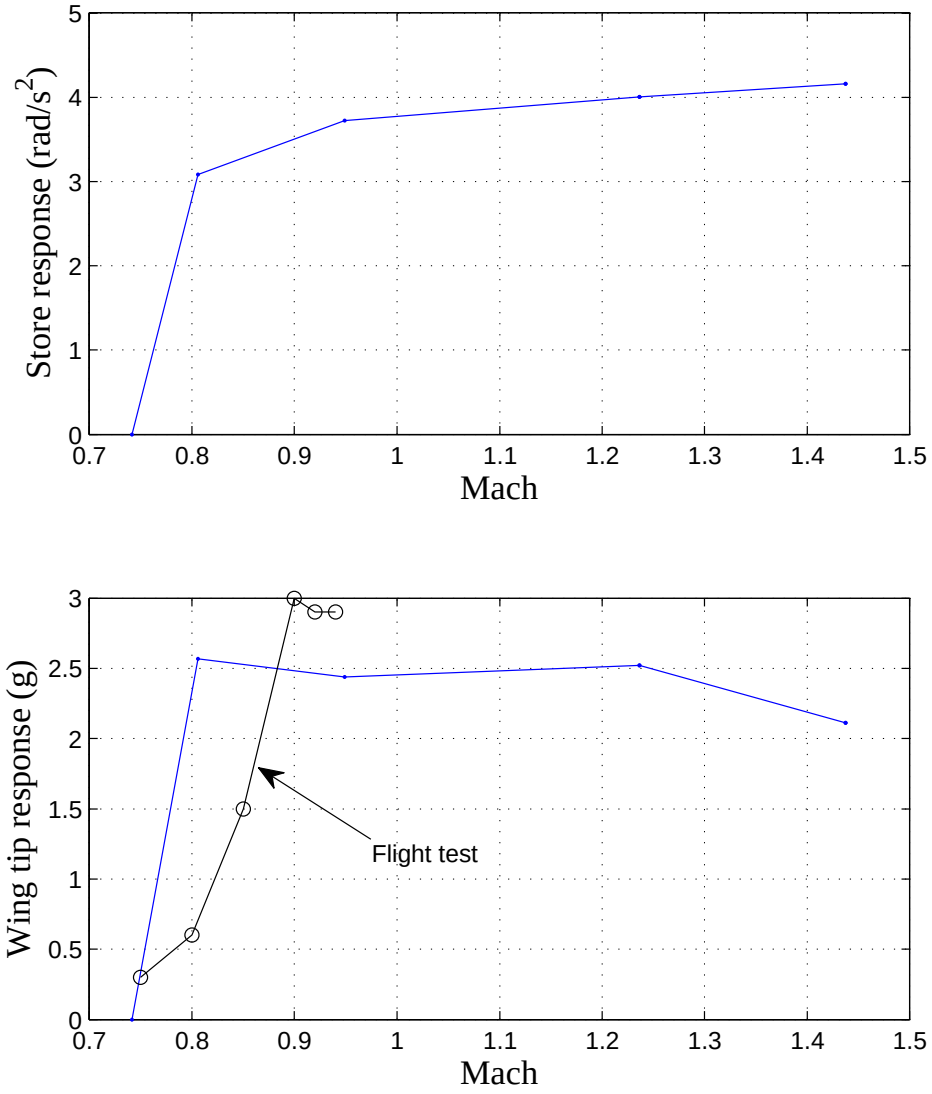

FIGURE 6.17: LCO responses for cubic softening stiffness in α_s, Stations 2/8

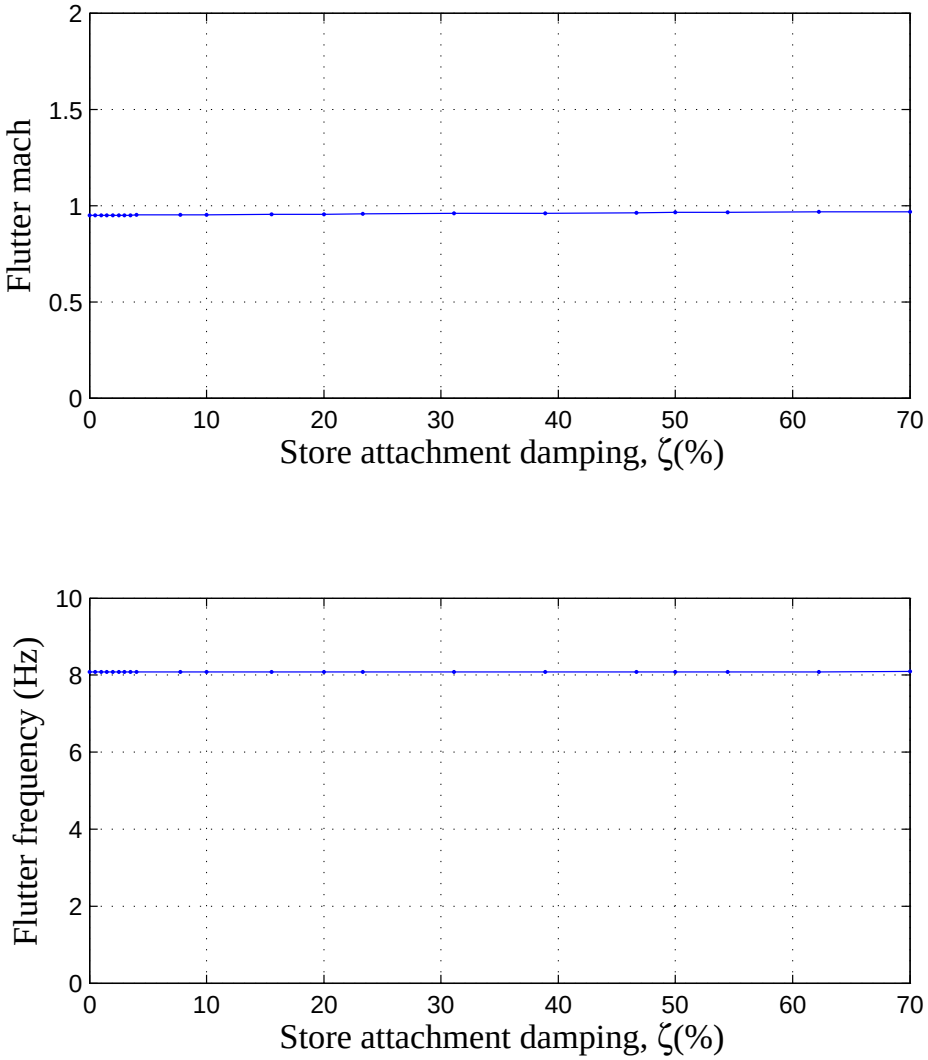

FIGURE 6.18: Flutter boundary vs ζ_{α_s}, Stations 2/8

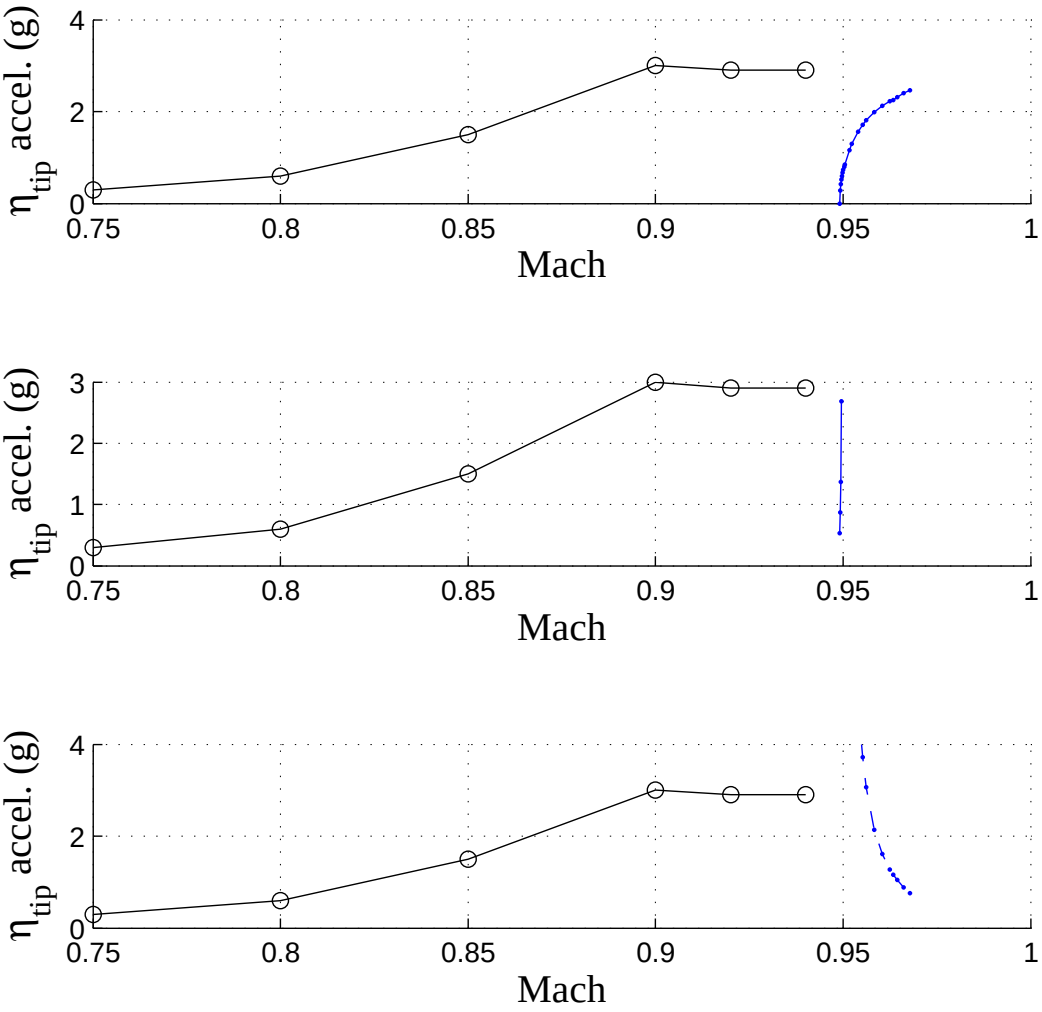

FIGURE 6.19: LCO responses for cubic damping (top), freeplay damping (middle) and friction damping (bottom)

The results discussed till now were all at 2000 ft altitude. Figure 6.21 shows flutter boundaries with respect to f_{α_s} at multiple altitudes. The low/medium f_{α_s} range was seen to have no flutter up to Mach 2.0, with the curves on either side tending to loop back. This was reasonable because decreasing f_{α_s} can be expected to (partially) decouple the wing from the store and bring it closer to being a 'clean wing' with very high flutter velocity outside the operational range of the aircraft. Also, the absence of the low f_{α_s} branch in the Stations 2/8 case was probably due to the wing-store decoupling effect being more pronounced at the wing outboard locations.

It is interesting to view the flutter boundaries for the F-16/NASA decoupler pylon [17, 38], generated using the Doublet Lattice Method. Those boundaries with respect to f_{α_s} at Stations 3/7 are reproduced in Figure 6.22. In plots i, ii the Stations 3/7 store inertia was comparable to that of the configuration in the present study, while in plots iii, iv the Stations 3/7 store was much lighter. Plots i-iii show antisymmetric flutter, with the flutter velocity increasing as f_{α_s} is reduced. This is consistent with the wing-store decoupling effect discussed above, and indeed it was the basis for the decoupler pylon concept. Plot iv shows symmetric flutter, where the flutter velocity dips and rises again as f_{α_s} is reduced.

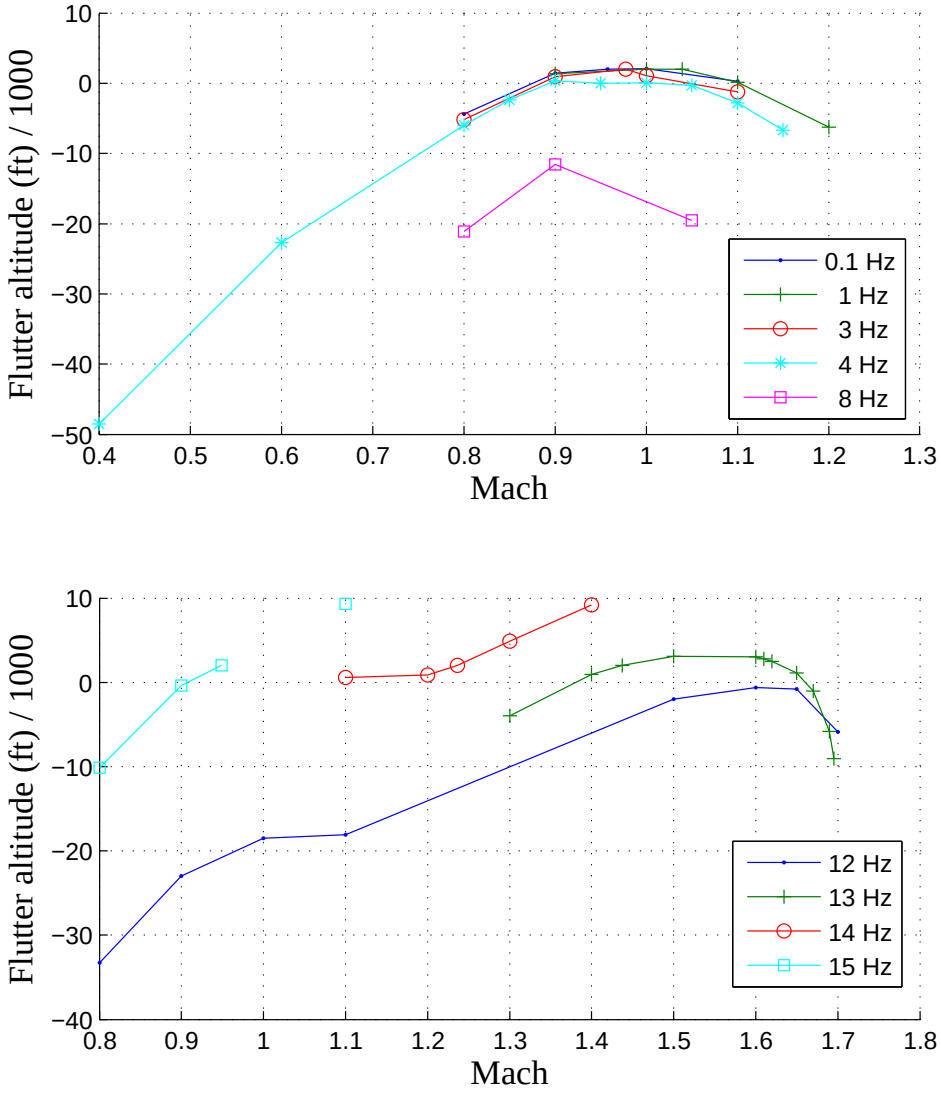

FIGURE 6.20: Approximate flutter Mach vs altitude for Stations 3/7 (top) and Stations 2/8 (bottom)

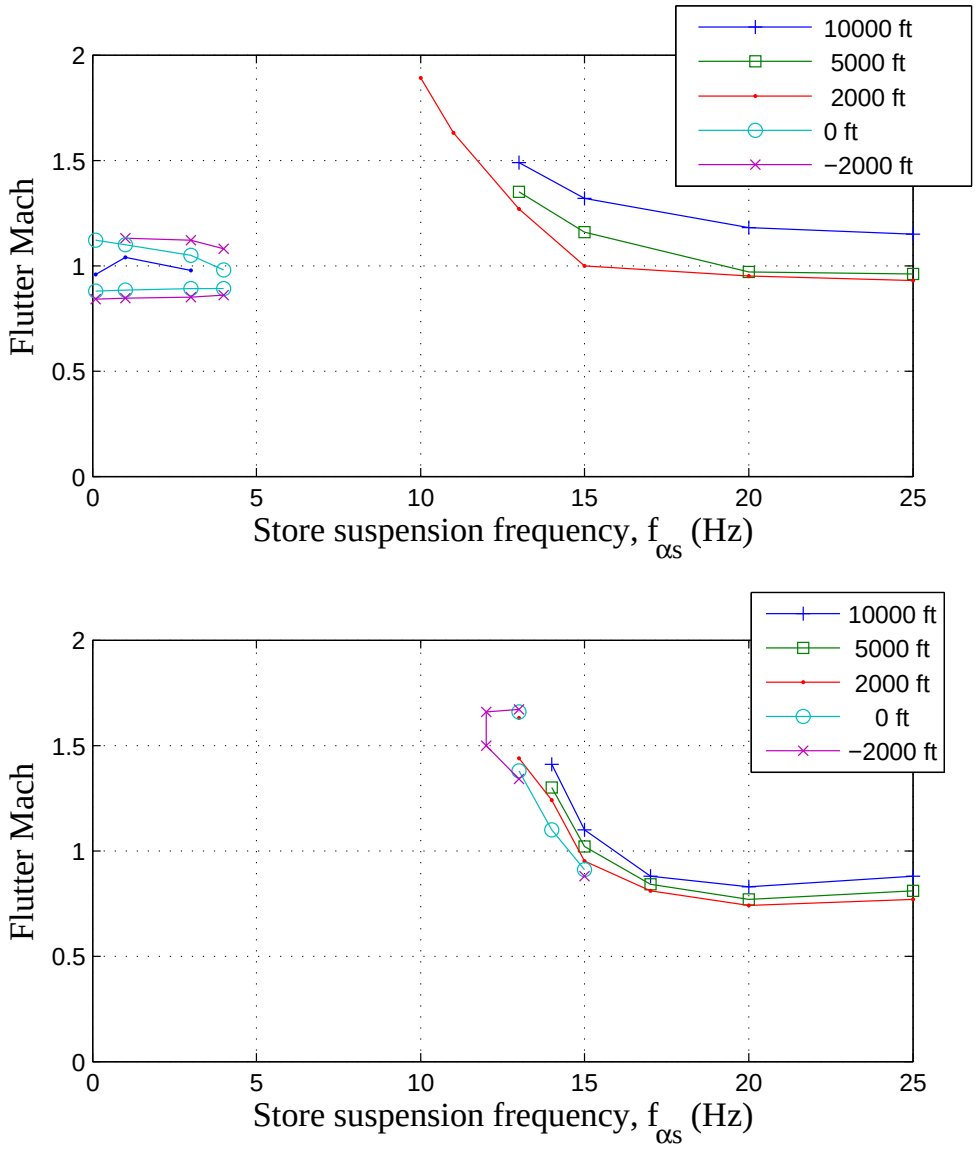

FIGURE 6.21: Effect of altitude on flutter boundary for Stations 3/7 (top) and Stations 2/8 (bottom)

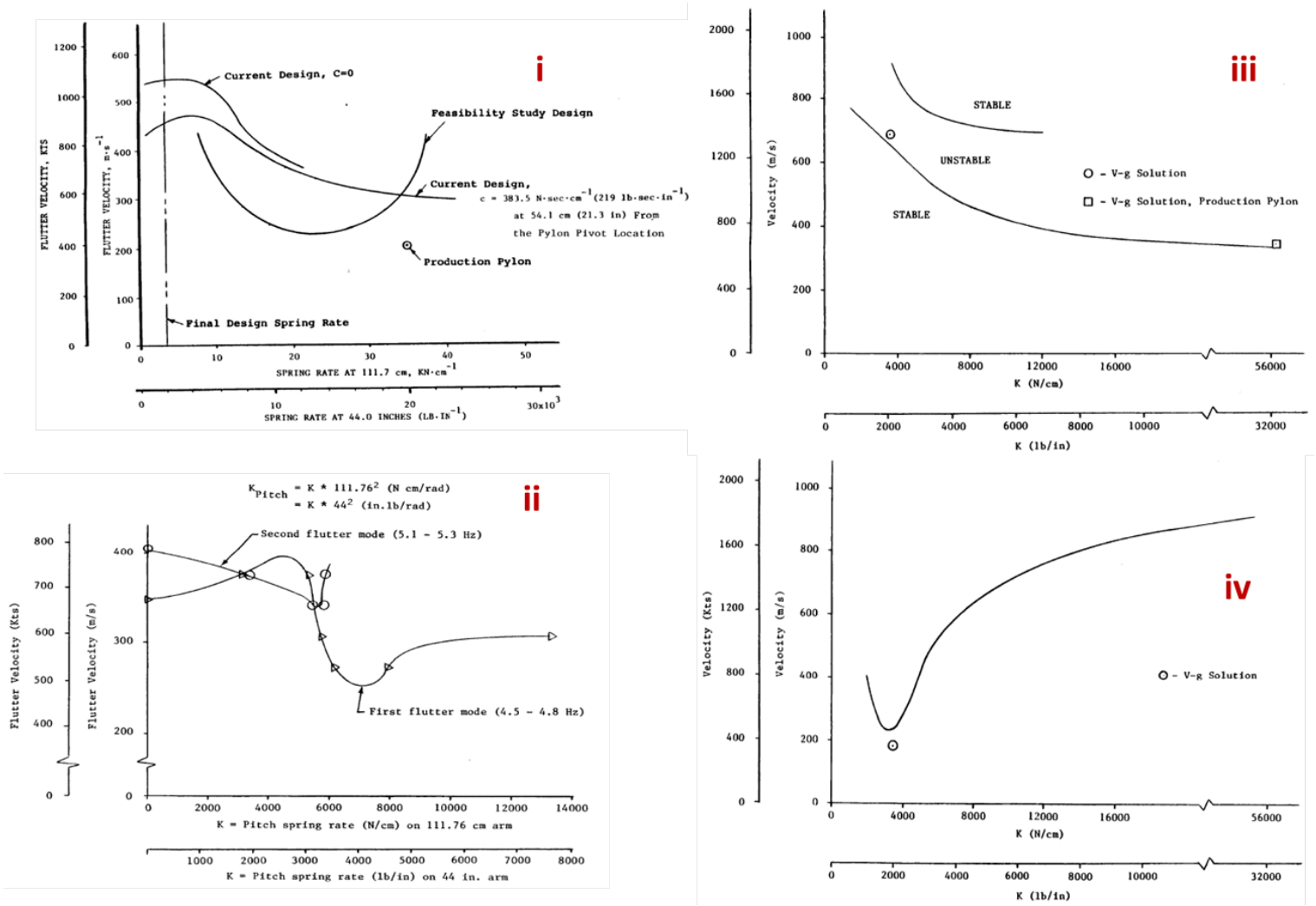

FIGURE 6.22: F-16 flutter boundaries vs decoupler pylon stiffness at Stations 3/7

6.7 Summary of LCO Response Trends

Transonic flutter boundaries were determined for the F-16 stores configuration described in [34], by varying the stiffness and damping levels in the wing-store attachments of wing span Stations 3/7 and Stations 2/8. These boundaries were used to construct LCO responses for a range for possible structural nonlinearities including cubic hardening/softening stiffness, freeplay stiffness, positive/negative cubic damping, freeplay damping and Coulomb friction.

Comparison of the computational results with flight test data indicates that the more probable nonlinear mechanisms producing/contributing to the F-16 LCO are cubic softening stiffness, positive cubic damping and freeplay damping. Stiffness can have a two-fold influence - on the nonlinear flutter/LCO onset velocity and on LCO magnitude. The former effect is seen in Table 6.1 which lists flutter/LCO onset Mach numbers for various linear stiffnesses of the wing-store attachment.

The experimental data of Northington and Pasiliao [14] shows no stiffness nonlinearity in the F-16 wing alone, and suggests other physical locations for structural nonlinearity such as the wing-store attachments. The present results also support the hypothesis of Chen, Sharma and Denegri [12, 39] that structural damping may be a cause of LCO.

Figure 6.23 (top line) shows LCO responses obtained for cubic damping in the different DOF and /or store stations, plotted after normalizing the Mach number axis by the flutter Mach number specific to each case. (The flight data was normalized by Mach 0.8, the best estimate of the flutter Mach number from flight test.) Also shown (in the bottom line) are the effective damping levels associated with each of the LCO responses. Among these, pitch damping at Stations 3/7 appears to be the more likely mechanism leading to LCO, since it provides the better match with flight data while accompanied by reasonable levels of effective (nonlinear) structural

damping.

Thus it appears that multiple sources of structural nonlinearity (in addition to aerodynamic nonlinearity) may be responsible for the wide range of LCO behavior exhibited by the F-16. Results from the present study that show the best match with flight test are collected in Fig. 6.24.

Table 6.1: Computed flutter/LCO onset Mach number vs store suspension frequency (*With best estimate of* $M_{flutter} = 0.8$ *from flight test*)

Stations 3/7:	Variation of f_{h_s},	with f_{α_s} fixed at 25 Hz
f_{h_s} (Hz)	Flutter Mach	Interacting modes
0.1	0.913	2,3
1	0.913	2,3
3	0.913	2,3
4	0.912	2,3
5	0.910	2,3
6.5	0.906	2,3
8	0.893	2,3
9	0.850	1,2,3,4
10	1.041	1,2
11	0.954	1,2
13	0.944	1,2
15	0.940	1,2
20	0.932	1,2
25	0.931	1,2
Stations 3/7:	Variation of f_{α_s},	with f_{h_s} fixed at 25 Hz
f_{α_s} (Hz)	Flutter Mach	Interacting modes
0.1	0.957	2,3
1	1.040	2,3
3	0.977	2,3
10	1.885	1,2
11	1.627	1,2
13	1.267	1,2
15	1.002	1,2
20	0.949	1,2
25	0.931	1,2
Stations 2/8:	Variation of f_{α_s},	with f_{h_s} fixed at 25 Hz
f_{α_s} (Hz)	Flutter Mach	Interacting modes
13	1.437	1,2
14	1.236	1,2
15	0.949	1,2
17	0.806	1,2
20	0.742	1,2
25	0.773	1,2

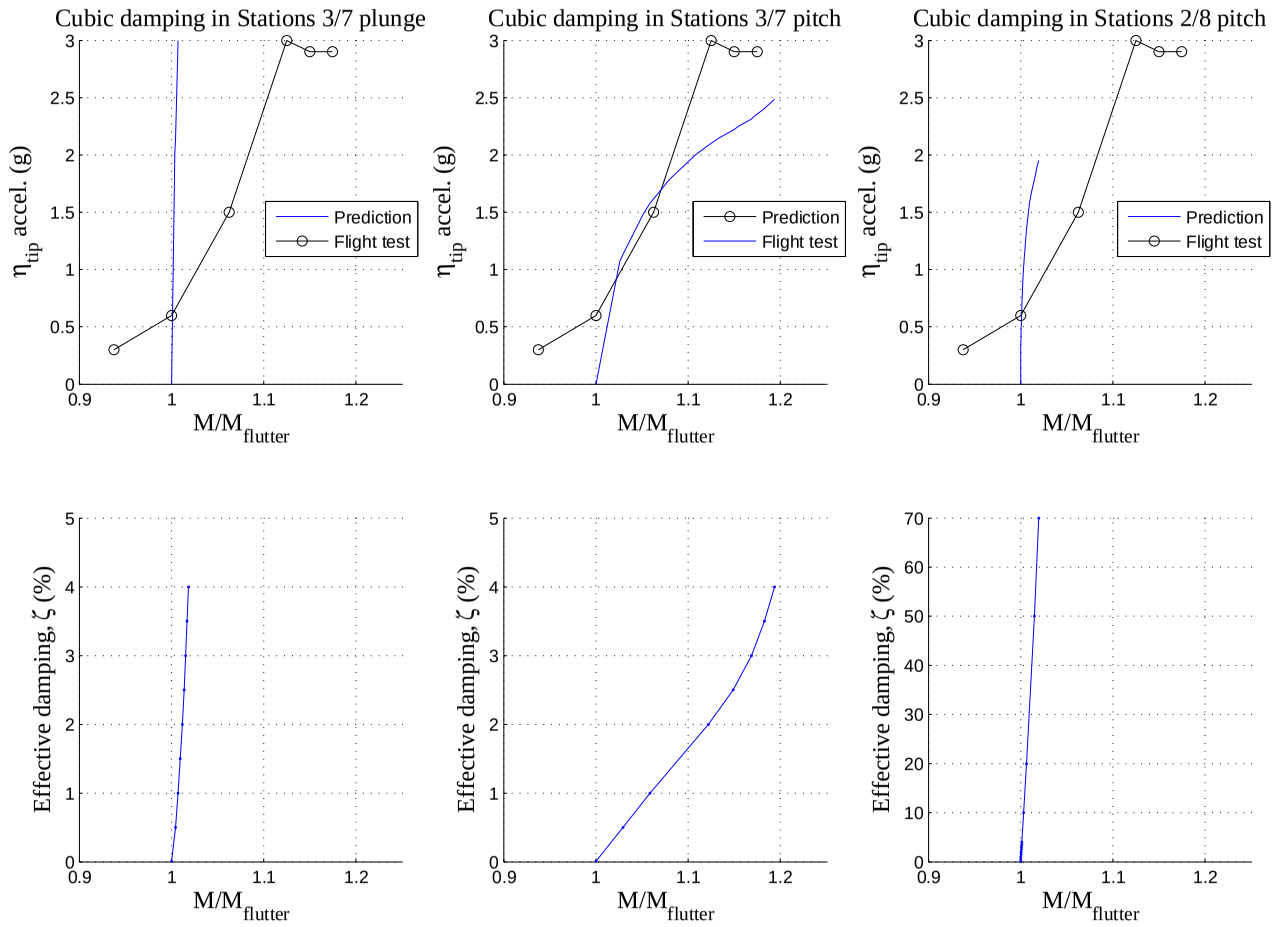

FIGURE 6.23: Wing tip LCO responses due to cubic hardening damping (top) and associated structural damping variation (bottom) (*Note that best estimate of* $M_{flutter}$ *from flight test was 0.8.*)

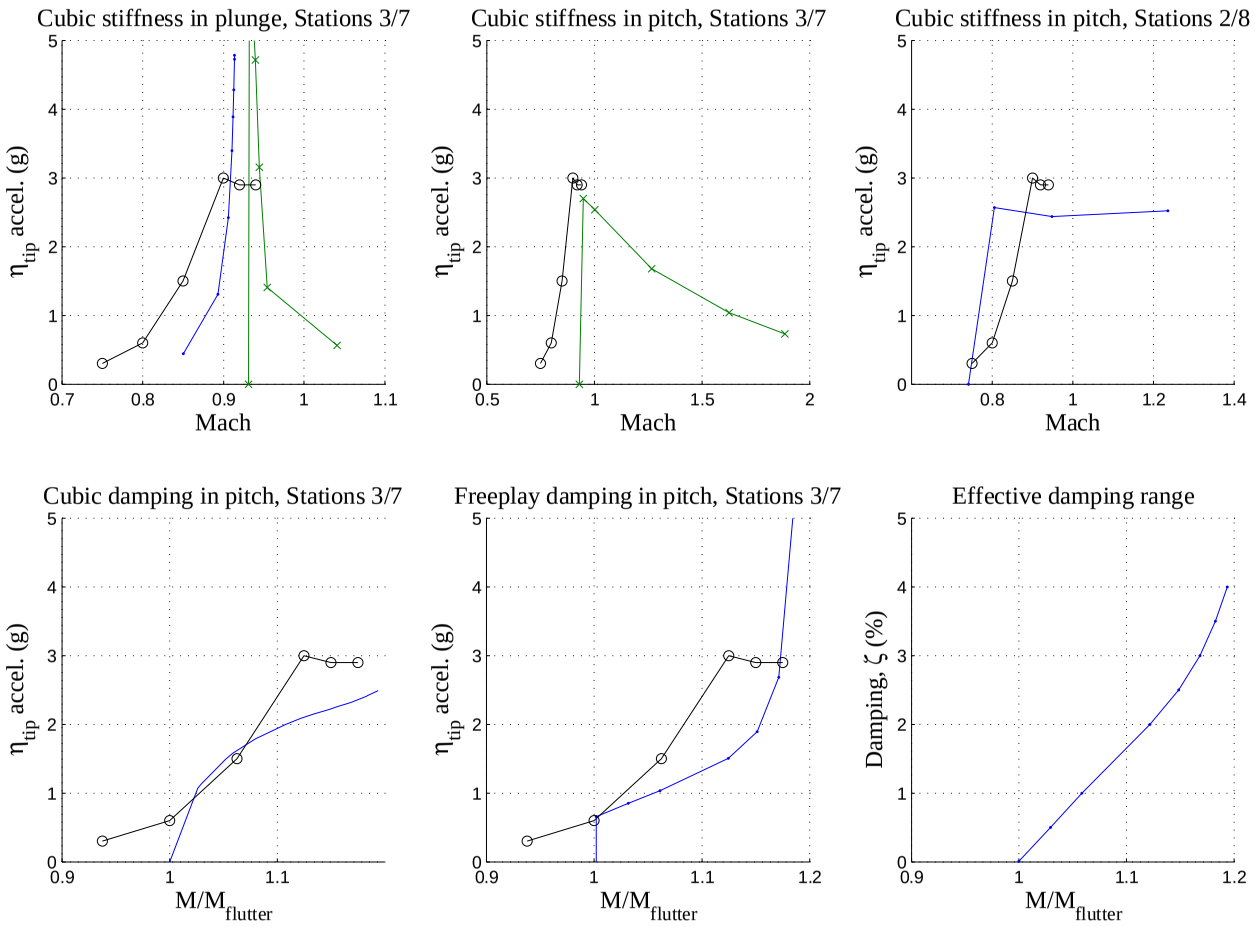

FIGURE 6.24: Most feasible LCO results due to nonlinear stiffness (top) and nonlinear damping (bottom) (*Note that bestestimateof $M_{flutter}$ from flight test was 0.8 for cubic damping and 1.2 for freeplay damping.*)

7

Conclusions

7.1 Work Accomplished

This work was undertaken to develop a better understanding of nonlinear aeroelastic phenomena, and their relation to classical flutter and divergence, with a particular focus on store-induced LCO in high performance fighter aircraft. The systems studied include (1) a 'simple' wing with a flexible and nonlinear root attachment, (2) a 'generic' wing with a flexible and nonlinear wing-store attachment and (3) the F-16 aircraft, again with a nonlinear wing-store attachment.

The consideration of structural nonlinearity here was complementary to several notable earlier studies that have focused on aerodynamic nonlinearity. LCO responses were calculated by applying Harmonic Balance in a common and consistent framework that was independent of the aerodynamic formulation, and also allowed the effects of various nonlinearities to be assessed over a wide range of parameters in a computationally efficient manner.

The simple wing and the generic wing were both modeled as linear beam-rods whose displacements were represented using the primitive modes method. They

were analyzed using linear potential flow aerodynamics. The nonlinear aeroelastic behaviors that were observed included (i) occurrence of unstable LCO and hysteresis due to positive cubic stiffness, depending on the ordering of the wing bending and torsion frequencies, (ii) delayed catastrophic flutter in the nonlinear system, due to LCO turning into flutter at a higher (but finite) flow velocity as compared to the linear system, (iii) linear flutter tendency without actual flutter (due to a hump in the flutter damping curve) manifesting as a minimum initial condition for entry into LCO, (iv) nonlinear static equilibrium/static LCO related to linear system static divergence, (v) atypical LCO, with the zero state being unstable over a finite flow velocity range and locally stable outside of it, and (vi) nontypical LCO due to cubic stiffness/damping existing over a finite flow velocity range. It was found possible to construct the bifurcation diagram of the nonlinear system by applying the HB method to the flutter and divergence boundaries of the model linearized about the origin. General relationships were established between the type of nonlinearity and the nature of the resulting response, and these were used to guide the F-16 study that followed.

For the F-16 aircraft, the starting point was a modal structural model that included the stores. Stiffness and damping of the wing-store attachments at Stations 3/7 and Stations 2/8 were modified using a dynamic decoupling/coupling technique. Since the LCO responses of the configuration under study occurred in the transonic range during the flight tests, the aeroelastic analyses were carried out with an RANS CFD Harmonic Balance solver, with dynamic linearization of the aerodynamics. The resulting flutter boundaries were used to calculate LCO responses due to structural nonlinearities including cubic and freeplay stiffness and cubic, freeplay & friction damping in the wing-store attachments.

Some of the above results were reported in [40, 41].

The F-16 computational results were compared to flight test data to assess the

likelihood of various nonlinear structural mechanisms causing the flight observed LCO. It appeared that cubic softening stiffness, positive cubic damping and freeplay damping could be significant factors that produce LCO. Stiffness could have a two-fold influence - on the nonlinear flutter/LCO onset velocity and on LCO magnitude. The experimental data of Northington and Pasiliao [14] showed no stiffness nonlinearity in the F-16 wing alone, thereby suggesting other physical locations for structural nonlinearity such as the wing-store attachments. The present results also supported the hypothesis of Chen, Sharma and Denegri [12, 39] that structural damping may be a cause of LCO.

Among the cubic damping results for various DOF and store stations, the nonlinear store pitch damping at Stations 3/7 appeared to be a likely mechanism leading to LCO, since it provided a better match with flight data than the others, while accompanied by reasonable levels of effective (nonlinear) structural damping. In general, multiple sources of structural nonlinearity (in addition to aerodynamic nonlinearity) may be responsible for the wide range of LCO behavior exhibited by the F-16.

7.2 Future Work

1. Analyzing an F-16 store configuration that exhibits LCO at subsonic (rather than transonic) velocities is perhaps the most promising direction in which to take this work forward. That would permit characterization of the contribution of wing-store attachment nonlinearities to LCO in isolation from the effects of nonlinear aerodynamics.

2. The contribution of nonlinear sideslip and yaw of the store may be studied, in the same manner that plunge and pitch of the store has been considered in this work. The F-16 structural modeshapes do show store lateral deflections.

3. Combining aerodynamic and structural nonlinearities in the analysis can be

useful to address any configuration in any flight regime. This requires running the HB aeroelastic solver at different levels of structural motion (as quantified by the first element of the aeroelastic eigenvector, ξ_1) for each modified structural model, and then finding the intersection point where the amplitude of the store motion that the aeroelastic solver yields matches the amplitude dictated by the structural nonlinearity. The procedural details are presented in Appendix D.

4. The HB based methodology can be used with an Euler or even DLM solver for quicker aerodynamic data generation.

5. It is highly desirable to acquire data from static and/or dynamic structural tests of the store assembly conducted on a hardback to determine directly the type and magnitude of the structural nonlinearity that may exist.

6. The effect of static preload on LCO response has been studied here for the case of cubic stiffness, and can be extended to other nonlinearities such as freeplay.

Appendix A

Torsion frequencies of a rod on a spring, in the limit $GJ \to 0$

Consider a uniform rod of length L with stiffness, GJ and moment of inertia, I_α, constrained by a stiffness, k_1 at the root. Let the twist be represented by two primitive modes, $\alpha(y,t) = \phi_1(y)q_1(t) + \phi_2(y)q_2(t)$, with $\phi_1 = 1$ (the rigid body mode) and $\phi_2 = cos(\pi y/L)$ (the first free-free torsion mode). Then the kinetic and elastic potential energies are

$$T = \frac{1}{2}\int_0^L I_\alpha \dot{\alpha}(y,t)^2 dy = \frac{I_\alpha}{2}\int_0^L (\phi_1\dot{q}_1 + \phi_2\dot{q}_2)^2 dy = \frac{I_\alpha}{2}(\dot{q}_1^2 L + \dot{q}_2^2 L/2) \tag{A.1}$$

$$\begin{aligned} U &= \frac{1}{2}\int_0^L GJ\alpha'(y,t)^2 dy + \frac{1}{2}k_1\alpha(0,t)^2 \\ &= \frac{GJ}{2}\int_0^L (\phi_1' q_1 + \phi_2' q_2)^2 dy + \frac{1}{2}k_1(q_1+q_2)^2 = \frac{GJ}{2}(q_2^2\frac{\pi^2}{L^2}L/2) + \frac{1}{2}k_1(q_1+q_2)^2 \end{aligned} \tag{A.2}$$

where $(\dot{}) \equiv d/dt$ and $(') \equiv d/dy$

Applying Lagrange's equations yields

$$\begin{bmatrix} I_\alpha L & 0 \\ 0 & I_\alpha L/2 \end{bmatrix} \begin{Bmatrix} \ddot{q}_1 \\ \ddot{q}_2 \end{Bmatrix} + \begin{bmatrix} k_s & k_s \\ k_s & k_s + GJ\pi^2/2L \end{bmatrix} \begin{Bmatrix} q_1 \\ q_2 \end{Bmatrix} = 0 \tag{A.3}$$

When GJ is made zero, the stiffness matrix is singular and one of the system natural frequencies is zero. The other frequency turns out to be $\sqrt{3k_s/I_\alpha L}$, i.e. $\sqrt{3}$ times the frequency that would exist if the rod were rigid.

Appendix B

Nonlinear static aeroelastic equilibrium and stability of the B1T2 simple wing model

Based on Eqn. 2.3, the B1T2 model with a torsion spring at the root is represented by

$$M \begin{Bmatrix} \ddot{q}^h \\ \ddot{q}_1^\alpha \\ \ddot{q}_2^\alpha \end{Bmatrix} + C \begin{Bmatrix} \dot{q}^h \\ \dot{q}_1^\alpha \\ \dot{q}_2^\alpha \end{Bmatrix} + K \begin{Bmatrix} q^h \\ q_1^\alpha \\ q_2^\alpha \end{Bmatrix} + k_3 \left(\phi_1^\alpha(0) q_1^\alpha + \phi_2^\alpha(0) q_2^\alpha\right)^3 \begin{Bmatrix} 0 \\ \phi_1^\alpha(0) \\ \phi_2^\alpha(0) \end{Bmatrix} = 0 \quad \text{(B.1)}$$

where the linear spring term, k_1 and the (quasisteady) aerodynamic forcing terms have been combined with the wing stiffness and damping.[1]

To solve for the static equilibrium, the time dependent terms are set to zero. Since $\phi_1^\alpha = 1$ and $\phi_2^\alpha = cos(\pi y/L)$, we obtain

$$K_{11} q^h + K_{12} q_1^\alpha + K_{13} q_2^\alpha = 0 \quad \text{(B.2)}$$

$$\begin{aligned} K_{22} q_1^\alpha + K_{23} q_2^\alpha + k_3 (q_1^\alpha + q_2^\alpha)^3 = 0 \\ K_{32} q_1^\alpha + K_{33} q_2^\alpha + k_3 (q_1^\alpha + q_2^\alpha)^3 = 0 \end{aligned} \quad \text{(B.3)}$$

[1] The combined C and K are unsymmetric because of the aerodynamic terms.

Equation B.3 is solved for the q^α, and then Eqn. B.2 for q^h. In addition to the zero solution, there are two symmetric nonzero solutions given by

$$\alpha_{static} = q_1^\alpha + q_2^\alpha = \pm\sqrt{\frac{K_{33}(K_{22} - K_{23}) - K_{23}(K_{32} - K_{33})}{(K_{32} - K_{33} - K_{22} + K_{23})k_3}} \tag{B.4}$$

The solution's stability is assessed by considering a small perturbation, $\hat{q}(t) = \begin{bmatrix}\hat{q}^h & \hat{q}_1^\alpha & \hat{q}_2^\alpha\end{bmatrix}^T$ from the equilibrium position, $q = \begin{bmatrix}q^h & q_1^\alpha & q_2^\alpha\end{bmatrix}^T$. Inserting this into Eqn. B.1 leads to

$$M\ddot{\hat{q}} + C\dot{\hat{q}} + K\hat{q} + k_3(3\alpha_{static}^2\hat{\alpha} + 3\alpha_{static}\hat{\alpha}^2 + \hat{\alpha}^3)\begin{Bmatrix}0\\1\\1\end{Bmatrix} = 0 \tag{B.5}$$

where $\hat{\alpha} = \hat{q}_1^\alpha + \hat{q}_2^\alpha$. Retaining terms that are linear in the $\hat{q}^\alpha$ leads to

$$M\ddot{\hat{q}} + C\dot{\hat{q}} + \left(K + 3k_3\alpha_{static}^2\begin{bmatrix}0 & 0 & 0\\0 & 1 & 1\\0 & 1 & 1\end{bmatrix}\right)\hat{q} = 0 \tag{B.6}$$

Stability of the static equlibrium is assessed from the eigenvalues of the above system.

Appendix C

Component mode synthesis of wing and store connected by a flexible and damped attachment

For the modal synthesis of a damped system, two examples are given in [23]. One deals with a damped beam contrained at a single point. The other deals with the attachment of a grounded spring-damper to a beam. Equations are derived here along the same lines for a different case, namely the addition of an ungrounded mass-spring-damper to an MDOF system. This case is relevant when a store is connected to a wing through a damped, flexible attachment.

The kinetic energy is

$$T = T_{wing} + T_{store} = \frac{1}{2}\sum_{1}^{N} M_n \dot{q_n}^2 + \frac{1}{2}M(\dot{\eta} + \dot{z})^2 \tag{C.1}$$

and the elastic potential energy is

$$V = V_{wing} + V_{store} = \frac{1}{2}\sum_{1}^{N} M_n {\omega_n}^2 q_n^2 + \frac{1}{2}M\omega_z^2 z^2 \tag{C.2}$$

where ψ_n are wing-without-store modeshapes at the store location, q_n are the associated generalized coordinates and $\eta = \sum \psi_n q_n(t)$ is the wing displacement at the store location; z is the store displacement relative to wing, M is the store mass, and Mw_z^2 is the attachment stiffness.

The augmented Lagrangian is

$$L = T - V + \lambda(\eta - \sum \psi_n q_n) \tag{C.3}$$

Applying Lagrange's equations with respect to q_n, z and η leads to

$$M_n(\ddot{q}_n + 2\zeta_n\omega_n\dot{q}_n + \omega_n^2 q_n) + \lambda\psi_n = 0 \tag{C.4a}$$

$$M(\ddot{\eta} + \ddot{z} + 2\zeta_z\omega_z\dot{z} + \omega_z^2 z) = 0 \tag{C.4b}$$

$$M(\ddot{\eta} + \ddot{z}) - \lambda = 0 \tag{C.4c}$$

Damped harmonic motion is assumed and the following are inserted into the above equations.

$$q_n = \bar{q}_n e^{\alpha t} \quad ; \quad z = \bar{z}e^{\alpha t} \quad ; \quad \eta = \bar{\eta}e^{\alpha t} \quad ; \quad \lambda = \bar{\lambda}e^{\alpha t} \tag{C.5}$$

Thus

$$\bar{q}_n = -\bar{\lambda}\psi_n/[M_n(\alpha^2 + 2\zeta_n\omega_n\alpha + \omega_n^2)] \tag{C.6a}$$

$$\alpha^2\bar{\eta} + (\alpha^2 + 2\zeta_z\omega_z\alpha + \omega_z^2)\bar{z} = 0 \tag{C.6b}$$

$$M\alpha^2(\bar{\eta} + \bar{z}) = \bar{\lambda} \tag{C.6c}$$

From the latter two eqns,

$$\bar{\eta} + \bar{z} = \bar{\eta} - \alpha^2\bar{\eta}/(\alpha^2 + 2\zeta_z\omega_z\alpha + \omega_z^2) = \bar{\lambda}/(M\alpha^2) \tag{C.7a}$$

$$\implies \bar{\eta} = \frac{\bar{\lambda}}{M\alpha^2}\frac{\alpha^2 + 2\zeta_z\omega_z\alpha + \omega_z^2}{2\zeta_z\omega_z\alpha + \omega_z^2} \tag{C.7b}$$

Substitute this into the constraint equation to get

$$\bar{\lambda}\left[\sum \frac{\psi_n^2}{M_n(\alpha^2+2\zeta_n\omega_n\alpha+\omega_n^2)}+\frac{\alpha^2+2\zeta_z\omega_z\alpha+\omega_z^2}{M\alpha^2(2\zeta_z\omega_z\alpha+\omega_z^2)}\right]=\lambda D=0 \tag{C.8}$$

If the damping is made zero, this simplifies to

$$\bar{\lambda}\left[\sum \frac{\psi_n^2}{M_n(-\omega^2+\omega_n^2)}-\frac{-\omega^2+\omega_z^2}{M\omega^2\omega_z^2}\right]=0 \tag{C.9}$$

which agrees with Eqn. 7a of [37]. Solving this determinant will yield the undamped natural frequencies of the wing-with-store.

Now the small damping approximation taken from Eqn 10.30 of [23], $\alpha=-\zeta\omega\pm i\omega\sqrt{1-\zeta^2}\approx-\zeta\omega\pm i\omega$ is used in Eqn. C.8, and only the first power of ζ is retained in all the resulting expressions. Then the determinant becomes

$$\begin{aligned} D=&\sum \frac{\psi_n^2[-\omega^2+\omega_n^2-2i\omega(-\zeta\omega+\zeta_n\omega_n)]}{M_n(-\omega^2+\omega_n^2)^2} \\ -&\frac{1}{M\omega^2\omega_z^3}[\omega_z(-\omega^2+\omega_z^2)+2i\omega\omega_z(-\zeta\omega+\zeta_z\omega_z)-2i(\zeta_z\omega+\zeta\omega_z)(-\omega^2+\omega_z^2)] \end{aligned} \tag{C.10}$$

The real part of D is the same as the D for the undamped case, i.e., Eqn. C.9. The imaginary part is

$$D_I=\sum \frac{\psi_n^2\omega(-\zeta\omega+\zeta_n\omega_n)}{M_n(-\omega^2+\omega_n^2)^2}+\frac{(-\zeta\omega+\zeta_z\omega_z)}{M\omega\omega_z^2}-\frac{(-\omega^2+\omega_z^2)(\zeta_z\omega+\zeta\omega_z)}{M\omega^2\omega_z^3} \tag{C.11}$$

Setting $D_I=0$ leads to

$$\zeta\omega = \frac{\sum \frac{\psi_n^2 \omega \zeta_n \omega_n}{M_n(-\omega^2+\omega_n^2)^2} + \frac{\zeta_z \omega_z}{M\omega\omega_z^2} - \frac{\zeta_z \omega(-\omega^2+\omega_z^2)}{M\omega^2\omega_z^3}}{\sum \frac{\psi_n^2 \omega}{M_n(-\omega^2+\omega_n^2)^2} + \frac{1}{M\omega\omega_z^2} + \frac{(\omega_z/\omega)(-\omega^2+\omega_z^2)}{M\omega^2\omega_z^3}} \tag{C.12}$$

An interesting aspect of the examples in [23] is the simplification obtained when the wing and store damping decay rates are all equal, i.e., $\zeta_n\omega_n = \zeta_z\omega_z$: the resulting wing-with-store modes also have the same decay rate. This simplification did not occur in the present model. Next, the model was modified by grounding the store with an additional spring-damper and the following equation was obtained.

$$\begin{aligned}\zeta\omega = [\sum \frac{\psi_n^2 \zeta_n \omega_n}{M_n(-\omega^2+\omega_n^2)^2} - \frac{1}{M\omega_z^2(-\omega^2+\omega_{z2}^2)} \\ \left\{\zeta_z\omega_z + \zeta_{z2}\omega_{z2} - (-\omega^2+\omega_z^2+\omega_{z2}^2)(\frac{\zeta_{z2}\omega_{z2}}{-\omega^2+\omega_{z2}^2} + \frac{\zeta_z}{\omega_z})\right\}] \\ \div [\sum \frac{\psi_n^2}{M_n(-\omega^2+\omega_n^2)^2} - \frac{1}{M\omega_z^2(-\omega^2+\omega_{z2}^2)} \left\{1 - (-\omega^2+\omega_z^2+\omega_{z2}^2)(\frac{1}{-\omega^2+\omega_{z2}^2})\right\}]\end{aligned} \tag{C.13}$$

Here too, the simplification was absent. This may be due to the fact that both of these models acquired an additional DOF when the store was added, in contrast to [23] where the number of DOF either decreased or remained the same after the modal synthesis.

Appendix D

LCO Response Calculation with Combined Structural and Aerodynamic Nonlinearities

The calculation procedure for LCO response due to structural nonlinearity (but also accounting for *steady flow* aerodynamic nonlinearities), was outlined in Section 5.4. In that case, the unsteady aerodynamic forces were linearized by assuming a small value for the first element of the flutter eigenvector, ξ_1. The HB aeroelastic solver yielded the flutter Mach number, frequency and the full eigenvector, ξ for each modified value of the store suspension frequency, f_{h_s}. On the basis of Eqn. 5.3, the $\{\xi\}$ was scaled to be consistent with the h_s magnitude dictated by the structural nonlinearity under consideration (e.g., cubic restoring force), and then used to derive the displacements and accelerations at the wing tip. Equation 5.3 is reproduced below.

$$\begin{Bmatrix} \{q\} \\ h_s \\ \alpha_s \end{Bmatrix} = [E]\{\xi\} \quad ; \quad \eta_{tip} = \sum_{1}^{N} \psi_n q_n = [\Psi_{wos}]\{q\} = [\Psi_{ws}]\{\xi\} \tag{D.1}$$

To include the aerodynamic nonlinearity, the HB solver needs to be run for differ-

ent levels of structural motion for each modified aircraft model. Say these levels are quantified by $\xi_1 = \xi_{1a}$, ξ_{1b}, ξ_{1c}, etc. The runs will yield a series of flutter boundaries and corresponding eigenvectors, $\xi = \xi_a$, ξ_b, ξ_c, etc.

Next, consistency must be achieved between the structural and aerodynamic nonlinearities at a given f_{h_s}, as follows. Using Eqn. D.1, a series of $h_s = h_{sa}$, h_{sb}, h_{sc}, etc are calculated *but without scaling the* ξ. The h_s that is closest to the value dictated by the structural nonlinearity (say h_{sb}) is chosen, and ξ_b is used to calculate the wing tip response, η_{tip}. Plotting η_{tip} against the Mach number yields one point in the LCO response curve, and the procedure needs to be repeated for different f_{h_s} to obtain the entire curve.

Bibliography

[1] W. J. Norton. Limit Cycle Oscillation and Flight Flutter Testing. In *Society of Flight Test Engineers, 21st Annual Symposium, Garden Grove, CA*, page 3, 1990.

[2] C. M. Denegri. Limit Cycle Oscillation Flight Test Results of a Fighter with External Stores. *Journal of Aircraft*, 37(5):761–769, 2000.

[3] R. W. Bunton and C. M. Denegri. Limit Cycle Oscillation Characteristics of Fighter Aircraft. *Journal of Aircraft*, 37(5):916–918, 2000.

[4] W. A. Silva and S. Dunn. Higher-Order Spectral Analysis of F-18 Flight Flutter Data. In *46th AIAA/ASME/ASCE/AHS/ASC Structures, Structural Dynamics & Materials Conference, Austin, Texas*, 2005.

[5] C. C. Chabalko. *Identification of Transient Nonlinear Aeroelastic Phenomena, Chapter 2*. PhD thesis, University of Virginia.

[6] E. H. Dowell and D. Tang. Nonlinear Aeroelasticity and Unsteady Aerodynamics. *AIAA Journal*, 40(9):1697–1707, 2002.

[7] E. H. Dowell, J. Edwards, and T. Strganac. Nonlinear Aeroelasticity. *Journal of Aircraft*, 40(5):857–874, 2003.

[8] D. E. Thompson Jr and T. W. Strganac. Nonlinear Analysis of Store-Induced Limit Cycle Oscillations. *Nonlinear Dynamics*, 39(1-2):159–178, 2005.

[9] R. L. Bisplinghoff, H. Ashley, and R. L. Halfman. *Aeroelasticity*. Courier Corporation, 1996.

[10] D. Tang and E. H. Dowell. Flutter and Limit-Cycle Oscillations for a Wing-Store Model with Freeplay. *Journal of Aircraft*, 43(2):487–503, 2006.

[11] E. H. Dowell, J. P. Thomas, C. H. Hall, and Jr. Denegri, C. M. Theoretical Predictions of F-16 Fighter Limit Cycle Oscillations for Flight Flutter Testing. *Journal of Aircraft*, 46(5):1667–1672, 2009.

[12] V. K. Sharma and C. M. Denegri Jr. Time Domain Aeroelastic Solution using Exact Aerodynamic Influence Coefficients and Nonlinear Damping. *International Forum on Aeroelasticity and Structural Dynamics*, IFASD-2013-29D.

[13] C. L. Pasiliao. *Temporal Analysis of Transonic Flow Field Characteristics associated with Limit Cycle Oscillations, Chapter 2*. PhD thesis, University of Florida 2009.

[14] J. S. Northington and C. L. Pasiliao. F-16 Wing Structural Deflection Testing–Phase I. *AIAA Paper*, 1674, 2007.

[15] Federation of American Scientists. MAU-12 Ejector Rack, 1999. URL: `http://www.fas.org/man/dod-101/sys/ac/equip/mau-12.htm`.

[16] J-P. Noël, L. Renson, G. Kerschen, B. Peeters, S. Manzato, and J. Debille. Nonlinear Dynamic Analysis of an F-16 Aircraft using GVT Data. In *International Forum on Aeroelasticity and Structural Dynamics*, 2013.

[17] J. D. Clayton, R. L. Haller, and J.M. Hassler Jr. Design and Fabrication of the NASA Decoupler Pylon for the F-16 Aircraft. January 1985.

[18] M. D. Conner, D. M. Tang, E. H. Dowell, and L. N. Virgin. Nonlinear Behavior of a Typical Airfoil Section with Control Surface Freeplay: a Numerical and Experimental Study. *Journal of Fluids and Structures*, 11(1):89–109, 1997.

[19] D. Tang, E. H. Dowell, and L. N. Virgin. Limit Cycle Behavior of an Airfoil with a Control Surface. *Journal of Fluids and Structures*, 12(7):839–858, 1998.

[20] W. Anderson and S. Mortara. Maximum Control Surface Freeplay, Design and Flight Testing Approach on the F-22. In *48th AIAA Structures, Structural Dynamics and Materials Conference*, pages 2007–1767, 2007.

[21] C. Goodman, M. Hood, E. Reichenbach, and R. Yurkovich. An Analysis of the F/A-18C/D Limit Cycle Oscillation Solution. *AIAA Paper*, 1424, 2003.

[22] Dowell E. H., et al. *A Modern Course in Aeroelasticity*. Kluwer Academic, 2004.

[23] E. H. Dowell and D. Tang. *Dynamics of Very High Dimensional Systems*. World Scientific, 2003.

[24] Eusebius Doedel, Concordia University. AUTO - Software for Continuation and Bifurcation Problems in Ordinary Differential Equations, 2010. URL: `http://indy.cs.concordia.ca/auto/`.

[25] J. P. Den Hartog. *Mechanical Vibrations, 1956*, volume 2.

[26] K. C. Hall. Eigenanalysis of Unsteady Flows about Airfoils, Cascades, and Wings. *AIAA Journal*, 32(12):2426–2432, 1994.

[27] N. R. Hoffman and I. N. Spielberg. Subsonic Flutter Tests of an Unswept All-Movable Horizontal Tail. Technical report, WADC-TR-54-53, 1954.

[28] J. R. Wright and J. E. Cooper. *Introduction to Aircraft Aeroelasticity and Loads*.

[29] S. H. Strogatz. *Nonlinear Dynamics and Chaos: with Applications to Physics, Biology, Chemistry, and Engineering, Cambridge, MA*. Westview Press, 1994.

[30] A. A. Ferri and E. H. Dowell. Frequency Domain Solutions to Multi-Degree-of-Freedom, Dry Friction Damped Systems. *Journal of Sound and Vibration*, 124(2):207–224, 1988.

[31] A. M. Cunningham and R. J. Holman. Time Domain Aeroelastic Solutions - A Critical Need for Future Analytical Methods Developments. In *NATO Rept. RTA-MP-AVT-154, Paper 12, Fig. 26*, 2008.

[32] J. T. Gordon. Perturbation Analysis of Nonlinear Wheel Shimmy. *Journal of Aircraft*, 39(2):305–317, 2002.

[33] Lockheed Martin. F-16 Specifications, 2015. URL: `http://http://www.lockheedmartin.com/us/products/f16/F-16Specifications.html`.

[34] C. M. Denegri, J. A. Dubben, and D. L. Maxwell. In-Flight Wing Deformation Characteristics during Limit Cycle Oscillations. *Journal of Aircraft*, 42(2):500–508, 2005.

[35] C. M. Denegri Jr and J. A. Dubben. F-16 Limit Cycle Oscillation Analysis using Transonic Small-Disturbance Theory. *AIAA paper*, 2296:2005, 2005.

[36] E. H. Dowell. Theory and Application of Dynamic Decoupling in Structural Analysis: Another View. *Finite Elements in Analysis and Design*, 3(2):119–125, 1987.

[37] E. H. Dowell. On Some General Properties of Combined Dynamical Systems. *Journal of Applied Mechanics*, 46(1):206–209, 1979.

[38] J. D. Clayton and R. L. Haller. Design and Fabrication of the NASA Decoupler Pylon for the F-16 Aircraft, Addendum 1. January 1985.

[39] P. C. Chen, D. Sarhaddi, and D. D. Liu. Limit Cycle Oscillation Studies of a Fighter with External Stores. *AIAA paper*, AIAA-98-1727, 1998.

[40] M. A. Padmanabhan, C. L. Pasiliao, and E. H. Dowell. Simulation of Aeroelastic Limit-Cycle Oscillations of Aircraft Wings with Stores. *AIAA Journal*, 52(10):2291–2299, 2014.

[41] M. A. Padmanabhan, C. L. Pasiliao, and E. H. Dowell. Store-Induced Limit Cycle Oscillations due to Nonlinear Wing-Store Attachment.

Biography

Madhusudan A. Padmanabhan was born on August 6, 1971 at Udyogamandal, Kerala, India. He was brought up in Chennai (earlier Madras) and obtained the B.Tech degree in Mechanical Engineering from the Indian Institute of Technology, Madras in 1993. This was followed by an MS degree from the University of Maryland, College Park in 1995. He then obtained employment at the Aeronautical Development Agency (ADA), Bangalore and returned to India. After working for 15 years on aeroservoelastic analysis and testing of fighter aircraft, he decided to upgrade his academic knowledge and research skills with a PhD degree from Duke University, which he obtained in 2015. He will be returning to ADA subsequently.